

Accelerated Sepsis Diagnosis by Seamless Integration of
Nucleic Acid Purification and Detection

by

Bang-Ning Hsu

Department of Electrical and Computer Engineering
Duke University

Date: _____

Approved:

Richard B. Fair, Supervisor

Krishnendu Chakrabarty

Chuan-Hua Chen

Chris L. Dwyer

Nan M. Jokerst

Dissertation submitted in partial fulfillment of the requirements for the degree of
Doctor of Philosophy in the Department of Electrical and Computer Engineering
in the Graduate School of Duke University

2014

ABSTRACT

Accelerated Sepsis Diagnosis by Seamless Integration of
Nucleic Acid Purification and Detection

by

Bang-Ning Hsu

Department of Electrical and Computer Engineering
Duke University

Date: _____

Approved:

Richard B. Fair, Supervisor

Krishnendu Chakrabarty

Chuan-Hua Chen

Chris L. Dwyer

Nan M. Jokerst

An abstract of a dissertation submitted in partial fulfillment of the requirements for
the degree of Doctor of Philosophy in the Department of Electrical and Computer
Engineering
in the Graduate School of Duke University
2014

Copyright © 2014 by Bang-Ning Hsu
All rights reserved.

Abstract

Background The diagnosis of sepsis is challenging because the infection can be caused by more than 50 species of pathogens that might exist in the bloodstream in very low concentrations, e.g., less than 1 colony-forming unit/ml. As a result, among the current sepsis diagnostic methods there is an unsatisfactory trade-off between the assay time and the specificity of the derived diagnostic information. Although the present qPCR-based test is more specific than biomarker detection and faster than culturing, its 6 ~ 10 hr turnaround remains suboptimal relative to the 7.6%/hr rapid deterioration of the survival rate, and the 3 hr hands-on time is labor-intensive. To address these issues, this work aims to utilize the advances in microfluidic technologies to expedite and automate the “nucleic acid purification - qPCR sequence detection” workflow.

Methods and Results This task is evaluated to be best approached by combining immiscible phase filtration (IPF) and digital microfluidic droplet actuation (DM) on a fluidic device. In IPF, as nucleic acid-bound magnetic beads are transported from an aqueous phase to an immiscible phase, the carryover of aqueous contaminants is minimized by the high interfacial tension. Thus, unlike a conventional bead-based assay, the necessary degree of purification can be attained in a few wash steps. After IPF reduces the sample volume from a milliliter-sized lysate to a microliter-sized eluent, DM can be used to automatically prepare the PCR mixture. This begins with compartmenting the eluent in accordance with the desired number of multiplex

qPCR reactions, and then transporting droplets of the PCR reagents to mix with the eluent droplets. Under the outlined approach, the IPF - DM integration should lead to a notably reduced turnaround and a hands-free “lysate-to-answer” operation.

As the first step towards such a diagnostic device, the primary objective of this thesis is to verify the feasibility of the IPF - DM integration. This is achieved in four phases. First, the suitable assays, fluidic device, and auxiliary systems are developed. Second, the extent of purification obtained per IPF wash, and hence the number of washes needed for uninhibited qPCR, are estimated via off-chip UV absorbance measurement and on-chip qPCR. Third, the performance of on-chip qPCR, particularly the copy number - threshold cycle correlation, is characterized. Lastly, the above developments accumulate to an experiment that includes the following on-chip steps: DNA purification by IPF, PCR mixture preparation via DM, and target quantification using qPCR - thereby demonstrating the core procedures in the proposed approach.

Conclusions It is proposed to expedite and automate qPCR-based multiplex sparse pathogen detection by combining IPF and DM on a fluidic device. As a start, this work demonstrated the feasibility of the IPF - DM integration. However, a more thermally robust device structure will be needed for later quantitative investigations, e.g., improving the bead - buffer mixing. Importantly, evidences indicate that future iterations of the IPF - DM fluidic device could reduce the sample-to-answer time by 75% to 1.5 hr and decrease the hands-on time by 90% to approximately 20 min.

Contents

Abstract	iv
List of Tables	ix
List of Figures	x
1 Introduction	1
2 Background and Motivation	4
2.1 Challenges of Sepsis Diagnosis	4
2.2 Cyberphysical System	6
2.3 Motivation	8
3 Technology Overview	11
3.1 qPCR Sequence Detection	11
3.1.1 PCR Theory	11
3.1.2 Quantitative PCR	12
3.1.3 Specificity Improvement	16
3.1.4 qPCR in Practice	17
3.2 Digital Microfluidic Droplet Actuation	19
3.2.1 Theory	19
3.2.2 Device Structure	21
3.2.3 Fluidic Operations	24
3.2.4 Aspect Ratio Optimization	25

3.3	Immiscible Phase Filtration	28
4	Approach	34
4.1	Nucleic Acid Purification Followed by qPCR Detection	34
4.2	PCR Preparation by DM Droplet Actuation	36
4.3	Nucleic Acid Purification by IPF	38
4.4	Interfacing IPF with DM	41
4.5	Advantages	42
4.6	General Workflow and Device Operation	44
5	Development of Assay, Fluidic Device and Auxiliary System	48
5.1	Assays	49
5.1.1	qPCR Assay	49
5.1.2	PCR Master Mix	55
5.1.3	Purification Assay	61
5.2	Fluidic Device	64
5.2.1	Layout and Structure	65
5.2.2	Heat-Resistant Plastic Top Plate	70
5.2.3	On-Chip Heater	75
5.3	Auxiliary Systems	82
5.3.1	Temperature Control	83
5.3.2	Device Holder	89
5.3.3	Fluorescence Sensing	94
5.4	Chapter Summary	102
6	Experimental Results	106
6.1	Estimation of Purification Power	106
6.1.1	Effect of GuSCN on PCR	107

6.1.2	GuSCN Concentration vs. Number of Washes	109
6.2	Demonstration of IPF - DM Integration	116
6.2.1	Threshold Cycle vs. Number of Washes	116
6.2.2	Nucleic Acid Retention	122
6.3	Performance of On-Chip qPCR	128
6.3.1	Amplification Efficiency	129
6.3.2	Limitations of Nucleic Acid Quantification	133
6.4	Chapter Summary	140
7	Future Work and Conclusions	142
7.1	Future Work	142
7.2	Conclusions	145
A	Experimental Methods	150
A.1	Effect of GuSCN on PCR	150
A.2	GuSCN Concentration vs. Number of Washes	151
A.3	Threshold Cycle vs. Number of Washes	153
A.4	Amplification Efficiency	155
A.5	Nucleic Acid Retention	157
B	Dye-Based Initial Evaluation of Immiscible Phase Filtration	160
B.1	Experimental Methods	160
B.2	Selection of the Immiscible Phase	161
B.3	Effect of Input Viscosity and Interfacial Tension	162
B.4	Effect of Bead Load on Purification Power	163
	Bibliography	164
	Biography	172

List of Tables

3.1	Thermocycling profile of TaqMan Fast Advanced Master Mix	17
3.2	Parameters used in the estimation of F_{EM} , F_{CLF}	26
4.1	Estimated total run time and hands-on time.	47
5.1	Comparison of two $\lambda_{abs} \sim 532$ nm fluorophores.	51
5.2	Alu Yb8 assay.	52
5.3	qPCR detection of Alu Yb8.	53
5.4	Comparison of master mixes.	56
5.5	Default thermocycling profile of master mixes.	56
5.6	Linear CTE, heat distortion temp. of the materials at the top plate. .	70
5.7	Top plate sheet resistance vs. baking.	74
5.8	Properties of the on-chip resistive heater.	78
5.9	Temperature ramp rate and PCR time.	85
5.10	Heat sinking effect of the aluminum device holder.	93
5.11	$T_{heater} - T_{drop}$ vs. layers of Kapton tape.	93
5.12	Properties of the custom-built fluorescence sensor.	98
6.1	PCR inhibition by GuSCN.	108
6.2	Peak absorption wavelength vs. GuSCN concentration.	111
6.3	Threshold cycle vs. number of washes.	119
6.4	Loss of NA retention due to unoptimized on-chip processes.	127
7.1	Estimated total run time and hands-on time.	149

List of Figures

2.1	Septic shock survival rate vs. time from hypotension onset.	5
2.2	Reroute a droplet to bypass a failed DM electrode.	8
2.3	Integration of DM device with annular thin-film photodetector.	10
3.1	Exponential amplification of DNA template.	13
3.2	qPCR of a 160 bp target.	14
3.3	TaqMan-based qPCR.	15
3.4	Layout of a DM device, top-down view.	19
3.5	Structure of a typical DM device, side view.	20
3.6	Electrowetting-on-dielectric.	21
3.7	Fluidic operations: Transport, split.	23
3.8	Fluidic operations: Merge, dispense.	23
3.9	DNA concentration measurement on DM device.	24
3.10	EM force, contact line friction vs. DM electrode pitch.	27
3.11	Fraction of the EM force available for droplet actuation.	27
3.12	DM electrode pitch, gasket thickness that correspond to 1 μ l droplet.	27
3.13	Schematic of an IPF device, top-down view.	30
3.14	Bead snapping under different interfacial tension conditions.	31
3.15	The linear correlation between bead weight and carryover volume.	31
4.1	Preparation of the PCR mixture droplet.	37
4.2	PCR on DM device.	38

4.3	Operation of the IPF - DM fluidic device.	44
4.4	Bead snapping, eluent droplet generation.	45
5.1	Amplification of a 176 bp segment in Alu Yb8.	54
5.2	Layout of Generation I fluidic device.	67
5.3	Generation I fluidic device.	67
5.4	Layout of Generation II fluidic device.	68
5.5	Generation II fluidic device.	68
5.6	Structure of Generation II fluidic device.	69
5.7	Cracking of ITO after 65 °C bake.	71
5.8	Cracking of ITO in ITO/PEDOT:PSS after 95 °C bake.	71
5.9	DM actuation remains functional after 40 thermocycles.	75
5.10	Photomask of Gen II fluidic device.	80
5.11	Used and damaged on-chip heater.	80
5.12	Heater failure due to the electrolysis of water.	81
5.13	Electrical contacts to Gen II fluidic device.	81
5.14	Temperature control system.	83
5.15	Thermocouple taped to a Gen II fluidic device.	85
5.16	PCR performed with the “Fast Ramp” set of PID parameters.	86
5.17	PCR performed with the “Slow Ramp” set of PID parameters.	86
5.18	Comparison of transient temperature ramp rate.	87
5.19	Temp. difference between two thermocouples vs. temp. ramp rate.	88
5.20	Deformed 3D-printed device holder.	91
5.21	3D-printed device holder with built-in thermocouple aligner.	92
5.22	Kapton tape on aluminum device holder.	92
5.23	Schematic of the custom-built fluorescence sensor.	97

5.24	Custom-built fluorescence sensor positioned on Gen II fluidic device.	97
5.25	Droplet detection using the fluorescence sensor.	100
5.26	Droplet leaving the fiber field-of-view.	101
6.1	PCR inhibition by GuSCN	109
6.2	Absorbance spectrum of 1.5 mM GuSCN.	110
6.3	Absorbance - GuSCN concentration standard curves.	111
6.4	Purification power and GuSCN conc. in eluent vs. number of washes.	113
6.5	Threshold cycle vs. number of washes.	119
6.6	Nucleic acid retention experiment: Floor plan and workflow.	123
6.7	Threshold cycle vs. nucleic acid retention.	125
6.8	On-chip qPCR amplification efficiency and Yb8 background.	130
6.9	Dust particle entering the device during thermocycling.	138
7.1	Nanosphere's nanoparticle-based sequence detection.	144
A.1	The device employed to measure the purification power.	152
B.1	An early PDMS-based IPF.	161

1

Introduction

This thesis represents the initial development of a fluidic device designed to reduce the sample-to-answer time of multiplex sparse pathogen detection, particularly in the case of sepsis diagnosis.

Septic shock is a severe form of bloodstream infection. Its diagnosis is challenging in part for two reasons. First, the infection could be caused by more than 50 species of pathogens [1]. Second, the pathogens may exist in the bloodstream in very low concentrations, e.g., less than 1 colony-forming unit/ml blood [2]. Consequently, depending on the method it might be necessary to analyze 3 ~ 20 ml of blood [2, 3]. In turn, these difficulties of identifying the pathogens translate to inadequate and delayed treatments. The median time to receive an effective antimicrobial therapy is 6 hr after hypotension onset. By then, the survival rate has dropped at an average of 7.6%/hr to 42% [4].

Importantly, among the current sepsis diagnostic methods there exists a trade-off between the assay time and the specificity of the derived diagnostic information. Situated between the two extremes (blood culture and biomarker detection) is pathogen DNA quantification. For instance, the qPCR-based SeptiFast test measures the DNA

of 25 pathogens with a turnaround of $6 \sim 10$ hr [5], which includes a lengthy hands-on time of 3 hr [6]. Such timescale remains unsatisfactory relative to the aforementioned rapid decrease in the survival rate.

Therefore, this work aims to take advantage of the advances in microfluidic technologies to expedite and automate the detection of sparse pathogens in a large-volume biofluid. Specifically, this improvement is evaluated to be best approached by combining immiscible phase filtration and digital microfluidic droplet actuation to enhance nucleic acid purification and qPCR sequence detection, respectively. Thus, the primary objective herein is to demonstrate the feasibility of the proposed integration.

This thesis details the developments en route to this main objective. It is structured as follows:

Chapter 2 The motivations and the objectives of this research are further elaborated.

Chapter 3 The three technologies that are tightly related to this work will be reviewed: qPCR sequence detection, digital microfluidic droplet actuation, and immiscible phase filtration.

Chapter 4 This chapter examines how the two microfluidic technologies could be combined to enable a short sample-to-answer time and a high degree of automation.

Chapter 5 The developments that lead to the experiments in Ch. 6 are discussed, including the evaluation of the three assays, the improvements applied to the fluidic device, and the construction of the auxiliary systems needed for qPCR execution.

Chapter 6 This chapter presents the results from the wet experiments. Based on the experimental method, the chapter is divided into three parts:

- In Sec. 6.1, the effectiveness of on-chip purification is assessed by off-chip measurements.
- In contrast, in Sec. 6.2, on-chip purification is followed by on-chip qPCR, thereby demonstrating the feasibility of the IPF - DM integration.
- The performance of on-chip qPCR is discussed in Sec. 6.3.

Chapter 7 The key results are recited in the last chapter of this thesis.

Appendix A The experimental methods used in Ch. 6 are detailed.

Appendix B The initial dye-based evaluation of IPF is summarized.

Background and Motivation

Taking septic shock as an example disease, this chapter will first examine the challenges of multiplex sparse pathogen detection and the importance of having a short assay time and an automated workflow. Then, the other backdrop of this work, augment a fluidic device with cyberphysical control to enhance the execution of a bioassay, would be overviewed. Finally, the objectives of this investigation will be specified in the last section of the chapter.

2.1 Challenges of Sepsis Diagnosis

Septic shock is a severe form of bloodstream infection. It has an overall mortality rate of 56% [4]. Further, since the increase in invasive medical procedures inevitably exacerbates the likelihood of hospital-acquired infections, the incidence of septic shock has been climbing and amounts to 10% of all admissions to the intensive care unit [7].

The diagnosis of severe sepsis and septic shock are challenging in part for two reasons. First, the infection can be caused by more than 50 species of pathogens

that include Gram positive bacteria 47%, Gram negative bacteria 62%, and fungi 19% (based on the patients who had positive cultures [1, 7].) Second, the pathogens might exist in the bloodstream in very low concentrations, e.g., less than 1 colony-forming unit/ml blood [2]. Consequently, depending on the method it might be necessary to analyze 3 ~ 20 ml of blood [2, 3]. As indicated by the two problems, definitive pathogen identification involves the multiplex detection of sparse pathogens from a large-volume biofluid.

In turn, the difficulties of identifying the pathogens translate to inadequate and delayed treatments. As can be seen in Fig. 2.1, the median time to receive an *effective* antimicrobial therapy is 6 hr after hypotension onset. By then, the survival rate has dropped at an average of 7.6%/hr to 42% [4].

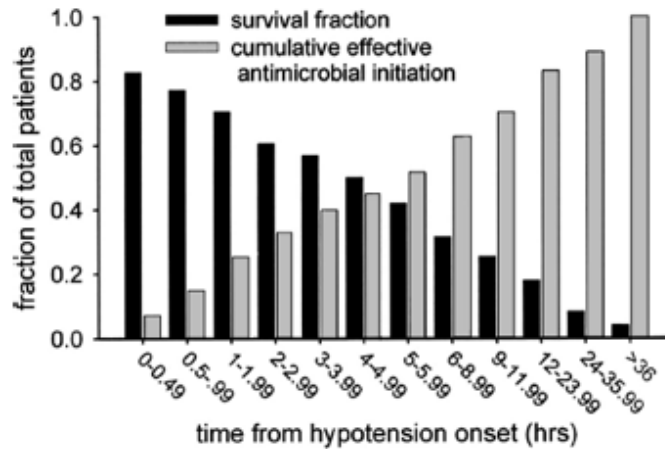


FIGURE 2.1: Septic shock survival rate vs. time from hypotension onset [4].

The gold standard of sepsis diagnostic methods is the blood culture. It indicates the species, concentrations, and antibiotic resistance of viable pathogens. However, definitive pathogen identification takes at least 24 ~ 48 hr on automated systems - far longer than the aforementioned 6 hr timescale [6, 8].

In contrast, biomarker-based methods generally have a shorter assay time but provide relatively unspecific data. For example, by measuring the protein procal-

citonin in plasma, the VIDAS BRAHMS PCT test shows the severity of bacterial infection in 20 min [9]. Still, these biomarkers are common to many inflammation types and can be found in simple infections [8].

In terms of the assay time and the usefulness of the derived diagnostic information, the molecular diagnostic approach that uses qPCR or microarray to quantify the DNA of 25 ~ 50 pathogens [3, 10] is situated between culturing and biomarker detection. Molecular diagnostic tests generate the same types of information as the blood culture, albeit in most cases without the specificity to viable pathogens. Additionally, a significant drawback is the considerable hands-on time. For example, the qPCR-based SeptiFast test has an average turnaround of 6 hr, which includes a hands-on time of 3 hr [6]. Also, as a related issue, the delay caused by the operator has been observed to further prolong the assay time to 10 hr [5].

In summary, certain approaches to sepsis diagnosis involve the multiplex detection of sparse pathogens from a large-volume biofluid. Culturing is indispensable but is growth rate-limited. In relation to the rapid deterioration of survival rate in severe sepsis and septic shock, it remains to be seen to what extent the DNA-based diagnostic methods could be expedited and automated by the advances in fluidic technologies.

2.2 Cyberphysical System

A cyberphysical system is a system that involves computational entities interacting with the physical world via interrelated sensors and actuators. An example is an autonomous car that uses lidar mapping to stay on the road and preemptively diverts from the planned route based on the real-time traffic data.

Recently, digital microfluidic devices (DM) have become sufficiently sophisticated to be considered as basic cyberphysical systems. For instance, a PID controller can

utilize the feedback from on-chip capacitive sensors to rapidly modulate the voltage applied to the DM electrodes involved in the generation of droplets. The volume variation of the droplets produced by this system can be controlled within $\pm 1\%$ [11]. Another demonstration tapped a commercial thin film transistor technology to expand the impedance sensing capability to all DM electrodes. Hence, the position and volume of all droplets on the fluidic device can be simultaneously monitored [12]. This ability can then be used to validate the droplet operations in a bioassay and automatically react to a failed step, e.g., undo an uneven splitting of a microdrop into two droplets.

However, since the implementation of a fluidic device can be highly application-driven, an “electronics-first” approach may be less adaptable. In contrast, this work represents the initial phase of a larger project that attempts to construct a cyberphysical system that enhances the execution of real-world bioassays. This goal is thought to be best achieved via the co-development of the fluidic device, control algorithms, and sensors, e.g., on-chip photodetector, capacitive droplet position sensor. (Algorithm: Chakrabarty group, photodetector: Jokerst group, capacitive sensor: Chakrabarty/Fair group.)

Below are two examples of what could be implemented in this cyberphysical system:

- Dynamically instantiated error recovery: As illustrated in Fig. 2.2, the droplets could be rerouted to bypass a failed DM electrode. The preliminary demonstration of this capability is summarized in [13].
- Dynamic adaptation to intermediate qPCR results: For instance, as soon as the qPCR detection of *S. aureus* shows positive amplification, the qPCR detection of methicillin-resistant *S. aureus* could be initiated without waiting for the preset number of thermocycles to finish.

It can be seen that these features would be required for mission-critical applications that demand the fastest sample-to-answer time, e.g., sepsis diagnosis.

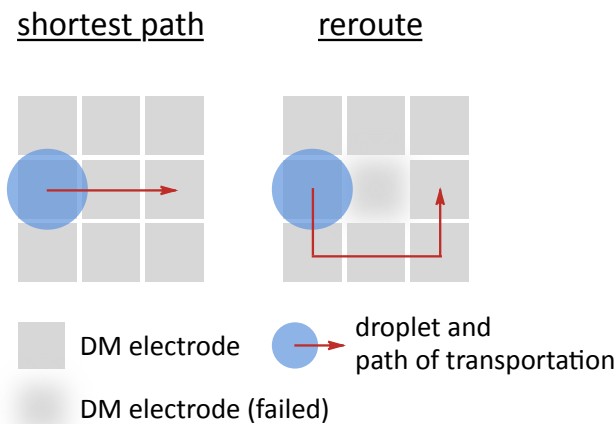


FIGURE 2.2: Reroute a droplet to bypass a failed DM electrode.

2.3 Motivation

The discussion in Sec. 2.1 indicates that among the current sepsis diagnostic tests there is an inevitable tradeoff between the sample-to-answer time and the usefulness of the generated diagnostic information. However, this tradeoff is costly given the rapid deterioration of survival rate in severe sepsis and septic shock. Located somewhat in the middle of the two extremes is combining nucleic acid purification and qPCR sequence detection to quantify the pathogen DNA. Still, a step-by-step evaluation of the workflow of the commercial SeptiFast test shows that there is a considerable room for improvement in its assay time and hands-on time.

The example of sepsis diagnosis further exposed an ironic deficiency in contemporary lab-on-a-chip research: the majority of demonstrations are focused on enhancing a particular procedure but without regard to its parent multistep workflow. Thus, the claimed advances would be immaterial in practice if the approach is incompatible with the intended upstream and downstream processes, e.g., in terms of flow rate,

sample volume, and analyte concentration.

In light of the above issues, this work will attempt to demonstrate a key concept that could lead to a sepsis diagnostic device with a short sample-to-answer time and a high degree of automation. Importantly, rather than electing to optimize a particular process, fluidic technologies would be applied to expedite and automate the entire workflow. To this end, the five objectives of this investigation are specified below:

- Identify a compatible set of fluidic technologies that can be combined to expedite and automate nucleic acid purification and qPCR sequence detection. Importantly, although a full-fledged diagnostic device is beyond the scope of this project, the employed approach nonetheless should be scalable to meet the demands of sepsis diagnosis, i.e., sample volume and the number of multiplex qPCR reactions. – Ch. 4
- Uphold the feasibility of the proposed integration of fluidic technologies by performing basic purification and qPCR tasks on the developed device. – Ch. 6
- Construct the auxiliary systems necessary for the operation of the fluidic device, i.e., temperature control and fluorescence sensing systems. This task should not be overlooked because commercial solutions can be cost prohibitive or incompatible with the custom fluidic device. – Ch. 5
- Characterize the performance and identify the deficiencies of the initial fluidic devices. The information can then be used to facilitate the subsequent design revisions. – Ch. 6
- As the initial phase of a larger project that seeks to evolve the fluidic device into a cyberphysical system, provisions will be made in the designs of the device

and the assays to prepare for the later incorporation of additional sensors, e.g., the thin-film photodetector sketched in Fig. 2.3. – Ch. 5

Considering the steps involved, an aggressive yet achievable target might be improving from the present 6 hr / 3 hr assay time/operator time to better than 1 hr / 0.3 hr. Such improvement may double the survival rate of septic shock from 42% to 80% [4]. This work then represents the first step towards this long-term goal.

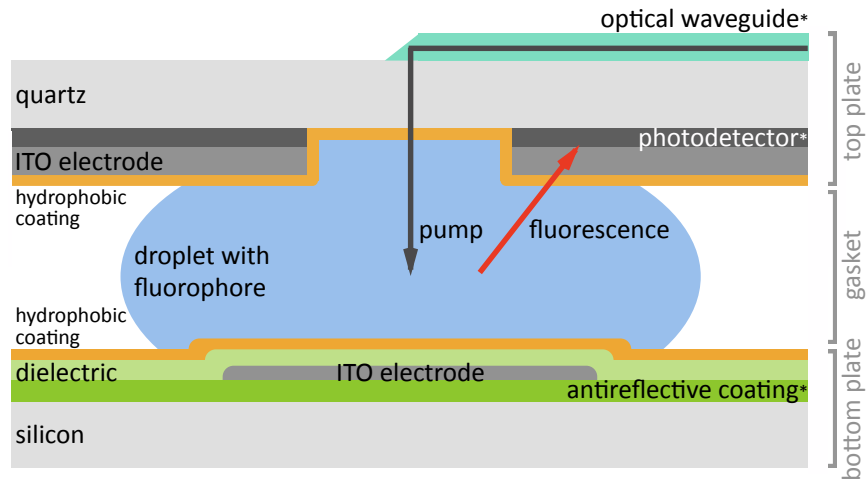


FIGURE 2.3: Integration of digital microfluidic device with annular thin-film photodetector (starred.)

Technology Overview

This chapter will overview the three technologies that are tightly related to this work. First, because of its relevance to all aspects of the project, a longer section is dedicated to quantitative polymerase chain reaction (qPCR.) Then, the review on digital microfluidic droplet actuation (DM) will focus on the realizable fluidic operations. Lastly, the discussion on immiscible phase filtration (IPF) will emphasize its workflow and a qualitative evaluation of the main factors that affect the effectiveness of purification.

3.1 qPCR Sequence Detection

3.1.1 PCR Theory

Polymerase chain reaction (PCR) is a biochemical method that exponentially amplifies the amount of a DNA template. As illustrated in Fig. 3.1, a basic PCR cycle consists of three steps: (1) Denaturation: at elevated temperature the hydrogen bonds between complementary bases are broken, unwinding a double-stranded DNA to two strands. (2) Annealing: the temperature is lowered to allow for the

hybridization of a primer to its target sequence at the 3' end of each strand. (3) Extension: using dNTPs as building blocks, the hybridized primer is extended by a DNA polymerase to become a complement of the original strand.

Since a replicate of the dsDNA template is formed from each of the two initial strands, after the first cycle there are now two templates. Then, the cycle is repeated. Assuming 100% amplification efficiency, the amount of a template would be doubled each cycle (Eq. 3.1.)

$$C_n = C_i(1 + E)^n \quad (3.1)$$

(C_i , C_n : initial copy number and copy number at cycle n , E : amplification efficiency.)

In practice, exponential amplification cannot be sustained indefinitely. For instance, in Fig. 3.2 it can be seen that there are only approximately 35 cycles in the exponential phase. This is in part due to the exhaustion of dNTPs, and the thermal degradation of the polymerase (*Taq* polymerase, a DNA polymerase frequently used in PCR, has a half-life of 45 min at 95 °C [14].) Afterwards, as the accumulation of nonspecific amplicons promotes further generation of nonspecific amplicons (that is, PCR products), a negative feedback cycle is formed that rapidly terminates the chain reaction. Eventually, PCR is ceased because of the aforementioned reasons.

3.1.2 Quantitative PCR

After PCR, the products are traditionally examined by gel electrophoresis [16]. However, due to its inadequate detection limit and dynamic range, gel electrophoresis is unsuitable for quantifying the final amplicon concentration. This issue is exacerbated by the fact that gel electrophoresis might be incapable of discriminating specific amplicons from nonspecific ones. As a consequence, under this approach it is difficult to infer the initial template concentration. Further, as a separate step performed after PCR, gel electrophoresis adds to the already lengthy sample preparation and PCR time.

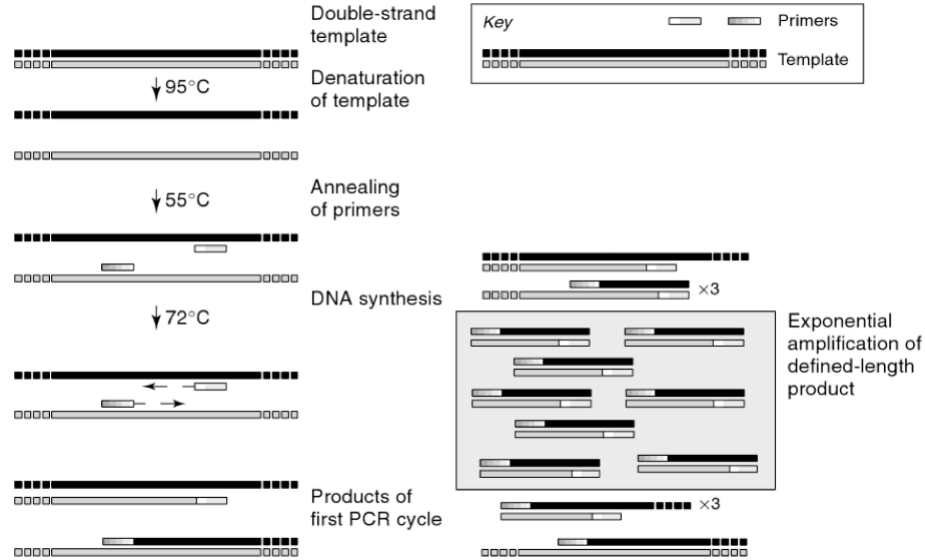


FIGURE 3.1: Exponential amplification of DNA template [15]. Left: the first PCR cycle. Right: products of the fourth cycle.

To address the above drawbacks, quantitative PCR (qPCR) is developed. In qPCR, via the use of fluorogenic probes or intercalating dyes, PCR progress can be monitored by a photodetector in real-time. Hence, initial template concentration is correlated with threshold cycle C_t , the number of PCR cycles to reach a threshold fluorescence intensity. Lower C_t implies higher initial concentration. Also, absolute initial template concentration can be estimated from a $C_t - \log(C_i)$ standard curve (Fig. 3.2.)

Notably, threshold intensity should be sufficiently low such that it can be reached while an amplification is still in the exponential phase. Thus, in contrast to end-point measurements such as gel electrophoresis, C_t and the subsequent estimation of initial template concentration would not be distorted by nonspecific amplicons generated after the exponential phase.

In addition to initial template concentration, the other information that can be extracted from a standard curve is amplification efficiency. Specifically, via Eq. 3.2 amplification efficiency can be calculated from the slope of the standard curve. As

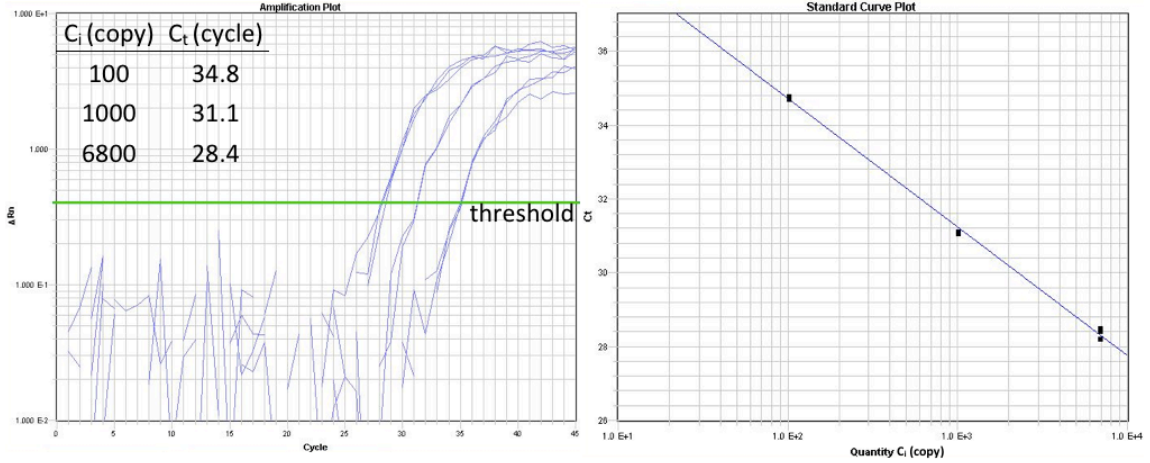


FIGURE 3.2: qPCR of a 160 bp target. Left: amplification plot. ΔR_n is obtained by (reporter dye fluorescence / reference dye fluorescence) - baseline. Right: standard curve with $E = 94\%$.

defined in Eq. 3.1, an ideal efficiency of 100% suggests that the amount of amplicons is doubled per PCR cycle. In reality, a well-designed and executed PCR reaction should achieve better than 90%. Moreover, because amplification efficiency is affected by all aspects of PCR, when fine-tuning a new PCR reaction a satisfactory efficiency could be seen as a telltale sign of an optimized chemistry. Similarly, amplification efficiency might be used as a debugging tool. As an example, for a routine PCR reaction, the deviation of amplification efficiency from typical values (overly low or abnormal, e.g. higher than 110%) may indicate the presence of PCR inhibitors in reaction mixtures.

$$E = 10^{\frac{-1}{\text{slope}}} - 1 \quad (3.2)$$

(E: amplification efficiency, slope: slope of the standard curve.)

Regarding the generation of fluorescence in qPCR, a frequently used mechanism is TaqMan chemistry (Fig 3.3.) In principle, a basic PCR can be converted to a TaqMan-based qPCR by adding an appropriate TaqMan probe. TaqMan probe is a type of fluorogenic probe that consists of three components: A < 30 nt nucleotide complementary to a region of the amplicon, a fluorophore attached to the 5' end of

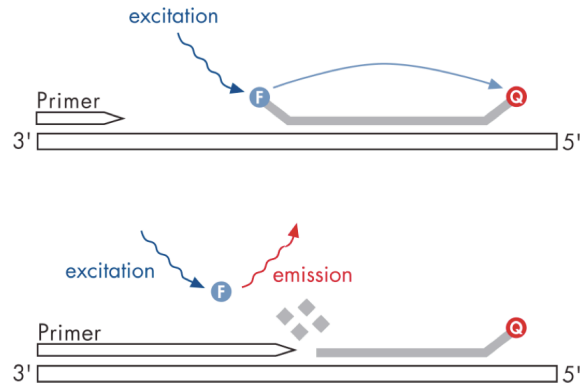


FIGURE 3.3: TaqMan-based qPCR. During extension, a DNA polymerase extends the primer. When the enzyme reaches the probe, due to its $5' \rightarrow 3'$ exonuclease activity the fluorophore is cleaved from the probe [17].

the nucleotide, and a quencher attached to the 3' end of the nucleotide. Prior to PCR, fluorescence emitted by the fluorophore is quenched via fluorescence resonance energy transfer by the quencher. During annealing, a probe hybridizes to its target sequence on a ssDNA. Then, in the extension step of PCR, the probe is digested by the DNA polymerase as it extends the primer. Accordingly, the fluorophore is irreversibly cleaved from the quencher, and the fluorescence is unquenched. In other words, each duplication of a dsDNA template would generate two amplicons and unquench one fluorophore. Therefore, the amount of amplicons accumulated in a reaction mixture is proportional to fluorescence intensity.

The above discussion highlights three features of probe-based qPCR. First, a set of two sequence-specific primers can be designed to selectively amplify a target. Second, extra specificity is introduced by the sequence-specific probe. Because fluorescence can only be generated by the amplification of targets, but not by unintended amplifications, e.g. due to mispriming. Third, initial target concentration can be determined from the threshold cycle. Because of these attributes, probe-based qPCR is an attractive method for quantifying sparse targets that are buried in high levels of background nucleic acids.

Importantly, multiplex detection can be attained by running multiple assays (an assay includes a set of two primers and a corresponding probe) concurrently in the same reaction mixture. One of the prerequisites for multiplexing is that each target should be represented by a fluorophore that is spectrally distinct from the fluorophores associated with other targets. Meanwhile, a photodetector needs to be able to suppress the excitation light and resolve the emission contributed by each type of the fluorophore. Consequently, the degree of multiplexing is limited by the availability of suitable fluorophores and optical filtering. Commercial qPCR instruments are typically equipped with sufficient fluorescence channels to support the sensing of three to six targets.

3.1.3 Specificity Improvement

Hot start is a technique that substantially improves the specificity of amplification. Essentially, it is devised to prevent the amplification of misprimed ssDNA and primer dimer during PCR preparation and while a reaction mixture is being heated up from room temperature to the first denaturation step. This type of nonspecific amplification is attributed to two undesirable effects. First, at low temperature (compared to the melting temperatures of primers), the annealing of primers suffers from poor stringency, and primer dimer is relatively stable. Secondly, *Taq* polymerase - a frequently employed DNA polymerase - is somewhat active at room temperature: 0.25 nt/s extension rate [18]. Together, the two effects would produce nonspecific amplicons even before the first PCR cycle, and these nonspecific amplicons might be further replicated by PCR. In turn, the specificity of amplification is compromised.

As the name implies, hot start PCR is initiated by a high-temperature step that activates the DNA polymerase. Otherwise, prior to the thermal activation the DNA polymerase has no enzymatic activity at ambient temperature. This temporary enzyme inactivation can be achieved by, for example, binding or blocking the active

Table 3.1: Thermocycling profile of TaqMan Fast Advanced Master Mix [19].

Temp. (°C)	Duration (s)	Step
50	120	UNG incubation
95	20	Polymerase activation
95	1	Denature
60	20	Anneal/extend, fluorescence measurement

domain of DNA polymerase with antibody or oligonucleotide. During PCR preparation, because DNA polymerase is inactive, misprimed ssDNA and primer dimer cannot be amplified. Later, DNA polymerase is activated, but at proper annealing and extension temperatures the probability of mispriming and the stability of primer dimer are greatly diminished.

Therefore, hot start minimizes the introduction of “noise” to a sample. In turn, less “noise” is likely to be amplified by PCR, thereby enhancing the specificity of amplification. In the context of qPCR, hot start decreases the presence of potentially amplifiable false positives in a sample, resulting in a more accurate quantification of targets.

3.1.4 qPCR in Practice

A baseline qPCR protocol is listed in Table 3.1. This two-temperature protocol assumes that the melting temperatures of primers are designed to be approximately 60 °C. Thus, instead of involving a dedicated 72 °C extension step, annealing, extension, and fluorescence measurement are combined into one 60 °C step, resulting in significantly reduced PCR run time. Although functioning at a reduced extension rate, 20 s anneal/extend at > 24 nt/s is sufficient for extending a typical < 150 bp qPCR amplicon (> 60 nt/s at 70 °C [18].)

A qPCR reaction mixture is assembled from three components: sample, assay, and master mix. A master mix contains DNA polymerase, dNTPs, Mg²⁺, K⁺, pH

buffer, and other additives. In particular, the master mixes intended for Applied Biosystems's qPCR instruments generally contain the passive reference dye ROX. The dye does not participate in PCR. Rather, it is used to detect non-PCR-originated fluctuations in the fluorescence signal, e.g. due to well-to-well volume variations.

Importantly, the concentration of PCR inhibitors in a sample should be kept low. Otherwise, targets might be undetected due to failed PCR, leading to false negatives. For instance, whereas hemoglobin concentration in blood is on the order of 100 mg/ml, PCR has been shown to be completely inhibited at 1 mg/ml [20].

Because multiple assays can be employed to detect more than one target in a sample, internal positive control DNA (IPC DNA) and its corresponding assay are frequently used to assist the identification of false negatives. Briefly, prior to PCR a low concentration of IPC DNA is added to a sample. Later, if IPC is undetected, or is detected with a significantly delayed threshold cycle, then the extent of PCR inhibition should be evaluated before true negative can be declared.

Similarly, a no template control (NTC) should be performed alongside a sample. NTC is prepared by adding water - instead of sample - to a reaction mixture. If a target is detected in NTC, the PCR reagents could be contaminated with the target. Accordingly, positive detection in samples may in fact be false positives. Alternatively, NTC might be inadvertently contaminated during PCR preparation, for instance via aerosols generated by pipetting [21].

Nevertheless, depending on the target of interest, amplified NTC could be unavoidable. For example, since the recombinant *Taq* polymerase is manufactured by inserting the DNA polymerase gene of *T. aquaticus* into an *E. coli* host [22], per unit enzyme it can contain 10^2 to 10^5 genome equivalents of bacterial DNA [23]. Thus, qPCR-based *E. coli* detection is usually encumbered by high background and unsatisfactory detection limit, e.g. 2500 CFU/ml [24]. Even if *Taq* polymerase is further purified to reduce the bacterial DNA introduced from the host, a "clear"

NTC is still difficult to obtain [23].

3.2 Digital Microfluidic Droplet Actuation

Three topics will be overviewed in this section: the theory behind DM actuation, the structure of a DM-based device, and the fluidic operations that can be executed on the device. In particular, the discussion will focus on the aspects that are directly relevant to this work. More comprehensive reviews can be found in [25] and [26].

3.2.1 Theory

Digital microfluidic droplet actuation (DM) is a liquid handling technology that is used to control the motion of conductive droplets on an electrode array (Fig. 3.4), primarily for lab-on-a-chip purposes. Instead of a pump, the actuation force originates from the bias applied between the DM electrode and the ground plane, as sketched in Fig. 3.5.

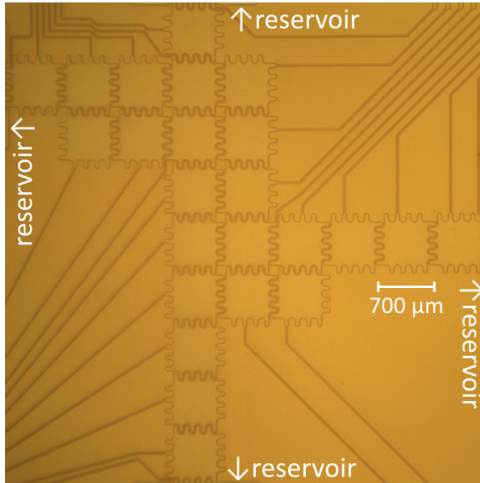


FIGURE 3.4: Layout of a DM device, top-down view.

At low frequency (below ~ 10 kHz [25]), the applied voltage results in an electrostatic pressure that pulls the liquid - fluid interface in the proximity of the triple

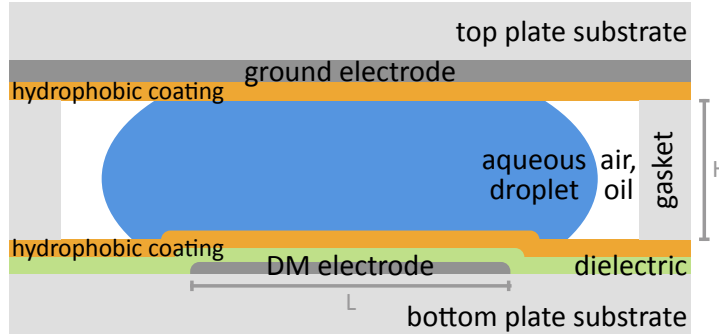


FIGURE 3.5: Structure of a typical DM device, side view.

phase line (specifically, the interface within a distance of order d from the triple phase line [27]) in the direction of the outward (droplet) surface normal (Fig. 3.6.)

After integrating the electrostatic pressure over the droplet surface, the horizontal component (i.e., parallel with the substrate) of the obtained electromechanical force under relevant conditions amounts to 10s of μN [25], which is sufficient to overcome the frictional and viscous dissipation terms (former: contact line friction; latter: the flow in the droplet and in the filler medium) and pull the liquid - fluid interface (thus, the droplet) towards the energized DM electrode, e.g., Fig. 3.7.

This driving force scales in the same way as the energy stored in the dielectric: $\epsilon_r V^2/d$. (ϵ_r , d : relative permittivity and thickness of the dielectric; V : applied voltage.) Hence, the applied voltage can be utilized to increase the droplet transportation speed. In practice, the actuation force is observed to fall from the V^2 dependency well before the dielectric reaches its breakdown field strength. The exact causes of the saturation are not currently well understood [25].

Further, by affecting the Laplace pressure, another consequence of the electrostatic pressure is a reduced apparent contact angle θ_a . Fig. 3.6 illustrates this electrowetting-on-dielectric effect, $\theta_y = \theta_a(0) > \theta_a(V)$. However, it is important to note that the reduced apparent contact angle does not imply the liquid - solid interfacial tension is lowered by the voltage. Indeed, the same local contact angle

θ_y (again, within a distance of order d from the triple phase line) as governed by Young's equation is observed with or without the bias [28].

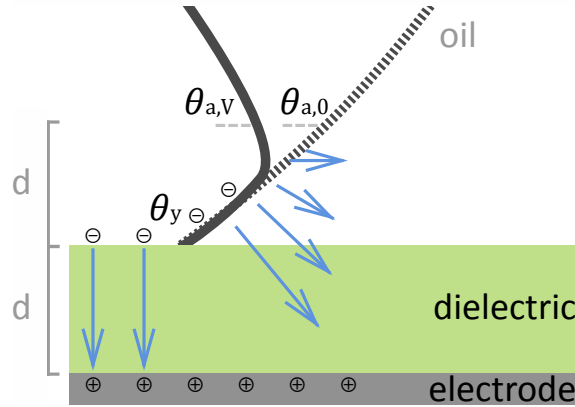


FIGURE 3.6: Electrowetting-on-dielectric. Solid / dotted curve: Liquid - fluid interface with / without an applied voltage. Arrow: Electric field. d is typically on the order of $1 \mu\text{m}$. Also, note that to transport the droplet via the electromechanical force towards the right, the depicted DM electrode would be the one that is adjacent to the electrode where the droplet currently resides on, see Fig. 3.7.

3.2.2 Device Structure

Fig. 3.5 illustrates the structure of a baseline DM device. Also, Fig. 5.6 shows the materials and the layer thicknesses employed by the main fluidic device in this work.

The aspect ratio L / H strongly depends on the targeted application and the available fabrication tools. Ratios between $4 \sim 25$ have been used [29, 30]. (L : DM electrode pitch; H : gasket thickness.) For a given droplet volume, a higher aspect ratio permits a larger portion of the liquid - fluid interface to be influenced by the electromechanical force. Hence, a higher ratio to certain extent could benefit DM actuation, especially for steps such as generating and splitting a droplet [31].

Regarding the largest droplet that might be reliably transported using DM actuation, with $L = 2.7 \text{ mm}$ (capillary length of water) and $H = 300 \mu\text{m}$ or $675 \mu\text{m}$ (limited by the thickest SU-8 gasket that can be fabricated with reasonable through-

put or the lowest reported aspect ratio, respectively) the volume would approximate $\pi(L/2)^2H = 2 \sim 4 \mu\text{l}$.

In comparison, the main device in this work has $L / H = 700 / 120 \mu\text{m}$ and a unit droplet volume of 46 nl. (For the structure shown in Fig. 2.3, the light tracing simulation conducted by the Jokerst group suggests that a suitable balance between the droplet's exposure to the excitation light and the probability of the resulting fluorescence reaching the photodetector may be obtained with $L / H = 700 / 160 \mu\text{m}$. However, to improve the fabrication throughput, the current gasket is laser-patterned from 120 μm -thick SecureSeal, a double-sided adhesive film.)

The typical bottom plate substrates include glass, silicon, and PCB. As for the top plate substrate, since optical observation is usually conducted from the top, transparent materials such as glass, polycarbonate, and PMMA are common. (For the same reason, the ground plane is generally made of the transparent conductive oxide ITO.) In particular, polymers and the associated manufacturing technologies (e.g., CNC milling, laser cutting, and injection molding) are relatively accessible. These methods enable the pipette ports, reagent reservoirs, and other chip-to-world interfaces to be incorporated as part of the top plate, e.g., Fig. 5.5. Still, compared with glass, the trade-offs are optical clarity, chemical inertness, and thermal stability.

Lastly, the filler medium should be electrically insulating and compatible with the application in question. That is, it must be immiscible with the reagents, must minimize analyte partitioning, and be thermally stable. Further, due to the small droplet volume, it is crucial to mitigate evaporation. Thus, although air satisfies most of the aforementioned criteria, inert oils such as dodecane and $2 \sim 5 \text{ cS}$ low viscosity silicone oil are more frequently employed.

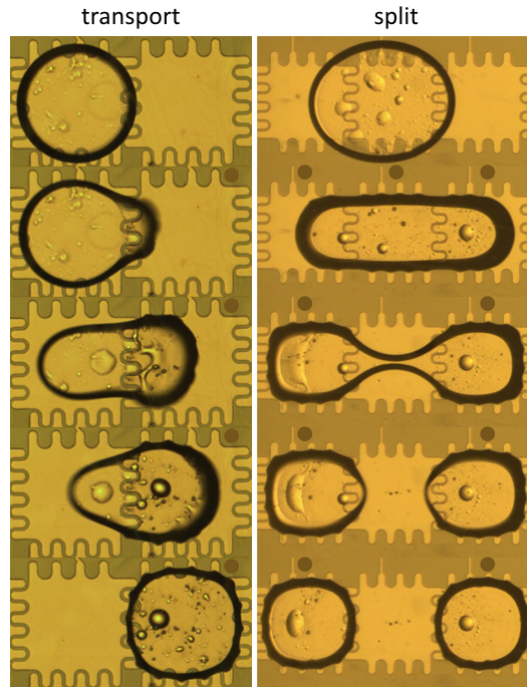


FIGURE 3.7: Fluidic operations: Transport, split. \odot : energized electrodes.

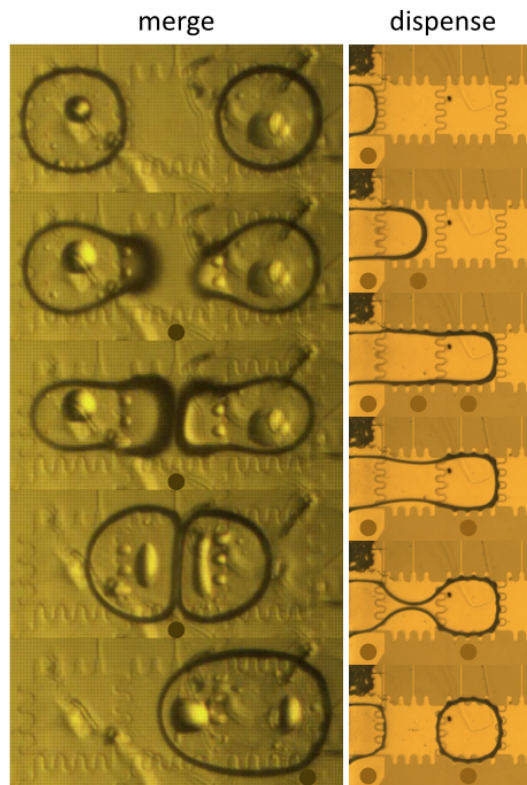


FIGURE 3.8: Fluidic operations: Merge, dispense from a reservoir. \odot : energized electrodes.

3.2.3 Fluidic Operations

On an electrode array, by energizing different sets of DM electrodes in sequence, the electromechanical force can be utilized to transport and split a microdrop. Based on the two basic fluidic operations, steps such as merging, dispensing, and mixing can be performed. Micrographs of these operations are shown in Fig. 3.7 and Fig. 3.8. (Merge: Transport droplets to the same location. Dispense: Split a droplet from a reservoir. Mix: A combination of merge, transport, and split are repeated to counter the lack of turbulent mixing at $Re \sim 0.4$.)

As an example, on the device illustrated in Fig. 5.6, the typical voltage used to transport an aqueous droplet of 0.08% w/v Tween 20 is 35 V_{rms} at 1 kHz. At this voltage, the droplet can be moved at 5 electrode/s, or 3.5 mm/s.

In turn, the five fluidic operations can be blended to execute a variety of reactions. For instance, Fig. 3.9 illustrates the measurement of ssDNA and dsDNA concentrations. Importantly, since the application of the actuation voltage to the

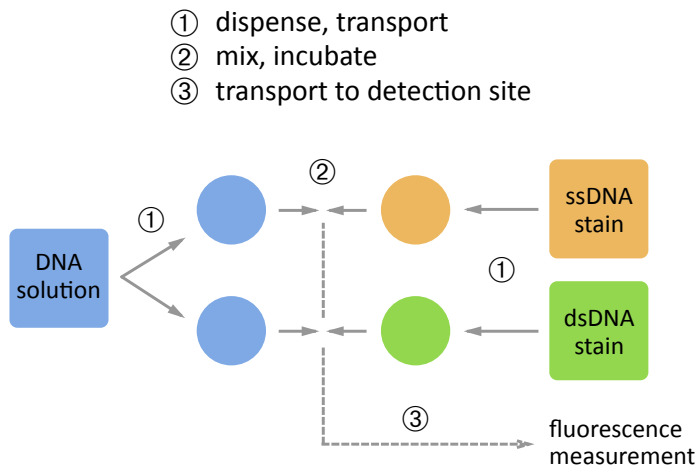


FIGURE 3.9: ssDNA, dsDNA concentration measurement performed via DM actuation.

DM electrodes is computer-controlled, the two procedures in Fig. 3.9 can be conducted on the same device automatically and concurrently. Hence, hands-on time

and the chance of contamination are minimized. In this work, these advantages of DM actuation will be used to automate and expedite the preparation of PCR reaction mixtures (Fig. 4.1 and Fig. 4.2.)

Lastly, it should be noted that DM actuation by itself is incapable of separating particles (such as cells, proteins, nucleic acids) from the droplet they reside in. This crucial deficiency can be circumvented by binding the particles to, for example, magnetic beads or a functionalized patch of the droplet-facing surface [32, 33]. After anchoring the magnetic beads in place with an external magnet, the droplet can be transported away from the beads. Subsequently, the process can be reversed to resuspend the particles in a new medium.

The outlined procedure can be adapted to purify nucleic acids from a solution of contaminants, or replenish the nutrients for an on-chip cell culture. Still, due to the constraint on the maximum droplet volume (Sec. 3.2.2), this approach cannot efficiently purify nucleic acids from a large-volume sample, i.e., larger than 4 μl . Instead, alternatives such as immiscible phase filtration (Sec. 3.3) would be more viable for this task.

3.2.4 Aspect Ratio Optimization

Using a unit droplet volume of 1 μl as an example, this section will outline an approach for sizing the DM electrode pitch and the gasket thickness with respect to maximizing the droplet transportation speed for temperature zone PCR purposes. In particular, the analysis is based on the theoretical estimation of the electromechanical droplet actuation force and the contact line friction, whereas practical limitations, such as the difficulty of fabricating a thick gasket ($> 300 \mu\text{m}$), will not be considered.

In temperature zone PCR (Fig. 4.2), the temperature ramp rate can be improved by increasing the average droplet transportation speed U . Thus, the goal of this section is to facilitate the droplet transportation by selecting a suitable combination

of DM electrode pitch L and gasket thickness H (Fig. 3.5.)

Based on the discussion in [34], the electromechanical droplet actuation force F_{EM} and the contact line friction F_{CLF} might be approximated by the following equations:

$$F_{EM} = \frac{\varepsilon_0 \varepsilon_r}{2d} (V - V_t)^2 L \quad (3.3)$$

$$F_{CLF} = \zeta U (2\pi \frac{L}{2}) \quad (3.4)$$

Table 3.2: Parameters used in the estimation of F_{EM} , F_{CLF} .

Parameter	Value
Relative permittivity of the dielectric ε_r	3.15 (Parylene C)
Thickness of the dielectric d	1 μm
Applied voltage V	35 V
Threshold voltage V_t	13.2 V ¹
Contact line friction coefficient ζ	4×10^{-2} kg/(m·s) ¹
Average droplet speed U	5L/s

¹ Adapted from [34].

According to Eq. 3.3, F_{EM} scales with L . By intuition, for a given droplet volume, a higher ceiling of U may be obtained by increasing L to maximize the F_{EM} available for pulling the droplet. However, as shown in Fig. 3.10, this intuition is only valid up to a certain L . Specifically, this is because the primary dissipation term in the system, F_{CLF} , scales with $U \times L$ and hence L^2 (Eq. 3.4.) Accordingly, beyond a certain L F_{CLF} will begin to scale faster than F_{EM} . Then, less net force $F_{EM} - F_{CLF}$ would be available for DM droplet manipulation. (Note that the factor 2 at the end of Eq. 3.4 is intended to account for the contact line at the two plates.)

In the case of Fig. 3.10, the maximum net force is obtained at $L = 2.6$ mm. Consequently, 1 μl unit droplet volume can be achieved by having $H = 190$ μm (Fig. 3.12.) As a comparison, this aspect ratio $L / H = 14$ falls in the middle of the reported $4 \sim 25$ range [29, 30]. In addition, as can be seen in Fig. 3.11, it is worth

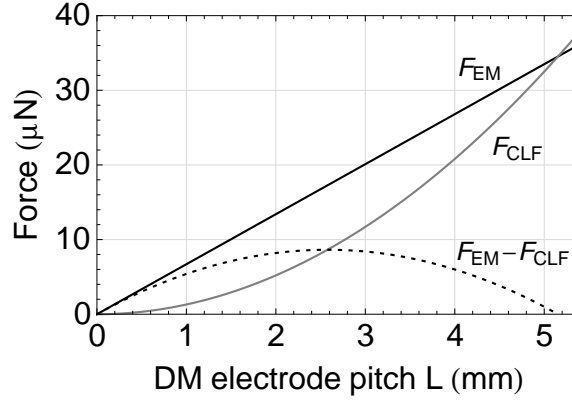


FIGURE 3.10: Electromechanical force (F_{EM}), contact line friction (F_{CLF}) vs. DM electrode pitch (L .) The estimation of F_{CLF} assumes an average droplet transportation speed of $5L/s$.

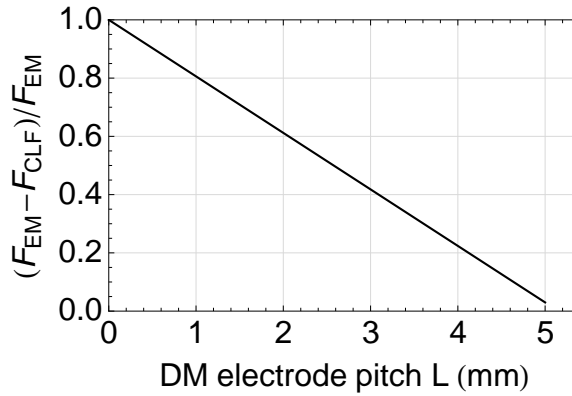


FIGURE 3.11: Fig. 3.10 is replotted to indicate the fraction of the electromechanical force available for droplet actuation.

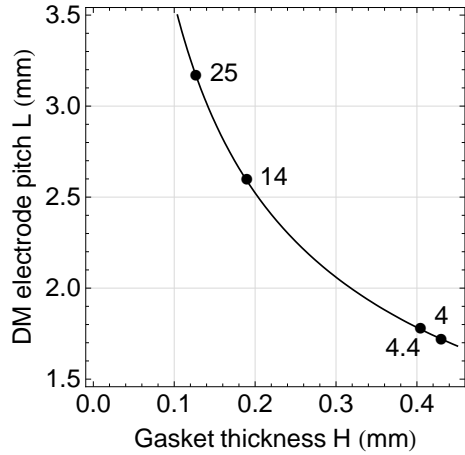


FIGURE 3.12: The line indicates the combinations of DM electrode pitch (L) and gasket thickness (H) that correspond to a unit droplet volume of $1 \mu l$. L/H is labeled.

noting that this maximum net force is attained at the expense of wasting half of the generated F_{EM} to counter F_{CLF} .

The above discussion outlines an analytical approach that uses the force balance to determine the most suitable L and H for temperature zone PCR purposes. To further refine the evaluation, additional terms can be incorporated to account for the viscous dissipation effects that exist in the droplet and in the filler medium. On the other hand, in general the droplet actuation is rarely the only factor that can affect the selection of the aspect ratio. For instance, based on the result from ray tracing simulations, the current integrated photodetector (Fig. 2.3) was designed to show the optimal S/N when fitted to a fluidic device with $L / H = 4.4$. Therefore, in order to reach a satisfactory balance between the two considerations (droplet transportation speed and photodetector S/N), it might be necessary to adopt an intermediate aspect ratio that falls between 4.4 and 14 (Fig. 3.12.)

3.3 Immiscible Phase Filtration

Nucleic acid purification is a process that isolates nucleic acids (NA) from contaminants. A typical magnetic bead-based assay involves three major steps: binding, wash, and elution. Briefly, NA in a lysate is first captured by magnetic beads. Then, the beads are washed in order to remove contaminants such as proteins, nucleases, and cellular fragments. After washing, ionic strength is lowered to release NA from the beads to an elution buffer. This way, NA is purified from a lysate and ready for subsequent analyses. In addition, sample volume is reduced from milliliters of lysate to microliters of eluent.

However, conventional magnetic bead-based purification involves repetitive pipetting and centrifugation. For example, depending on the starting sample as many as seven washes may be necessary for removing the contaminants entrapped in the bead

pellet, adsorbed on the walls of reaction tubes, or remained in the solution after aspirating the supernatant [35]. As a result, without access to costly robots the process is labor-intensive. Furthermore, due to the dominance of interfacial tension and viscosity over inertia, centrifugation is difficult to attain at microscale. Consequently, it is not straightforward to replicate the traditional assay on microfluidic devices.

Alternatively, immiscible phase filtration (IPF) is a new variant of the conventional bead-based assay. While based on the same bind-wash-elute principle, IPF does not utilize any centrifugation. Specifically, as shown in Fig. 3.13, in IPF beads bound with NA are first snapped out of the lysate to an immiscible phase. During bead snapping, the aqueous/immiscible interface represents an energy barrier that discourages the crossover of contaminants to the immiscible phase. Next, the beads are dispersed in a wash buffer. Here, the contaminants originally entrapped in the bead pellet are diluted away. Simultaneously, proteins adsorbed on the beads are denatured by chaotropic salts in the wash buffer.

After washing, the beads are transported from the wash buffer through an immiscible phase to an elution buffer. In this process, again it is energetically unfavorable for contaminants such as the chaotropic salts to enter the immiscible phase. As a result, a minimum amount of contaminants is carried by the beads to the elution buffer. Finally, the low ionic strength elution buffer promotes NA to unbind from the beads.

Following the above procedure, NA is now purified by IPF and ready for later analyses. For instance, genomic DNA has been purified from the PCR inhibitors and nucleases in lysed whole blood. qPCR is then conducted off-chip to quantify the provirus in the captured DNA. The obtained 108% amplification efficiency indicates minimal inhibitor carryover. A separate experiment in the same study claimed 90% sensitivity to plasma samples spiked with 800 copy/ml HIV-1 RNA [35]. Moreover, purification time can be reduced from 15 ~ 45 min in conventional assays to 4.1

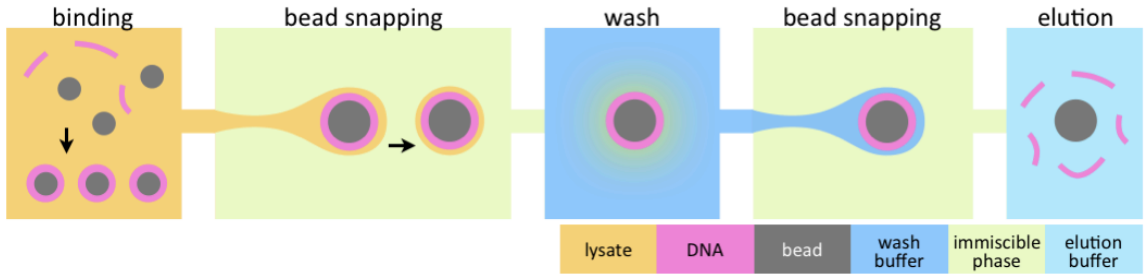


FIGURE 3.13: Schematic of an IPF device, top-down view. NA is purified from a lysate as the magnetic beads are transported rightwards through the device.

min [36]. An IPF integrated with micromachined heaters for on-chip qPCR further demonstrated a total assay time of 17 min [37].

Notably, the magnetic field that actuates the magnetic beads could be applied off-chip or generated on-chip. In previous examples the transportation of beads is controlled by permanent magnets mounted on a stepper motor or a linear actuator, whereas an IPF has utilized the magnetic field generated on-PCB by an array of multilayer coils [38].

Regarding the immiscible phase, compounds such as air [39], silicone oil [38, 40], mineral oil [37], and liquid wax [35] have been used.

Fundamentally, IPF is a series of magneto-capillary valves [39]. It requires an appropriate balance between the interfacial tension and the magnetic force acting on the beads, particularly at the lysate/miscible interface [41]. As an example, Fig. 3.14 shows the beads snapping behavior under different aqueous/miscible interfacial tension conditions. Considering the goal of reducing the carryover during bead snapping, high aqueous/miscible interfacial tension is preferred. Yet, excessive interfacial tension would exacerbate incomplete bead snapping. Beads that remain in the lysate or wash buffers are not transported to the elution buffer, resulting in the loss of NA during purification. In the extreme case, no beads would be able to penetrate the aqueous/miscible interface. On the other hand, insufficient

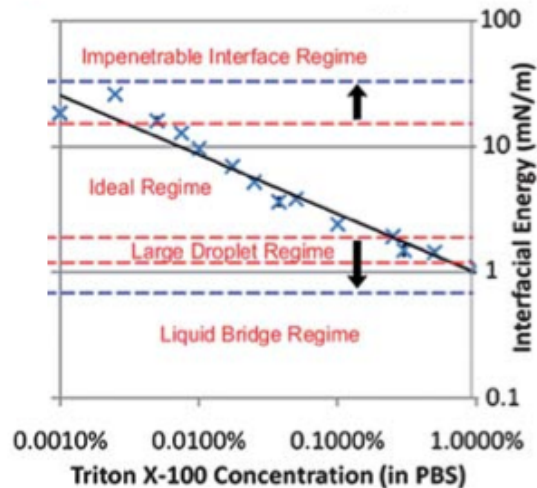


FIGURE 3.14: Bead snapping under different aqueous/immiscible interfacial tension conditions [36].

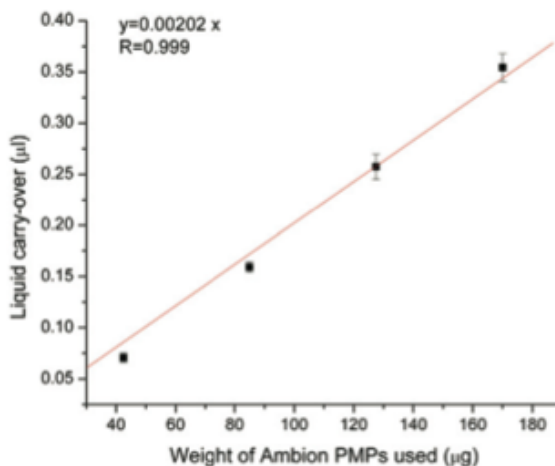


FIGURE 3.15: The linear correlation between bead weight and carryover volume [35].

interfacial tension leads to increased carryover. Accordingly, during the washes more contaminants need to be removed from the beads by digestion and dilution. In the worst scenario, bead snapping could lead to the formation of a liquid bridge, e.g., between the lysate and the wash buffer in Fig. 3.13.

In addition to interfacial tension, carryover volume is shown to be linearly proportional to bead load, i.e., total bead weight (Fig. 3.15, Appendix B.4.) In consequence,

to reduce the bead load (thus, the carryover) without sacrificing the surface area for NA binding, smaller magnetic beads are advantageous. Still, since the magnetic force acting on a magnetic bead is proportional to its volume, it is relatively difficult for smaller beads to overcome the interfacial tension and achieve bead snapping.

The above discussion suggests that optimal purification can only be obtained with suitable interfacial tensions, bead load, and magnetic field. Additional concerns include: (A) To ensure maximum NA capture, beads and lysate must be well mixed. Further attention is required in the case of a highly viscous lysate, e.g., lysed blood [36]. Similarly, adequate mixing of the beads with the wash buffer and elution buffer is crucial to contamination removal and NA unbinding, respectively. (B) Bead loss due to unsatisfactory bead snapping may be prevented by adjusting the bead transportation speed [36] and designing the IPF geometry in accordance with the applied magnetic field [39]. Besides, bead loss that originates from the adhesion to the sidewalls of the fluidic device could be mitigated by applying coating [42] and improving wash efficiency to reduce the number of wash stages. In fact, it is demonstrated that IPF is capable of purifying NA from lysed blood without any wash step [35], i.e., beads are snapped from a lysate to an immiscible phase, and then directly transported to an elution buffer [36].

In conclusion, immiscible phase nucleic acid purification utilizes the energy barrier presented by the aqueous/miscible interfacial tension during bead snapping to filter out the contaminants that would interfere with subsequent analyses (e.g., PCR inhibitors) from the captured nucleic acids. Because sample volume is reduced from milliliters of lysate to microliters of eluent, IPF could be implemented in a platform as the upstream purification/volume reduction stage to a downstream microfluidic analysis stage. This is feasible also because IPF does not employ centrifugation or demand any particular device construction. Such integration is beneficial because the manual specimen transfer from the sample preparation procedure to the bioanalytical

instruments contributes to the hands-on time and precludes full sample-to-answer automation. In contrast, with IPF sample preparation and microfluidic bioanalysis located on the same device, a hands-free operation becomes more attainable. Since the automation reduces the hands-on time and NA loss, the integration should lead to accelerated time to result and enhanced detection limit, both of which are highly desirable for rapid sparse cell quantification purposes.

Approach

After reviewing the technologies that are related to this work, this chapter will identify the advantages of combining immiscible phase filtration and digital microfluidic droplet actuation to expedite the diagnosis of bloodstream infections. The discussion also succinctly outlines the experiments that will be performed to substantiate the feasibility of the proposed IPF - DM integration. Then, a walk-through will be provided to illustrate the operation of the IPF - DM fluidic device.

4.1 Accelerate the Proven Strategy: Nucleic Acid Purification Followed by qPCR

This work seeks to use fluidic techniques to accelerate the diagnosis of sepsis. Such a fluidic device ideally should be capable of detecting multiple types of low-concentration pathogens from a large-volume raw sample, e.g., 3 CFU/ml *E. coli* in 3 ml whole blood [3]. Furthermore, the priority is to minimize sample-to-answer time and perhaps more importantly, hands-on time. This is in response to the drawbacks of current methods: blood culture takes one to three days [3], and SeptiFast requires

three hours of operator time per six-hour assay [6]. Still, it should be cautioned that performing all steps on-chip does not necessarily improve performance. Rather, the inclusion of any step onto the device for automation purposes is only sensible providing that detection limit and run time are not significantly impacted.

Traditionally, bloodstream infections are diagnosed by symptom classification systems or culturing [43]. However, new methods have been commercialized, such as biomarker detection (VIDAS BRAHMS PCT [9]) and DNA fingerprinting (SeptiFast, Prove-it [1].) Among these methods, in terms of run time and specificity, SeptiFast appears to offer a more reasonable balance than biomarker detection or culturing. Briefly, SeptiFast utilizes qPCR to detect 25 of the most common infection-causing bacterial and fungal species. Also, for some bacterial species, a follow-up qPCR can be run to detect the *mecA* gene, which indicates certain antimicrobial resistance. These qPCR-derived information are considerably more specific than what can be provided by biomarker detection, meanwhile the run time is substantially shorter than culturing. Accordingly, the “purification then qPCR” method could be even more attractive if the run time and hands-on time can be further reduced.

To accelerate a SeptiFast-like “purification then qPCR” workflow, the following might be attempted:

- Automate nucleic acid purification, and/or use a purification method that takes less step/time to execute.
- Reduce the lag between purification and qPCR.
- Automate PCR mixture preparation.
- Reduce qPCR time by minimizing the time spent on transitioning between 60 °C and 95 °C.

Whereas lab-on-chip researches usually elect to specialize on one of the listed aspects,

the first objective of this work is to identify a compatible set of fluidic technologies that can enable the pursuit of acceleration on all fronts.

As will be explained in the rest of this section, a suitable solution seems to be using immiscible phase filtration to purify the nucleic acids, followed by employing digital microfluidic droplet actuation to prepare the PCR mixture. Furthermore, a complete implementation might expand the two technologies to incorporate chemical lysis and temperature zone PCR.

Yet, with two fluidic devices, each dedicated to pre- or post-purification processes, it is still necessary to manually transfer the eluent between the two. Therefore, to fully exploit their ease of automation to attain hands-free operation, the key is to integrate IPF and DM onto a common platform. Thus, the second objective of this work is to construct such a fluidic device, and then run basic purification and qPCR tasks on the developed device to demonstrate the feasibility of IPF - DM integration.

4.2 PCR Preparation by DM Droplet Actuation

PCR mixture preparation refers to the procedure that combines purified nucleic acids, qPCR assays, and PCR master mix into a solution for the subsequent thermocycling. This step is extremely sensitive to contaminations, e.g., by PCR inhibitors, other samples, and products from previous PCR runs. Also, without a dedicated robot, it is also highly laborious and therefore prone to operator errors.

The two problems can be addressed by using DM droplet actuation to prepare the PCR mixtures. First, the routing and mixing of the reagent droplets are performed in an enclosed fluidic device, thereby eliminating the exposure to airborne contaminants. In contrast, during a conventional benchtop preparation, the solutions are exposed and thus vulnerable to the contamination until the well plate can be sealed by an optical adhesive film. Second, DM actuation is inherently automated, which

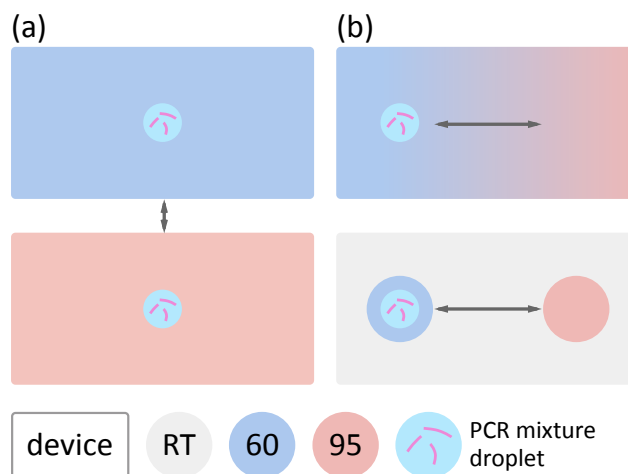


FIGURE 4.2: PCR on DM device. (a) Whole-chip thermocycling. (b) Using DM actuation, the PCR mixture droplet is shuttled between the two temperature zones or hot spots. In the latter case, the globally cooled device might allow other processes (e.g., PCR preparation, non-PCR reactions) to be concurrently executed.

4.3 Nucleic Acid Purification by Immiscible Phase Filtration

Meanwhile, since a lysate generally cannot be directly inputted to PCR due to the presence of concentrated PCR inhibitors, it is necessary to prepend the aforementioned PCR preparation stage with a nucleic acid purification stage. Then, considering that the initial evaluation will be limited to a simplified purification scenario yet without losing sight of the eventual sparse pathogen detection application, the purification stage of the fluidic device should satisfy the following requirements:

- Its construction and the employed purification method should be scalable to accept $1 \mu\text{l} \sim 100\text{s } \mu\text{l}$ of lysate. As a reference, 3 ml blood is analyzed by SeptiFast in order to deliver a statistically relevant diagnosis.
- The purification time at minimum should be comparable to typical benchtop purification protocols.
- Amenable to low-cost automation: Ideally, no operator intervention should be

needed except for sample and reagent loading.

- Crucially, in order to be compatible with the downstream DM-based PCR preparation stage, the output of the purification stage should be a static solution of concentrated nucleic acids on the order of 1 μ l and with an acceptable concentration of PCR inhibitors.

The last requirement may be interpreted from the perspective of the PCR preparation stage in two different ways. First, as DM actuation cannot efficiently manipulate liquids that are more than a few microliters in volume, it relies on the purification stage to scale down the analyte volume from milliliter to microliter. In this role, the purification stage might be thought of as the chip-to-world interface of the DM-based PCR preparation stage. Second, accompanied by the volume reduction is the enriched pathogen nucleic acid concentration. The PCR preparation stage depends on this preconcentration to improve the probability of having at least one copy of the target in an eluent droplet.

The above design constraints are derived from an earlier unsuccessful attempt to develop a purification stage that utilized size differentiation to isolate pathogens from whole blood (deterministic lateral displacement, which is a continuous flow technique [45].) Later on, the exploratory tests summarized in Appendix B suggested that immiscible phase filtration, a recent variant of magnetic bead-based nucleic acid purification, seemed to be a logical fit. In addition to satisfying the above specifications, nucleic acids processed by IPF have been reported to be sufficiently purified for benchtop PCR reactions [46, 47].

Herein, the IPF purification stage will be subjected to a relatively straightforward task of purifying the nucleic acids from a highly concentrated solution of a chaotropic salt. This uncomplicated purification scenario permits the initial development to focus on showing the feasibility of combining IPF and DM; it does not preclude a

more complex sample such as a cell lysate from being tested on the purification stage.

In particular, the reagents in a commercial bead-based purification kit will be used without modification. In contrast, typical IPF studies frequently focus on adjusting the interfacial tension between the aqueous phase and the immiscible phase in an attempt to reduce or completely eliminate the wash steps, e.g., [40]. The intention here is to evaluate how well the off-the-shelf reagents would perform in IPF-based purification. Using the reagents as-is is also expected to reduce the risk of contamination.

Finally, it is worth noting that the IPF - temperature zone qPCR integration has been demonstrated on a non-DM fluidic device [37]. Yet, two crucial flaws are unaddressed in the reported implementation. First, it would be difficult to scale up its droplet actuation mechanism to execute more than one PCR reaction at a time. Second, magnetic beads are required to remain in the droplet that is undergoing qPCR. However, the presence of microbeads in a PCR mixture has been observed to reduce the amplification efficiency by 50% [48].

In contrast, since DM actuation can simultaneously manipulate multiple droplets, the qPCR part of SeptiFast could be fully replicated on a DM device by performing six concurrent multiplex qPCR reactions (for Gram-positive and Gram-negative bacteria, fungi, positive and negative controls.) Also, since DM does not actuate a droplet via the magnetic beads, the beads can be removed from the eluent immediately after elution. This way, no significant amount of the magnetic silica beads will be present in the PCR mixture droplet, and the concern about the beads interfering with qPCR could be ruled out.

4.4 Interfacing IPF with DM

The interface between immiscible phase filtration and digital microfluidic droplet actuation is the elution buffer reservoir (Fig. 4.3, Fig. 5.4.) The EB reservoir is the last section of the purification stage (stores the elution buffer) that doubles as the first section of the PCR preparation stage (stores the eluent and then dispenses the eluent droplets.) Specifically, during elution nucleic acid-bound magnetic silica beads are transported to the EB reservoir. Then, due to the low salt condition in the reservoir, the nucleic acid is released from the beads to the EB. Afterwards, eluent droplets can be dispensed from the reservoir using DM actuation for the subsequent PCR mixture preparation.

Despite the simple concept, this interface is critical to the detection limit. Under the described implementation, the detection limit can be improved by optimizing the ratio $V_{\text{reservoir}}/V_{\text{drop}}$. In principle, by reducing $V_{\text{reservoir}}$ and increasing V_{drop} to make the ratio equal to the number of qPCR reactions to be conducted, e.g., three in the SeptiFast test, the maximum number of copies of pathogen nucleic acids could be packed into the eluent droplets for the subsequent qPCR detection. ($V_{\text{reservoir}}$, V_{drop} : volume of the EB reservoir and the eluent droplet, respectively.)

In practice, however, $V_{\text{reservoir}}$ needs to be sufficiently large to accommodate the beads and produce high elution efficiency during elution. Also, to perform temperature zone PCR, maximum V_{drop} is limited by the largest droplet volume that can be reliably transported at the desired velocity using DM actuation. On the other hand, whole-chip thermocycling would not be subjected to this limit.

As an example, assuming a 100 μl sample with 1 copy/ μl pathogen nucleic acid concentration and no purification loss, after eluting to a 10 μl elution buffer the nucleic acid is enriched to 10 copy/ μl . Still, a 5 nl droplet dispensed from the EB reservoir will contain only 0.05 copies of the pathogen nucleic acid, which cannot be

reproducibly detected by qPCR. On the other hand, by decreasing the reservoir capacity to 1 μl and increasing the droplet volume to 333 nl (i.e., reduce $V_{\text{reservoir}}/V_{\text{drop}}$), three droplets at 33 copy/droplet can be obtained (as required by SeptiFast), which is approximately three times the detection limit of a typical qPCR reaction.

Furthermore, a related complication is that with decreasing copies in a droplet the packing of nucleic acids into a droplet is increasingly influenced by a Poisson distribution [49, 50]. Hence, increasingly unfavorable detection accuracy and precision are obtained, especially because the time-sensitive nature of the application does not permit the qPCR to be repeated. Therefore, $V_{\text{reservoir}}$ and V_{drop} ideally should be sized such that even when presented with a sample that carries the lowest anticipated pathogen nucleic acid concentration, sufficient pathogen nucleic acids (e.g., > 20 copies) can still be packed into the eluent droplets.

Since this work represents the initial development of the IPF - DM fluidic device (and the assays, supporting instruments needed to operate the device), an optimal IPF - DM interface will not be the emphasis herein. (A related limitation is that, as requested by the development of the integrated photodetector, the pitch of the DM electrode has been fixed at 700 μm . That is, only $V_{\text{reservoir}}$ could be varied.) However, the data that are to be collected, such as nucleic acid retention and qPCR detection limit, would be valuable for optimizing future IPF - DM devices.

4.5 Advantages

The proposed approach is an enhancement to SeptiFast's proven method of sparse pathogen detection and paves the way for a highly automated single-chip solution to sepsis diagnosis. The key to such a fluidic device is the integration of immiscible phase filtration and digital microfluidic droplet actuation. Hence, as a first step, this work aims to demonstrate the feasibility of the integration by performing basic

purification - detection tasks on an IPF - DM fluidic device.

The fluidic device will prepare the PCR mixtures using DM actuation. Since DM is inherently automated, it minimizes the hands-on time and reduces the chance of contamination. Importantly, unlike other droplet manipulation techniques, DM is not limited to actuating of a single droplet. Accordingly, the PCR preparation stage can be scaled up to support the concurrent execution of several multiplex qPCR reactions, which is needed to cover the detection of more than two dozens of infection-causing pathogens. In addition to PCR preparation, DM actuation might also be used to perform temperature zone PCR. This technique attempts to improve the temperature ramp rate over whole-chip thermocycling to substantially trim the PCR time.

Upstream to the PCR preparation stage, IPF will be utilized to purify the nucleic acid. IPF is suitable because it can process a milliliter-sized sample and output the resulting purified nucleic acid in a way that is compatible with DM. More importantly, it transforms the conventional magnetic bead-based purification scheme into a format that is far more amenable to low-cost automation. For example, the manual purification in this work could be fully automated using two linear actuators.

In addition to the speedup brought by the automation, a well-tuned IPF reagent system could attain the necessary degree of purification in appreciably fewer steps than a typical benchtop solid phase extraction procedure, thereby considerably reduces the purification time. This claim is supported by [35], in which the nucleic acid is purified from whole blood for benchtop qPCR using only one bead snapping step and without the use of any wash buffer.

Last but not least, although this work will focus on the steps that are subsequent to the binding of the nucleic acid to the magnetic silica beads, the IPF purification stage may be expanded to incorporate on-chip binding and on-chip chemical lysis [38]. Such a fluidic device would be hands-free after mechanical lysis and reagent

loading, which addresses the long hands-on time issue of the SeptiFast test.

In short, by combining IPF and DM, a “lysis-to-answer” sparse pathogen detection fluidic device seems to be achievable. In terms of the workflow and the reagents, this approach intentionally maintains the compatibility with the sepsis diagnosis kit SeptiFast. However, via automation and the expediting of nucleic acid purification and qPCR, the hands-on time and the sample-to-answer time should be notably reduced.

4.6 General Workflow and Device Operation

To illustrate how an IPF - DM fluidic device could be implemented and operated, the following paragraphs will briefly walk through the general workflow sketched in Fig. 4.3. To facilitate the discussion, micrographs showing the bead snapping and the eluent droplet generation processes are shown in Fig. 4.4.

In particular, in Fig. 4.3 notice that the EB reservoir has two functions. First, it is the last section of the purification stage (stores the elution buffer.) Second, it is also the first section of the PCR preparation stage (stores the eluent and then generates the eluent droplets.)

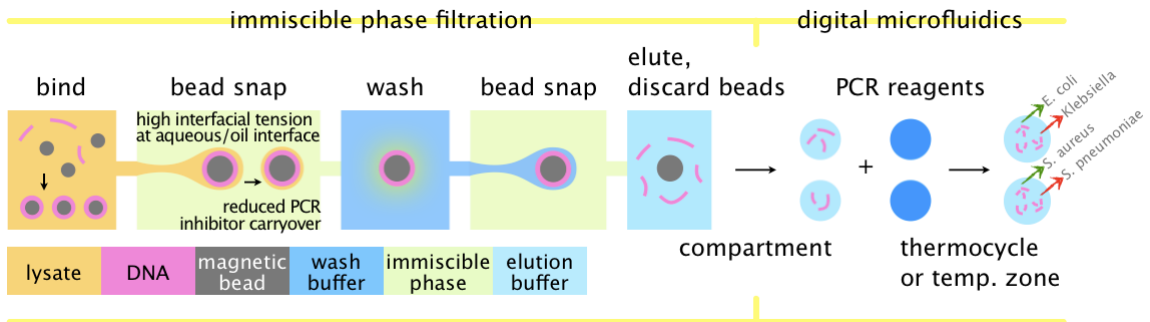


FIGURE 4.3: Operation of the IPF - DM fluidic device.

1. DNA binding, reagent loading:

As illustrated in Fig. 4.3, following a modified NucliSENS miniMAG protocol,

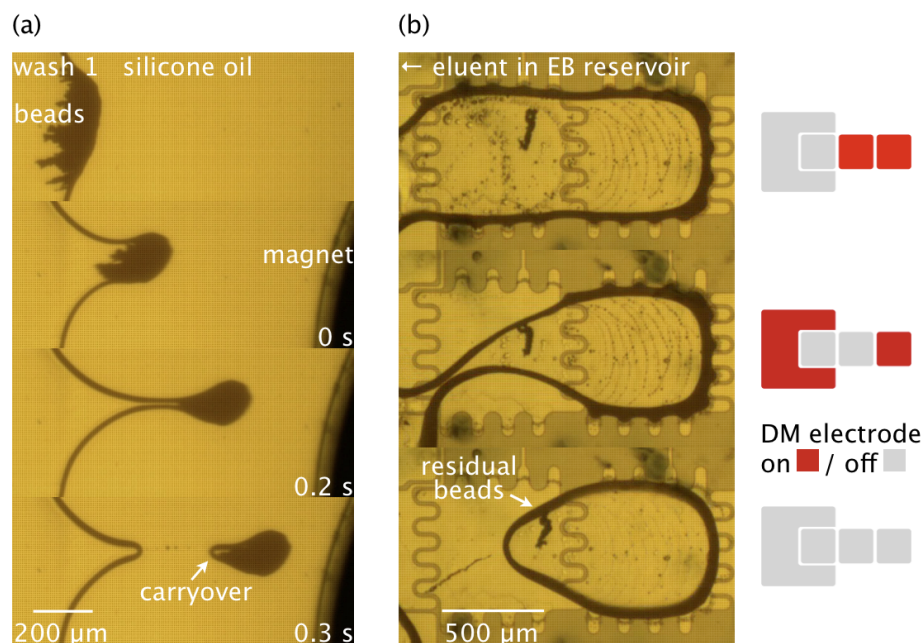


FIGURE 4.4: (a) The magnetic beads were snapped from Wash Buffer 1 to the immiscible phase. (b) An eluent droplet is dispensed from the EB reservoir with a minimum amount of the residual beads.

DNA is bound to the magnetic silica beads. Also, the purification reagents (wash buffers, elution buffer) and the qPCR reagents (master mix, qPCR assays) are loaded to the fluidic device.

2. Immiscible phase filtration, washing:

Actuated by an external magnet, the beads are snapped out of the PCR inhibitor solution to the immiscible phase. During the snapping, the bead pellet is encapsulated by the carryover (Fig. 4.4a.) Because it is energetically unfavorable for the aqueous PCR inhibitor solution to enter the immiscible phase, the volume of the carryover is limited. Later, by dispersing the beads in the wash buffers, PCR inhibitors in the carryover are digested or diluted. In the simplified case herein, the PCR inhibitor would be the GuSCN chaotropic salt that exists in the Lysis/Binding Buffer and Wash Buffer 1 of the miniMAG kit.

3. Elution:

After the IPF washes, DNA-bound beads are transported to the EB reservoir. Here, because of the low ionic strength, DNA is released from the beads to the elution buffer. After a brief incubation, the beads are transported away from the EB reservoir to prevent the beads from lowering the PCR amplification efficiency.

4. PCR mixture preparation, qPCR:

Later, after DNA is released from the beads to the elution buffer, an eluent microdrop is generated (Fig. 4.4b) and then mixed with the PCR reagents using DM actuation. Finally, the resulting PCR mixture droplets are thermocycled, and the copy number of the target can be correlated with the thermocycles needed to reach a threshold fluorescence intensity.

Based on the reported durations and the empirical evidences, estimations of the sample-to-answer time and the hands-on time are shown in Table 4.1. Assuming a fully developed fluidic device, the total run time may be reduced from SeptiFast's current 6 ~ 10 hr to 1.5 hr. More importantly, the hands-on time could be trimmed by 90% to approximately 20 min (mechanical lysis and 5 min reagent loading.)

Table 4.1: Estimated total run time and hands-on time.

Step	Benchtop	IPF+DM
	Time (hr)	
Mechanical lysis	0.25	0.25
Chemical lysis, purification	1.75 ~ 2.75	0.42 ¹
qPCR preparation	1	0.05
qPCR	1.5	0.3 ~ 0.7 ²
Melting curve	0.5	0.5
Total / hands-on	6 / 3	1.52 / 0.33

¹ Reagent loading followed by on-chip chemical lysis, purification, and elution = 5 + 10 + 5 + 5 min.

² Temperature zone PCR ~ whole-chip thermocycling.

Development of Assay, Fluidic Device and Auxiliary System

After pinning down the approach described in Chapter 4, the reactions and the necessary hardware need to be planned and developed before any on-chip validation can be conducted. An overview of this process is the focus of this chapter. Briefly, in Sec. 5.1 the selection of the detection target and the evaluation of the qPCR and purification reagents are discussed. The goal is to identify the suitable reagents to facilitate the initial testing of the fluidic device. Then, Sec. 5.2 will examine the main workhorse in the subsequent experiments, the “Gen II” fluidic device. Compared with typical DM devices, the two major differences are the inclusion of the purification stage and the ability to perform DM droplet actuation at elevated temperatures. Finally, since no commercial turn-key solutions are fully compatible with the operation of the fluidic device, a qPCR instrument needs to be custom constructed. This involves the development of three components: temperature control system, fiber optic fluorescence sensor, and device holder. Details of the in-house qPCR instrument will be provided in Sec. 5.3.

5.1 Assays

The demonstration of on-chip nucleic acid purification and quantification necessitates three types of reagents: qPCR assay, PCR master mix, and the purification kit. The purification kit purifies nucleic acids from PCR inhibitors. Then, the purified nucleic acid is mixed with the qPCR assay and the master mix. Later, the resulting mixture is thermocycled to perform qPCR. The selection of these reagents is surprisingly time-consuming. Because the requirements imposed by the integrated photodetector and the applicability to future experiments must also be contemplated. For example, the selection of the detection target needs to account for the possibility of low retention during the purification procedure. Also, to prepare for the later evaluation of on-chip lysis, the target ideally should reside in readily available and easy-to-lyse cells. As for the fluorescent tag on the probe, the fluorophore must be compatible with an affordable laser and available from the oligomer vendors. Further, the assessment of the master mix is based on the following criteria: short PCR time, high target concentration in the reaction mix, and no premixed reference dye that may interfere with the integrated photodetector. The next three sections will detail the evaluation of the three reagents, and the aforementioned considerations would be further elaborated.

5.1.1 qPCR Assay

A part of a qPCR reaction mixture is the qPCR assay. It is comprised of two primers and a fluorophore-labelled probe. Together, the three oligonucleotides define the sequence to be amplified and thus detected. This section will first discuss the selection of the fluorophore. Then, the target and its corresponding assay will be determined for use in the subsequent on-chip qPCR experiments. Finally, the assumption underlying the conversion from HeLa gDNA weight to Yb8 copy number is explained.

Dye Selection

It is possible to focus solely on the development of fluidic devices if off-the-shelf qPCR assays can be employed. Unfortunately, this option is currently infeasible, because the vast majority of ready-to-use qPCR assays are supplied with the fluorophore FAM (494/518 nm), whereas the integrated photodetector is being developed for HEX (absorption/emission peak = 535/553 nm.) This choice is primarily attributed to the preference of using the low-cost 532 nm laser diode as the excitation source.

In addition, the selection of the fluorophore on the qPCR probe is also influenced by the following factors:

- SecureSeal (Grace Bio-Labs), an alternative gasket material to SU-8, is incompatible with red fluorophores such as Cy5 (643/667 nm.)
- The fluorophores designed to be excited with UV light generally have a much larger Stokes shift than the aforementioned fluorophores, e.g., Alexa Fluor 350 (346/442 nm.) The large Stokes shift substantially reduces the difficulty of suppressing the pump before it reaches the integrated photodetector (Fig. 2.3.) Still, UV excitation might interfere with PCR. According to [51], PCR performed with UV-irradiated primers and *Taq* polymerase is observed to reduce the detection limit by one order of magnitude.
- The availability of a compatible 3' quencher.
- While the integrated photodetector is being developed, on-chip qPCR is conducted using the fluorescence sensor discussed in Sec. 5.3.3. Thus, a suitable filter set (i.e., excitation filter, dichroic beamsplitter, and emission filter) needs to be available.
- The ideal dye should feature high molar extinction coefficient, quantum yield, and photostability. In these regards, newer dyes such as ATTO 532 are superior

to HEX, as can be seen in Table 5.1. Still, although ATTO 532 is used in Sec. 5.3.3 to characterize the in-house fluorescence sensor, due to cost reasons it is not used on the qPCR probe.

Table 5.1: Comparison of two $\lambda_{abs} \sim 532$ nm fluorophores.

Dye	ε_{max} ($M^{-1}cm^{-1}$)	Φ
HEX	9.6×10^4	0.7
ATTO	1.2×10^5	0.9

Target Selection

Since off-the-shelf qPCR assays are typically only available with FAM, in order to replace FAM with HEX it is necessary to involve custom qPCR assays. To minimize the time spent on developing the custom assays, a literature survey was conducted to locate the assays that are appropriate for this work, and then the probes in the identified assays were modified with HEX and its corresponding 3' quencher.

Notably, during the survey the unavailability of FAM indirectly led to an additional complication. MGB probe, a variant of the TaqMan probe, is frequently employed in recent publications. However, MGB probe is only available from Life Technologies with FAM as the 5' fluorophore. As a result, MGB probes and the sequences developed for MGB probes could not be used in this research without modifications.

At present, two assays designed to detect multicopy/genome targets are identified to be useful for later experiments: (1) Alu Yb8 detects a 1852 copy/genome human-specific 176 bp sequence [52, 53]. (2) EC23S857 detects a 6 copy/genome *E. coli*-specific 88 bp target [23]. As a comparison, the two targets are located within the 3.2×10^9 bp human genome and the 4.6×10^6 bp *E. coli* K-12 genome, respectively.

Table 5.2 shows the relevant properties of the Alu Yb8 assay. The probe has a 5' HEX fluorophore, an internal ZEN quencher, and a 3' Iowa Black quencher. In a

typical 20 μ l reaction that uses the Fast Advanced master mix, the final concentrations of the primers and the probe are 1 and 0.25 μ M, respectively. The primer/probe ratio of 4 is based on [53].

Table 5.2: Alu Yb8 assay.

Type	nmole	GC (%)	MP ($^{\circ}$ C)	Size (bp)	Sequence 5' \rightarrow 3'
Primer 1	10	65	59	17	AGTGGCGCAATCTCGGC
Primer 2	10	55	58	22	GTCAGGAGATCGAGACC ATCCT
Probe	2.5	64	67	25	HEX/AGCTACTCG/ZEN/ GGAGGCTGAGGCAGGA/ IBFQ

Alu Yb8 and EC23S857 were chosen for two reasons. First, multicopy/genome targets are preferable because the detection limit is proportionally improved. Second, it seems logical to initiate the development of the fluid device based on an “easy” target that exists in readily available cells. (HeLa can be obtained from the Duke Cell Culture Facility.) Subsequently, once the fluidic device is sufficiently developed, tests can be conducted using a “difficult” but more relevant target. To clarify, an “easy” target should have a high copy/genome ratio and exist in easy-to-lyse cells.

On the other hand, despite their significantly larger copy/cell ratio, targets in mitochondrial DNA are thought to be unsuitable. Unlike the aforementioned targets that feature a fixed copy/genome ratio, targets located in mtDNA have highly variable copy numbers [54, 55]. As a result, the characterization of the detection limit could be interfered.

Still, a drawback of using Alu Yb8 to model a pathogen DNA target is that background contamination would be challenging to eradicate or mitigate. Since human cells are omnipresent and Yb8 has a high copy/genome ratio, any contamination that exists in the reagents or introduced by the manual procedures such as the reaction mixture preparation inevitably results in a relatively high background. This issue is

evident in the No Template Control in Fig. 5.1 (red trace.) Further, as mentioned on p. 18, in the case of EC23S857 the evaluation of the detection limit might be impeded by the bacterial DNA contamination in the DNA polymerase.

Yb8 Assay Validation

After the Yb8 assay was selected and synthesized (by Integrated DNA Technologies, Inc.), qPCR is performed to validate the design and the synthesis. Specifically, the assay is employed to quantify the Yb8 in the nucleic acids extracted from HeLa cells using the miniMAG purification kit. The Fast Advanced master mix is used to prepare the reaction mixtures, and the amplification is run on the ABI 7900HT benchtop qPCR instrument.

The obtained results are shown in Table 5.3 and Fig. 5.1. Briefly, the calibration curve derived from the two standards (#1, 2) is utilized to estimate the amount of Yb8 in the unknown (#3.) Also, #4 is the negative control. In the table, the expected copy numbers are estimated from the input HeLa gDNA weight (#1, 2, 4) or PicoGreen dsDNA measurement of the eluent (#3.)

Importantly, the successful amplification suggests that the assay is correctly designed and synthesized. Further, from the aforementioned calibration curve the amplification efficiency can be calculated to be 81%. Lastly, although the FAM-labelled probe is used in this evaluation in order to maintain the compatibility with 7900HT, the HEX-labelled probe is used in all on-chip qPCR tests in Sec. 6.2.

Table 5.3: qPCR detection of Alu Yb8. Also see Fig. 5.1.

#	C_t	Measured/expected (copy)	Sample
1	12.9	$-/1.3 \times 10^7$	Genomic DNA
2	16.6	$-/1.5 \times 10^6$	Genomic DNA
3	18.3	$5.3 \times 10^5 / 3.3 \times 10^5$	NA extracted from cells
4	33.9	$5.0 \times 10^1 / 0.0 \times 10^0$	No Template Control

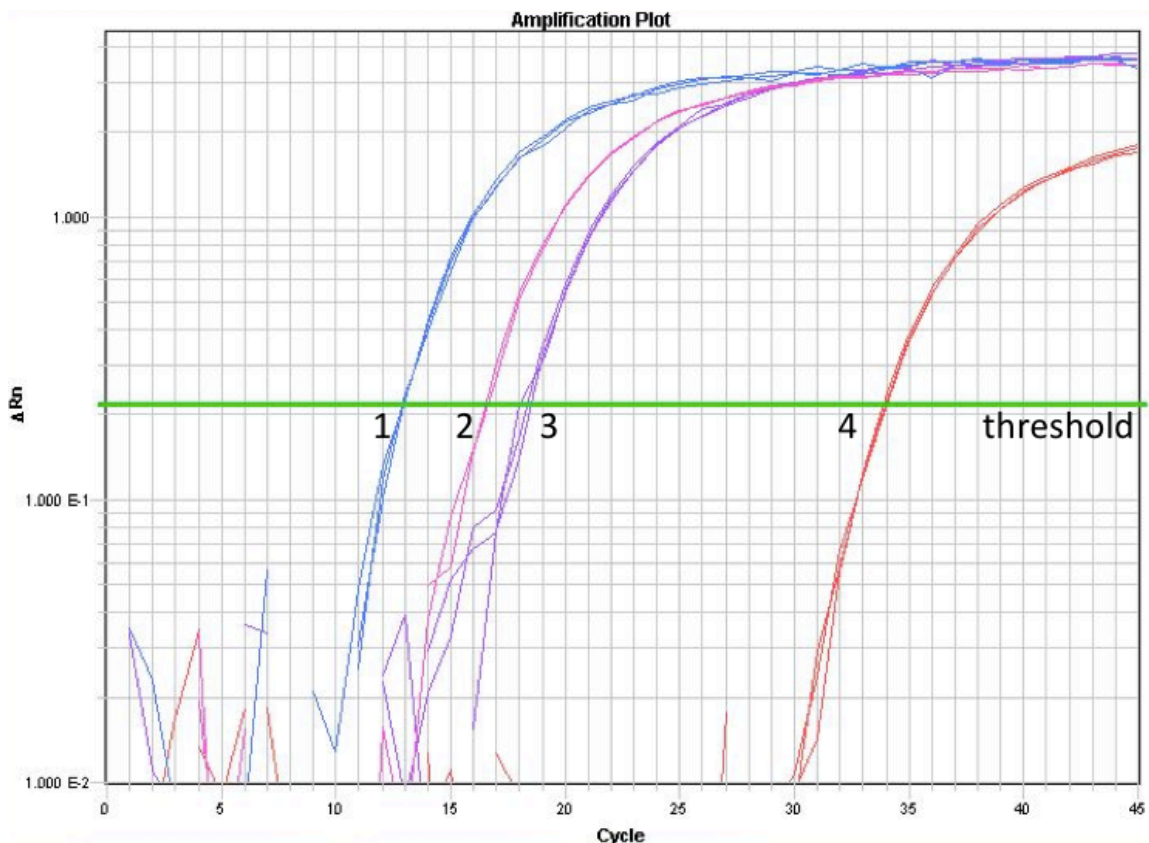


FIGURE 5.1: Amplification of a 176 bp segment in Alu Yb8. Also see Table 5.3.

Yb8 Copy Number in HeLa

The Alu Yb8 target was chosen because of the high copy/genome ratio, DNA and cell availability, and the ease of lysing human cells. These attributes should facilitate the initial development of on-chip lysing, purification, and qPCR.

However, rather than human somatic cells, the current source of Yb8 is HeLa gDNA. (The exception being the experiment shown in Fig. 5.1, which involves HeLa cells.) It is thought that the use of HeLa might better ensure the consistency between the current gDNA-based experiments and the future cell-based experiments, e.g., the evaluation of on-chip lysing. This is because HeLa can be affordably obtained from the Duke Cell Culture Facility. Furthermore, the concentration provided is sufficiently high (3×10^5 cell/ml as counted by a hemocytometer) such that it can

be directly used in on-chip lysing tests, i.e., the cells do not need to be cultured to higher densities.

Still, the copy number of the Yb8 target in HeLa is not known to be determined. This is likely because the sequencing of HeLa was only recently completed in March 2013, and the sequence still is not publicly accessible [56]. Consequently, when converting from HeLa gDNA weight to Yb8 copy number, the same 3 pg/genome and 1852 copy/genome, as in the case of human somatic cells, are assumed. Hence, qPCR results that involve the conversion of HeLa gDNA weight to Yb8 copy number should be interpreted with the aforementioned assumptions in mind.

To summarize, the dye on the probe is selected to be HEX, because its absorption peak is nearly coincident with the 532 nm output of low-cost laser diodes. Also, it is one of the stock dyes available from the major oligomer vendors.

Furthermore, the Alu Yb8 assay, which detects a 176 bp sequence that is specific to the human genome, will be employed to perform on-chip qPCR. Its high copy/genome ratio should facilitate the initial developments, particularly in the characterization of nucleic acid retention.

Lastly, the current source of Yb8 is HeLa gDNA. The decision to use HeLa gDNA is essentially to make provision for future on-chip lysing experiments, since HeLa cells are affordably available on-site.

However, the Yb8 copy number in HeLa is not known to be determined. As a consequence, in the conversion from HeLa gDNA weight to Yb8 copy number HeLa gDNA is assumed to be equivalent to human somatic cell gDNA. Thus, it is important to analyze the subsequent qPCR-derived results with this assumption in mind.

5.1.2 PCR Master Mix

A master mix is composed of the DNA polymerase, dNTPs, and other reagents that support the function of the polymerase. While any master mix can be used to

demonstrate the integration of IPF nucleic acid purification and DM reaction mixture preparation, the comparison of master mixes in this section nonetheless shows that an appropriate choice can expedite the execution of experiments.

To facilitate the subsequent evaluation of the two master mixes, the differences between them are summarized in Table 5.4 and Table 5.5. In the calculation of the maximum sample volume in Table 5.4, a reaction mixture is assumed to contain two qPCR assays in order to perform a duplex detection: the target of interest and an exogenous internal positive control. Pre-thermocycling steps include UNG incubation and polymerase activation. Dwell time refers to the total duration spent at 60 °C and 95 °C. Pre-thermocycling time and dwell time are calculated from the default protocols listed in Table 5.5. The run time is measured on the ABI 7900HT benchtop qPCR instrument.

Table 5.4: Comparison of master mixes.

	QuantiFast	Fast Advanced
Max sample volume (µl)	12 (48%)	6 (30%)
Reaction volume (µl)	25	20
Pre-thermocycling steps (min)	5	2.3
Dwell (min)	34	16
Ramping (min)	31	37
Total run time, 45 cycles (min)	70	55
ROX reference dye	Optional	Premixed

Table 5.5: Default thermocycling profile of master mixes.

T (°C)	QuantiFast		Step
	Time (s)	Fast Advanced	
50		120	UNG incubation
95	300	20	Polymerase activation
95	15	1	Denature
60	30	20	Anneal/extend, fluorescence measurement

QuantiFast qPCR Kit

QuantiFast (Qiagen) is a qPCR kit specifically designed for pathogen detection applications [57]. Since its master mix occupies a smaller percentage of the volume of the reaction mixture (20%, versus 50% in the other master mix), a larger sample volume can be used (12 μ l versus 6 μ l, see Table 5.4.) Accordingly, at a given pathogen concentration more copies would present in the reaction mixture, resulting in an improved detection limit.

In addition to the master mix, the kit also includes a 160 bp synthetic DNA and its corresponding qPCR assay. As a whole, the synthetic DNA and its qPCR assay are intended to function as the exogenous internal positive control. By adding the control DNA to a sample, both purification and amplification can be monitored. In comparison with detecting Alu Yb8 in HeLa gDNA, this assay offers two advantages in the context of characterizing the performance of a qPCR system. First, the quantity of the synthetic DNA in a reaction mix prepared according to the default protocol is known to be 10^3 copies. Second, in a measurement of the synthetic DNA, the contamination of the reagents and the PCR apparatus by human DNA will not be detected as the background.

Because its master mix is tuned to enhance the detection limit, and the bundled internal control assay can be repurposed to perform a variety of tests, the QuantiFast kit was originally selected to run the qPCR experiments. The results that are gathered using the kit include: the initial hands-on experience with qPCR (Fig. 3.2), the sensitivity of qPCR to the inhibitor GuSCN (Fig. 6.1), and the retention of nucleic acids (Table 6.4.)

However, during the course of the above investigations, it was found that the ROX reference dye, as shipped by the vendor, seems to be consistently below the specified concentration or partially photobleached. To address this issue, it was

recommended by the Duke DNA Microarray Core Facility to switch to qPCR kits supplied by the same vendor as the 7900HT instrument, Applied Biosciences/Life Technologies. Consequently, no further tests were conducted using the QuantiFast kit.

An additional concern that indirectly contributed to the switch is related to the fluorophore on the probe. Although the characterization of the fluidic device and the workflow might rely solely on the internal control assay and the master mix in QuantiFast, the development of the integrated photodetector demands the flexibility to change the fluorophore if needed. Since the internal control assay is incapable of meeting this request, one of the factors that led to the use of the QuantiFast kit ceased to exist.

Fast Advanced Master Mix

To address the problem regarding the ROX concentration in QuantiFast, it was recommended by the Duke DNA Microarray Core Facility to change to an ABI-supplied master mix with premixed ROX. Afterwards, a suitable choice was found to be the Fast Advanced master mix [19]. Because of the two features that will be discussed in the following paragraphs, it is uniquely attractive to the development of the fluidic device. Hence, this master mix is employed in conjunction with the Alu Yb8 assay and HeLa gDNA to perform the majority of the experiments in this work.

Specifically, the first feature that makes this master mix desirable is its ability to suppress the cross contamination between PCR experiments. This is achieved by using the enzyme UNG to degrade the dUTP-incorporated amplicons. As can be seen in Table 5.5, the first step in the thermocycling profile is UNG incubation. During this step, the dUTP-incorporated amplicons generated by previous amplifications are degraded into unamplifiable fragments. On the other hand, the DNA template intended to be amplified in the current PCR is unaffected, since it does not contain

dUTP. Subsequently, UNG is deactivated during the 95 °C polymerase activation step. Because the replicates of a test are run back-to-back in order to preserve the quality of the time- and temperature-sensitive reagents, this feature is necessary to prevent the cross contamination between the replicates.

The second advantage of this master mix is the shortened PCR time. As shown in Table 5.5, other than the extra UNG incubation time, the durations specified for the steps are shorter than what are needed for the QuantiFast master mix. For example, polymerase activation takes 300 s in QuantiFast, but only 20 s in Fast Advanced. Over the course of 45 cycles, the differences amount to a reaction that is faster by 15 min, or 21%. The shortened PCR time mitigates the structural deterioration of the fluidic device caused by thermocycling. This is particularly important because the cast acrylic top plate and the SecureSeal gasket used in the fluidic device are not rated for sustained exposure to 95 °C.

However, the Fast Advanced master mix is not without issues. First, the master mix as supplied is premixed with the reference dye ROX. Later on, if ROX is found to interfere with the integrated photodetector, it would be necessary to revert to the QuantiFast master mix.

Second, test results indicate that both 7900HT and the custom-developed temperature control system are incapable of fully exploiting the potential time saving offered by the master mix. In the case of 7900HT, the 95 °C 1 s/60 °C 20 s thermocycle is observed to result in considerable ringing around the two temperature setpoints. In contrast, the 15 s/30 s thermocycle of QuantiFast produces no notable oscillations. Consequently, as can be seen in Table 5.4, the Fast Advanced master mix wastes more time than QuantiFast on ramping and settling to a temperature setpoint: 6 min/19%. This behavior suggests that the temperature control system in older qPCR systems such as the 7900HT cannot keep up with the aggressive thermocycling profile of the Fast Advanced master mix.

On the other hand, in the case of the custom-developed temperature control system, conservative temperature ramp rates have to be adopted in order to reduce the temperature difference between what is experienced by the PCR mixture droplet and what is sensed by the thermocouple. This issue will be further discussed in Sec. 5.3.1.

In summary, two master mixes have been evaluated. Each option is found to offer different advantages.

First, when normalized to the volume of the reaction mixture, QuantiFast accepts 18% more sample volume than Fast Advanced. Thus, QuantiFast should have a better detection limit to sparse pathogens. Second, the reference dye is not premixed into the QuantiFast master mix. Therefore, the characterization of the integrated photodetector might be done with or without the reference dye in the reaction mixture.

In the case of the Fast Advanced master mix, the UNG/dUTP mechanism greatly reduces the chance of cross contamination. Further, assuming that the temperature can be optimally regulated, the shorter thermocycle of this master mix can lead to substantially faster PCR. In turn, the structural integrity of the fluidic device could be better preserved.

Although most experiments herein were conducted using Fast Advanced, in practice both 7900HT and the custom-developed temperature control system are unable to fully adhere to the specified dwell time. Thus, PCR time is not trimmed by the anticipated extent. Consequently, the main differences between QuantiFast and Fast Advanced essentially boil down to the flexibility on the reference dye and the ability to prevent cross contamination.

5.1.3 Purification Assay

Two topics will be discussed in this section. First, the reasons behind the selection of the miniMAG assay are explained. Second, a summary of the on-chip purification procedure is provided, with an emphasis on outlining the adaptations made to the default protocol.

Assay Selection

The purification assay is the ensemble of reagents used to perform cell lysis and the subsequent purification of nucleic acids from the lysate. Here, the employed purification assay is bioMérieux’s NucliSens line of Lysis Buffer and Magnetic Extraction Reagents. Together, they are referred herein as the miniMAG assay.

After comparing six bead-based purification kits, miniMAG was selected because it is designed to lyse and purify by the chaotrope GuSCN and the surfactant Triton X-100, but without the help of Proteinase K [58]. In contrast to the kits that mandate Proteinase K treatment at 56 °C, miniMAG makes it possible to initiate the testing of on-chip lysis without the need to add an extra heater. (Although Proteinase K treatment and other steps such as selective lysing are likely to be needed to optimize the quality and quantity of the extracted nucleic acids [59, 60].)

Furthermore, it is worth noting that miniMAG, as well as Roche’s SeptiFast, employs silica beads. Since the binding to silica is nonselective, its adoption by SeptiFast perhaps implies that the intention is to maximize the collection of nucleic acids. Then, the identification of pathogen DNA relies on the selectivity provided by the qPCR assays and the follow-up verification by melting curve analysis. In addition to SeptiFast, this “selectivity-last” approach is also employed by the newer sepsis *in vitro* diagnostic kits such as Prove-it and Verigene (Mobidiag and Nanosphere, respectively.) Hence, selective binding in a lysate, either DNA- or sequence-specific, appears to be less preferable.

A drawback of miniMAG is that the vendor refused to disclose any information regarding the magnetic silica beads, e.g., diameter and concentration. Still, because the standard protocol uses 50 μl bead slurry to process 200 μl whole blood, the binding capacity might be estimated at 264 ng nucleic acid/ μl bead slurry. The value is in line with $10^{2\sim 3}$ ng/ μl specified by other bead-based kits (MO BIO UltraClean 15, Bioclone BcMag Quick DNA, and AMS MagSi-DNA.) Accordingly, the highest concentration used in the experiments, 1.2 ng/ μl , is assumed to be within the capacity.

Summarized Procedure of On-Chip Purification

The procedure outlined below is used in the nucleic acid retention experiment in Sec. 6.2.2. After walking through the procedure, its major differences to the vendor-supplied default protocol are itemized and briefly discussed. (The experiment-specific purification procedures are detailed in Appendix A.)

In the first step, HeLa gDNA is bound to the magnetic silica beads. This is performed according to the default protocol. Initially, gDNA and then the beads are added to the Lysis/Binding Buffer. After incubating and centrifuging, the LB Buffer supernatant is aspirated. The DNA-bound beads are then resuspended with WB1, i.e., 5 M GuSCN.

The second step loads the reagents to the fluidic device. Similar to what is shown in Fig. 5.5, prior to an experiment DNA-bead/WB1 and WB3 (two locations) are loaded to the purification stage, and EB is filled to its reservoir in the PCR preparation stage.

The third step involves the IPF washes. To perform the first wash, the DNA-bound beads in WB1 are actuated by an external magnet to WB3. Then, the beads are repeatedly dispersed and pelletized in WB3. The first wash is concluded by actuating the beads away from the WB3. Later, the beads are transported to the second WB3 to conduct the second IPF wash.

The last step is elution. After the two washes, the beads are transferred from the second WB3 in the purification stage to the EB reservoir in the PCR preparation stage. To release the DNA from the beads to EB, the beads are incubated with EB at room temperature.

The primary differences between the default protocol and the above procedure are:

- WB1 is designed to digest the proteins that are attached to the beads. However, the main function of WB1 in this work is to serve as the source of the model PCR inhibitor, GuSCN.
- WB2 in miniMAG is unused. Initially, this is because the sodium azide in WB2 interferes with the determination of GuSCN concentration by absorption spectroscopy (see p. 112.) Afterwards, WB2 is still avoided even for the experiments that do not involve measuring the absorbance. This ensures that the purification power derived from the absorbance measurement and on-chip qPCR can be cross-compared.
- Following the discussion in the previous bullet point, when two washes are needed WB2 is replaced by WB3. As can be inferred from the miniMAG manual, WB3 and EB seem to have a similar chemical composition. Thus, two washes in the low ionic strength WB3, rather than one in the default protocol, is likely to affect the retention of nucleic acids.
- The volume of the reagents is rescaled to be suitable for on-chip operations. For example, 2 μ l EB is used because it is the typical capacity of the reservoirs in digital microfluidic devices. In turn, since the volume of EB needs to be sufficiently large to accommodate the beads without having the dispensing of eluent droplets impeded, a suitable bead/WB1 volume is empirically deter-

mined to be 4 μl . In addition, 8 μl WB3 approaches the maximum volume that can be reliably placed on the device without risking an accidental coalescence of the reagents. The combination of the aforementioned volumes was tested in the experiment in Sec. 6.1.2 before it is used to design the Gen II fluidic device.

- To promote the release of nucleic acids to a small volume of EB, it is generally recommended to perform elution at 60 °C with mild agitation. However, on-chip elution is run at room temperature. This circumvents the problem of excessive EB evaporation due to the exposed reservoir (i.e., not sealed by the top plate) but sacrifices the elution efficiency.

In conclusion, miniMAG is employed as the purification assay because it provides the possibility to try basic on-chip lysis without the need of a heater. Still, the lack of information regarding the magnetic silica beads makes certain calculations and optimizations difficult to perform.

Lastly, it is worth pointing out that even though the optimization of interfacial tension is crucial for the improvement of purification power, the modification of miniMAG reagents is intentionally avoided. First, it is interesting to observe how well the reagents in an off-the-shelf purification kit can be repurposed to perform IPF washes. Second, the use of fresh, unmodified reagents minimizes the contamination of nucleic acids.

5.2 Fluidic Device

In addition to identifying the suitable purification and qPCR reagents, the goal of demonstrating a single-chip solution that combines nucleic acid purification and detection eventually calls for new fabrication techniques to be developed and new features to be added to the fluidic device. In essence, the application demands the fluidic device to be single-use and capable of withstanding 95 °C over 1 hr without

losing the ability to perform DM actuation. Still, although options are known to be commercially available, it is important to understand that in this case the two requirements can only be tackled with the materials and the instruments that are realistically accessible. Regarding the first requirement, the increased device consumption is countered by the substantially improved fabrication throughput. This is achieved by reducing the footprint of the purification stage to improve the device/wafer ratio. Also, the time-consuming fabrication steps, such as SU-8 photolithography and top plate CNC milling, are replaced with laser patterning. As for the second requirement, it is temporarily addressed by adding a conductive polymer coating to the top plate. In the next three sections, the aforementioned enhancements over typical DM devices will be examined.

5.2.1 Layout and Structure

The layout and structure of two fluidic devices will be presented in this section. As a starting point, the Generation I device was found to suffer from a few drawbacks. Later on, the identified issues were addressed by the Generation II device.

Generation I Fluidic Device

The first iteration of the fluidic device is shown in Fig. 5.2 and 5.3. The design is similar to typical DM devices in a sense that all reagents, including the wash buffers, are enclosed in the device by the gasket and the two parallel plates. Structure-wise, it is similar to what is illustrated in Fig. 5.6, except for the lack of the PEDOT:PSS layer at the top plate.

The purpose of the Gen I device was to investigate which designs need to be improved in order to reliably complete the workflow from reagent loading to thermocycling. Also, it is required to verify the ability to use DM actuation to manipulate the droplets during and after the thermocycling.

In particular, as can be seen in Fig. 5.7, it was found that baking a Gen I device, even at temperatures lower than 60 °C, would crack the ITO on the top plate. After cracking, the ITO loses the necessary conductivity to function as the ground of the DM actuation voltage. By implication, DM actuation would no longer be possible after starting the PCR. This issue will be further discussed in Sec. 5.2.2.

Furthermore, the other significant drawback regarding the Gen I design is its footprint. Since the relevant instruments in the SMIF cleanroom can only process 1 ~ 2 4-inch wafers per run, then at 6 devices/wafer the overall fabrication throughput is somewhat insufficient relative to the rate that these single-use devices can be consumed by the experiments. Yet, especially because of the multifaceted nature of this research, the fabrication time must be minimized. Hence, it was the concern about the inadequate fabrication throughput that eventually prompted the switch to the Gen II design.

Generation II Fluidic Device

As shown in Fig. 5.4 ~ 5.6, the Gen II device is designed based on the evaluation of manufacturability and usability of the Gen I design. It is this device that is used in the majority of the experiments discussed in Sec. 6.2. The Gen II device features three major improvements over the Gen I device: reduced footprint, heat-resistant top plate, and an on-chip resistive heater. The latter two features will be detailed in Sec. 5.2.2 and 5.2.3, respectively. Here, the discussion will be focused on the footprint, layout, and fabrication throughput.

As mentioned previously, the move away from the Gen I design is primarily due to the concern about the large footprint and the corresponding low fabrication throughput. Later on, it was realized that the footprint can be effectively trimmed by modifying the purification stage. Specifically, since the top plate is needed by DM but not by IPF, the top plate at the purification stage is not essential. By

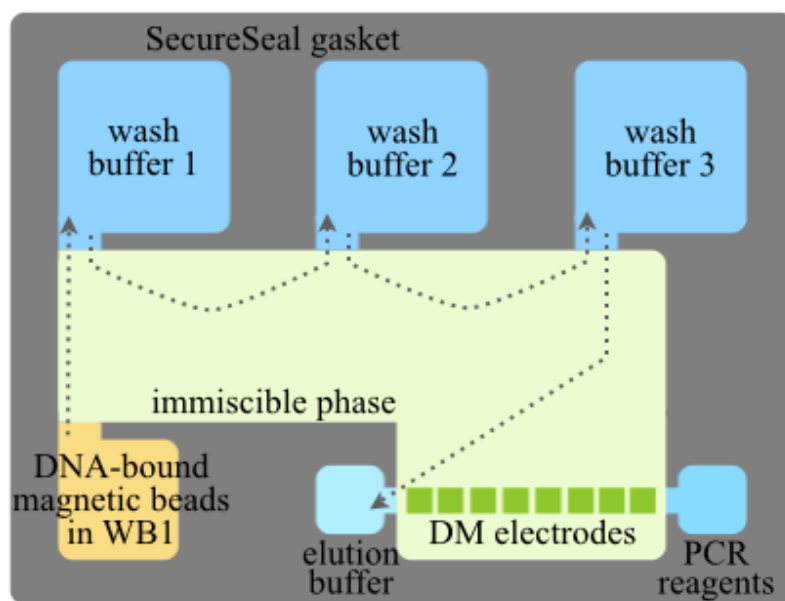


FIGURE 5.2: A sketch showing the layout of Generation I fluidic device. Dotted line: The transportation of beads during the purification process.

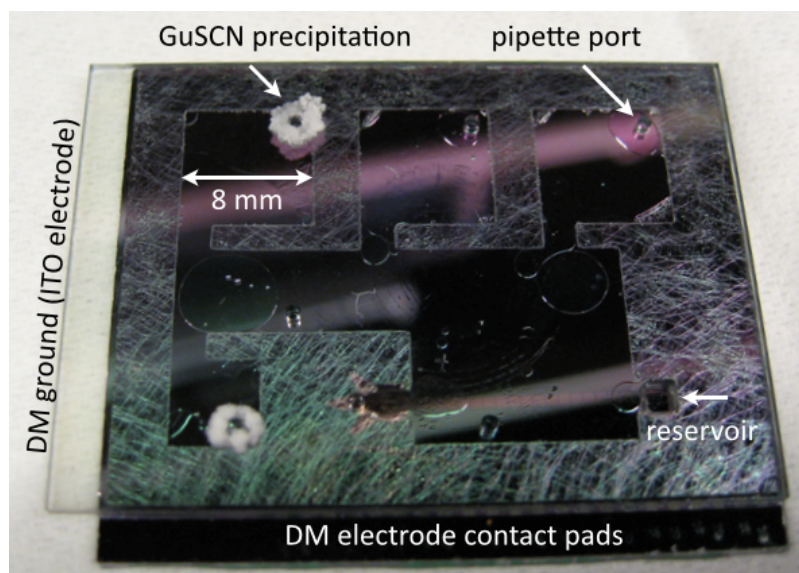


FIGURE 5.3: Generation I fluidic device. The white particle around the two pipette ports is the precipitation of GuSCN from WB1.

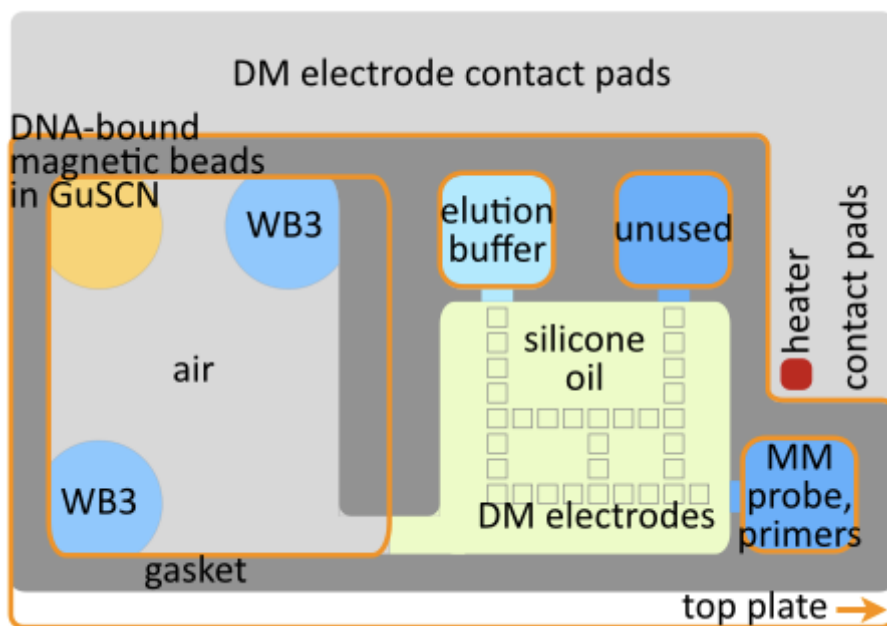


FIGURE 5.4: A sketch showing the layout of Generation II fluidic device. It also illustrates how the device could be configured to perform the nucleic acid retention experiment in Sec. 6.2.2.

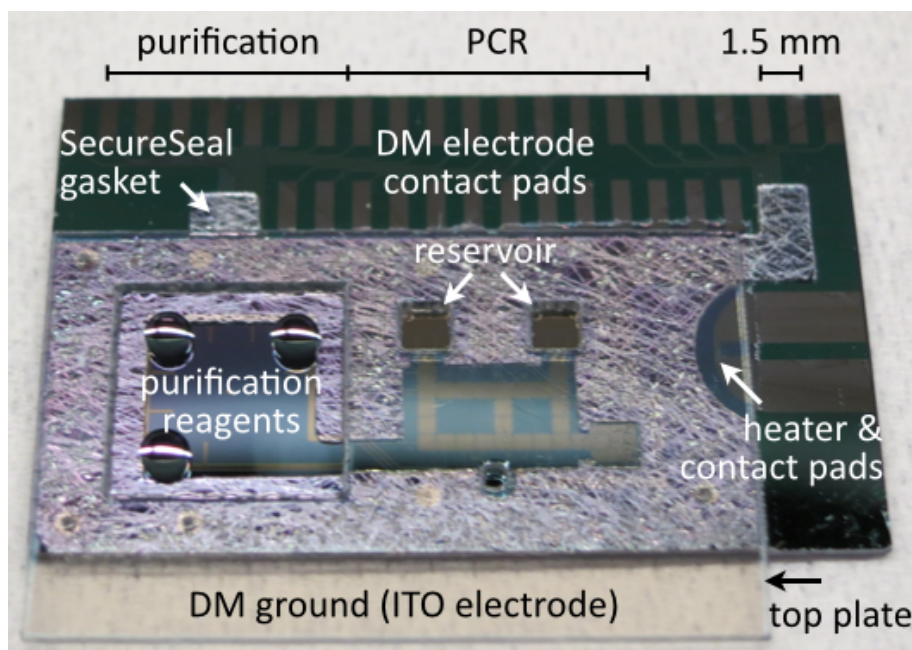


FIGURE 5.5: Generation II fluidic device.

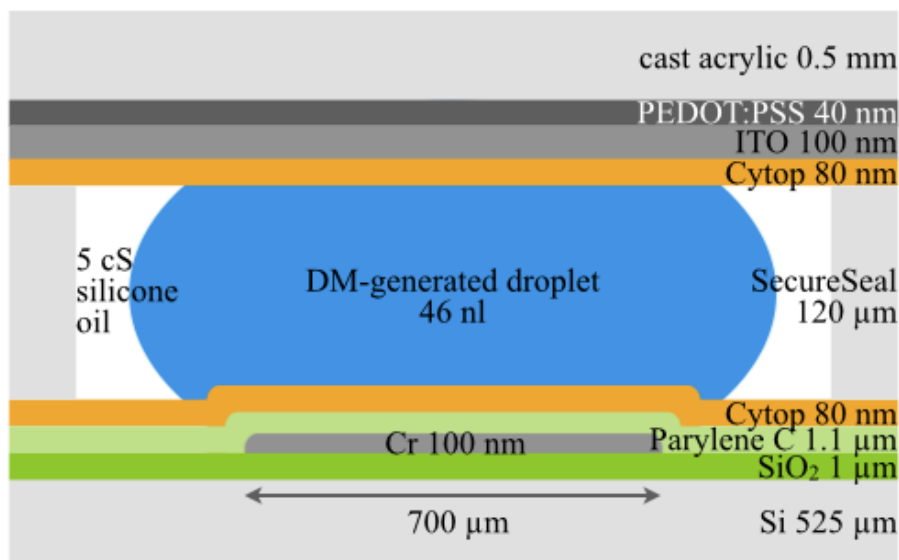


FIGURE 5.6: Structure of Generation II fluidic device.

removing the portion of the top plate that originally covered the purification stage, the wash buffers are no longer confined by the 120 μm gasket thickness (compare Fig. 5.3 with Fig. 5.5.) This way, the same volume of a wash buffer can now be accommodated in a much smaller area, and the footprint occupied by the purification stage is considerably reduced.

As part of the redesign, the number of IPF washes needed to purify the nucleic acids from the PCR inhibitor 5 M GuSCN has been estimated to be one (refer to Sec. 6.1.) Thus, as illustrated in Fig. 5.4, the purification stage of the Gen II device is designed to be capable of holding three reagents: DNA-bead/WB1 and two WB3.

Moreover, the layout rearrangement resulting from the revising of the purification stage permits the incorporation of an extra reservoir and an on-chip resistive heater without penalizing the device area. The two additions enable more sophisticated tests to be conducted. In particular, the heater and the DM electrodes are located at the same 100 nm Cr layer in Fig. 5.6. Since the heater is patterned in the same lift-off step as the DM electrodes, the inclusion of the heater does not require any

extra fabrication step.

Still, improving the fabrication throughput of the bottom plate is inconsequential if the throughput of the top plate is not correspondingly raised. To this end, as part of the development of the Gen II device, the patterning of the cast acrylic top plate is changed from CNC milling to laser cutting. This change of manufacturing method markedly reduces the fabrication time of the top plate. Whereas CNC milling approximately produces 6 top plates per 2 hr run, laser cutting is capable of at least 60 plates per 1 hr run. Although the rate of top plate fabrication is largely limited by the capacity of the ITO sputtering instrument, laser cutting nonetheless brings a significant time saving.

Overall, the number of devices that can be fabricated on a 4-inch silicon wafer is increased from 6 to 11. The much-improved fabrication throughput is crucial because the experiments do not permit the devices to be reused. On the down side, since the Gen II device is not fully sealed, the chance of contaminating the reagents is increased. This issue will be further explored in Sec. 6.3.2.

5.2.2 Heat-Resistant Plastic Top Plate

As can be seen in Fig. 5.7, baking at moderate temperatures is discovered to crack the ITO on the top plate. This seems to be due to the mismatch of linear thermal expansion coefficients between the ITO and the underlying acrylic substrate (Table 5.6.)

Table 5.6: Coefficient of linear thermal expansion and heat distortion temperature of the materials used at the top plate.

Material	CTE ($10^{-6}/^{\circ}\text{C}$)	Heat distortion ($^{\circ}\text{C}$)
ITO	8.5 ~ 10.2	
Quartz	~ 1	
Polycarbonate	37	128
Cast acrylic	70	110

After cracking, the ITO loses the necessary conductivity to function as the ground of the DM actuation voltage. In other words, with the common ITO/acrylic top plate, it becomes impossible to use DM actuation to manipulate the droplets as soon as the PCR is initiated. This is problematic because without DM actuation holding the PCR mixture droplet in place, it is likely to drift away from the sensing area of the fluorescence sensor. Hence, the construction of the Gen II top plate must be changed to make it sufficiently heat-resistant to withstand the PCR process.

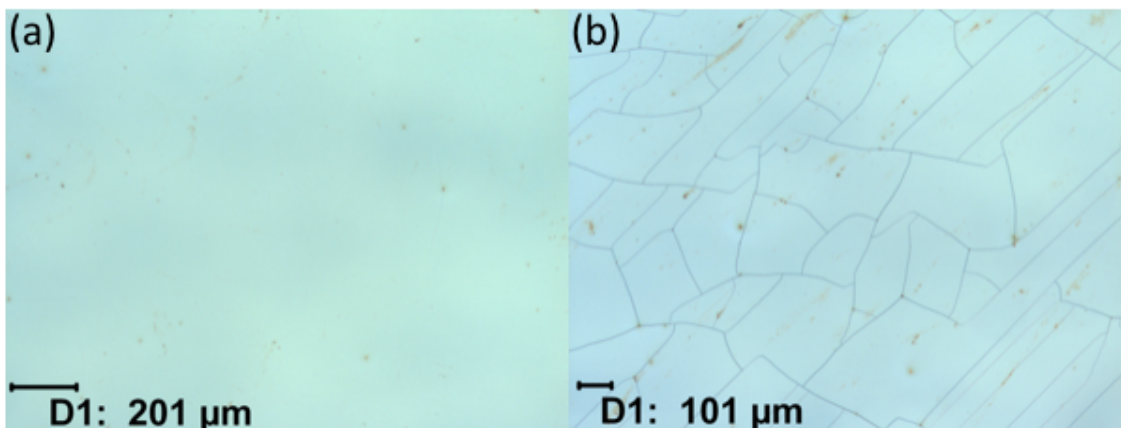


FIGURE 5.7: Cracking of ITO after 65 °C bake.

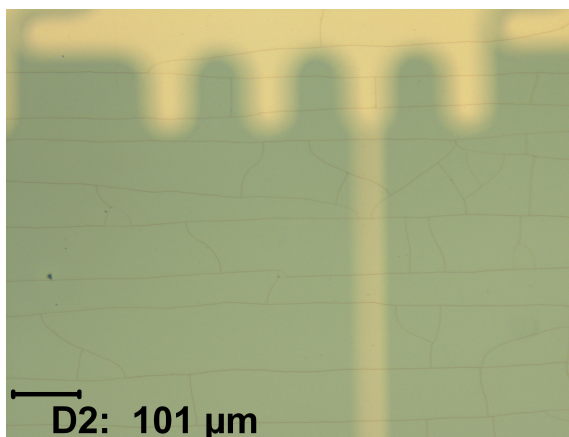


FIGURE 5.8: Cracking of ITO in ITO/PEDOT:PSS after 95 °C bake. Despite the cracking, DM actuation remains functional.

Criteria for Selecting the Top Plate Substrate

The top plate of a DM device is preferred to be transparent in order to facilitate the observation of droplet manipulation. Because of this reason, a commonly employed stack involves a 0.5 ~ 1 mm plastic substrate sputtered with 70 ~ 140 nm of the transparent conducting oxides ITO. (The discussion in this section will omit the Cytop hydrophobic coating.) The plastic substrate is advantageous in two aspects. First, it is very cost-effective. Second, it can be patterned on-site using CNC milling or laser cutting.

Additionally, pertaining to the PCR application, the concern about ITO cracking, and the fabrication throughput, the substrate of the top plate ideally should also meet the following criteria:

- High operating temperature, for instance 10 °C higher than the typical 95 °C denaturation temperature.
- Minimal CTE mismatch to ITO.
- Compatible with laser cutting, or at least CNC milling.

Regarding the second criterion, it is worth noting that having a minimal CTE mismatch between the top plate substrate and ITO generally implies that the CTE of the top plate substrate is also close to the CTE of the bottom plate substrate (silicon in this case, other typical choices include quartz and Pyrex.) Under this condition, the two plates should expand and contract by a similar amount during thermocycling, thereby facilitating the adhesion of the SecureSeal gasket to the two plates. In turn, the structural integrity of the fluidic device can be improved.

Considering the ultimate goal of integrating the photodetector to the top plate, the optimum substrate for the top plate should be quartz. However, although methods that can pattern thick quartz (e.g., 0.5 mm) with the reservoir openings and the

pipette ports (see Fig. 5.4) are known to be commercially available, none is available at the acceptable cost and turnaround. Due to this restriction, the top plate substrate is currently limited to plastics.

Since the use of glass-like materials has been temporarily ruled out, the more satisfactory choice among the typical transparent plastics remains to be cast acrylic. For example, even though polycarbonate is capable of operating at higher temperatures and closer to ITO in terms of CTE (Table 5.6), it is more difficult to mill and incompatible with the laser cutter. Also, compared with cast acrylic, the relatively common extruded acrylic has a slightly lower operating temperature. Further, it does not tolerate acetone wash.

Lastly, it is worth mentioning that manufactures are known to be developing a new generation of transparent and translucent high-temperature plastics. For instance, Solvay Plastics' polysulfone derivatives are rated at 204 °C. While these speciality/experimental polymers should be a significant improvement over cast acrylic, their general availability at the desired film thickness is not yet guaranteed.

ITO/PEDOT:PSS/acrylic

Due to the difficulty of patterning the reservoir openings and the pipette ports on glass-like materials, the substrate of the top plate is currently limited to cast acrylic. As the problem of ground electrode failure cannot be solved by changing the substrate, attention is shifted to finding an alternative transparent conductive coating, or a thin-film stack, that can maintain the function as the ground electrode at elevated temperatures.

To that end, because the use of the conductive polymer PEDOT:PSS had been briefly attempted in our research group [61], its applicability for cast acrylic plates was investigated. In terms of thermal stability, this material can withstand at least 170 °C [62]. By varying the film thickness, sequence of deposition, and fabrication

Table 5.7: Top plate sheet resistance (Ω/\square) vs. baking. Substrate: cast acrylic.

Stack	Pre-bake	100 °C bake
ITO	2.8	∞
ITO/PEDOT:PSS	3.0	∞
ITO/PEDOT:PSS (plasma)	3.0	2.7

method, a viable option is found to be ITO/PEDOT:PSS/acrylic (Fig. 5.6.) Although the PEDOT:PSS layer does not prevent the ITO from cracking (Fig. 5.8), after a 5 min bake at 100 °C the sheet resistance stays unchanged at approximately 3 Ω/\square (Table 5.7.) Further, after a fully-assembled and reagent-loaded Gen II device is thermocycled for 40 cycles, DM droplet actuation is observed to function normally (Fig. 5.9.) The result from the simulated PCR suggests that until the issue of patterning quartz can be addressed the ITO/PEDOT:PSS/acrylic top plate should suffice as the stopgap.

Notably, as can be seen in Table 5.7, oxygen plasma ashing of the acrylic immediately prior to the spin coating of PEDOT:PSS is found to be essential to the enhancement of temperature tolerance. The behavior might be related to the hydrophilicity of PEDOT:PSS.

Later on, the simpler PEDOT:PSS/acrylic top plate was also found to pass the 100 °C baking test. However, because it seems preferable to use ITO as a barrier to minimize the contact of water-soluble PEDOT:PSS with the aqueous reagents, this construction is not yet used in the on-chip qPCR experiments.

In summary, in the Gen II fluidic device the structure of the top plate is changed from ITO/acrylic to ITO/PEDOT:PSS/acrylic. Although PEDOT:PSS does not prevent the ITO from cracking, the conductivity is maintained after a simulated 40-cycle PCR. Interestingly, oxygen plasma ashing of the acrylic immediately prior to the spin coating of PEDOT:PSS is found to be essential to the enhancement of temperature tolerance.

As a temporary solution to the ITO cracking problem, the modified top plate structure is subsequently used in the on-chip qPCR experiments. Yet, the 80 °C maximum continuous operating temperature implies that under thermocycling conditions the cast acrylic may become a source of PCR inhibitors. Ultimately, a more thermally stable construction, such as PEDOT:PSS/polysulfone and ITO/quartz, needs to be developed.

5.2.3 On-Chip Heater

Three topics about the on-chip resistive heater will be overviewed in this section. First, the decision to use an on-chip heater, rather than an off-the-shelf part, will be explained. Second, the reason about positioning the heater outside the PCR mixture

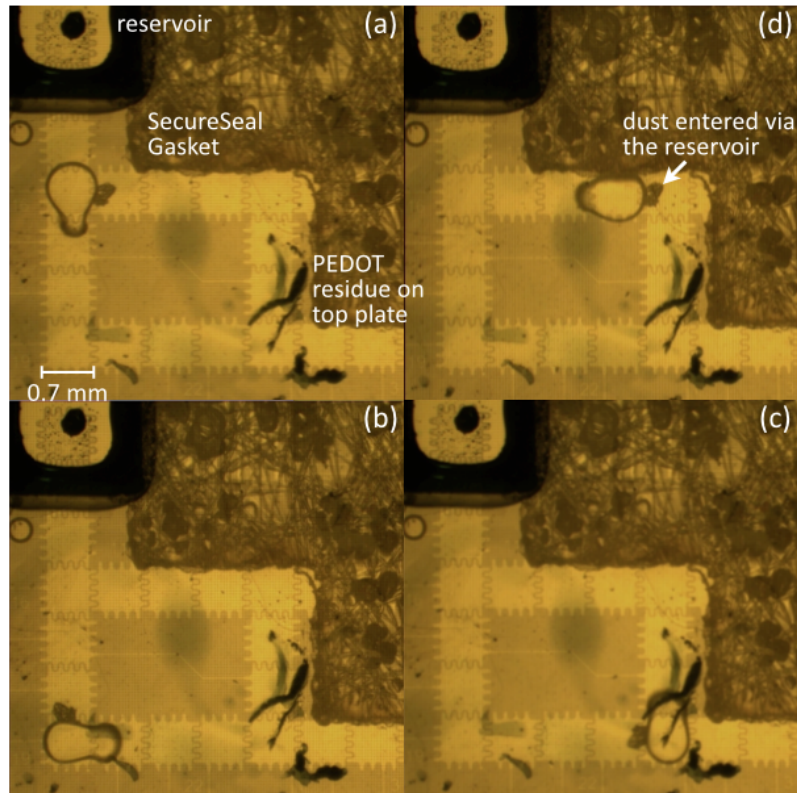


FIGURE 5.9: Counterclockwise from (a) to (d). After 40 thermocycles, a Gen II device with the ITO/PEDOT:PSS/acrylic top plate remains capable of dispensing and transporting a Tween 20 droplet.

preparation stage of the fluidic device would be discussed. Third, the properties of the developed heater are presented.

On-Chip Heater vs. Off-the-Shelf Heater

From the perspective of demonstrating the ability to combine IPF nucleic acid purification and DM PCR mixture preparation, on-chip and off-chip heaters are equally applicable. After a brief period of surveying and testing off-the-shelf heaters, it was decided to equip the Gen II fluidic device with an on-chip resistive heater. The decision is based on the three factors that will be explained in the following paragraphs.

First, due to the small footprint of the fluidic device, initial evaluations found that it is difficult for both a thermocouple and an external heater to maintain a good thermal contact with the bottom surface of the device. (The top surface is reserved for observation purposes.)

Second, off-the-shelf heaters with the desired power rating and temperature tolerance have a significantly larger thermal mass. Also, it is difficult to incorporate off-the-shelf heaters without compromising the heat dissipation. Both issues originate from the fact that commercial heaters are designed to have a constant power output and stay in thermal equilibrium with the operating environment. Since efficient heat dissipation is not a concern, to improve their durability these heaters are generally encapsulated in thick plastic layers. Consequently, most commercial heaters are unsuitable for thermocycling applications. In contrast, an on-chip resistive heater would be immune from the aforementioned drawbacks because of its negligible thermal mass.

Third, to prepare for a potential switch from full-chip thermocycling to temperature zone PCR [37], a few small on-chip heaters combined with a large off-chip thermoelectric cooler placed at the bottom surface of the fluidic device is thought to be a feasible way to create the necessary hot spots.

Heater Position

During the transition from 60 °C to 95 °C and the 95 °C dwell in a thermocycle, the heater generally is at a higher temperature than the PCR mixture droplet. Importantly, this temperature difference should be minimized because of two reasons. First, it is related to reducing the PCR time. Second, the less the heater needs to go above 95 °C, the more the polymeric materials used in the fluidic device can stay within their temperature ratings. This matters because although DM droplet actuation is serviceable during and after a PCR, the temperature involved nonetheless can approach or slightly exceed the short-term rating of some materials. (Long-/short-term rating (°C): cast acrylic 80/90, Parylene C 80/100.)

Fundamentally, the issue of exceeding the rating can only be solved by switching to the materials that are considerably more expensive and/or more difficult to process. Thus, pertaining to the materials that are realistically available, the temperature difference between the heater and the PCR mixture droplet must be decreased. This not only improves the structural integrity of the fluidic device but also mitigates the concern about the polymeric materials emitting PCR inhibitors.

A straightforward way to reduce the aforementioned temperature difference is to position the heater near the DM electrode where the PCR mixture droplet is intended to be placed. However, empirical results indicate that this layout results in severely compromised heater lifetime, i.e., less than 10 min before failure (Fig. 5.12.) The phenomenon can be explained by the degradation of Parylene C by the elevated temperature nearby the heater. The thermal degradation is observed to quickly puncture the 1.1 μm film (Fig. 5.11a.) As the puncture spreads, the electrolysis caused by the contact of the heater and the aqueous solution further damages the Parylene. This positive feedback soon leads to the failure of the heater and the nearby DM electrodes.

Since the result suggests that having the heater close to the DM electrodes and therefore potentially in proximity to the aqueous reagents will unacceptably degrade the heater lifetime, as a compromise in the final Gen II layout the heater is positioned outside the PCR mixture preparation stage of the fluidic device (Fig. 5.10.) Because the liquids cannot get in contact with the heater (Fig. 5.13), no heater at this location is observed to fail at the relevant current density. In other words, the heater can now comfortably outlive the typical PCR time.

Still, as in the case of the ITO/PEDOT:PSS/acrylic top plate, this layout should be considered as a stopgap measure meant to carry the research onwards. Ultimately, the aforementioned electrolysis problem needs to be addressed, perhaps by replacing the Parylene C layer with a more thermally robust dielectric, e.g., Parylene HT and ALD aluminum oxide.

Properties of the On-Chip Heater

After evaluating 48 designs, the heater shown in Fig. 5.11 is incorporated into the Gen II design. To simplify the fabrication, the heater and the DM electrodes are located at the same metal layer, as can be seen in Fig. 5.10. This way, no fabrication step needs to be added to build the heater. However, this choice comes with two downsides. First, the thickness of the heater cannot be independently tuned. Second, it is impossible to place the heater directly underneath a DM electrode.

Table 5.8: Properties of the on-chip resistive heater.

Property	Value
Dimensions (μm)	$180 \times 530 \times 0.1$
Resistance (Ω)	60 (+ 47 pad + 73 contact)
Max current density (A/cm^2)	2×10^6
Typ. current density (A/cm^2)	$\leq 1.5 \times 10^6$
Typ. power in on-chip qPCR (W)	$2 \sim 12$
Max sustainable power (W)	14

Since the 100 nm e-beam evaporated Cr is surprisingly resistive, the main resistive element does not need to meander as in the case of the heater pictured in Fig. 5.12. Instead, a straight trace that is 180 μm wide and 530 μm long is able to provide 60 Ω . Also, the two contact pads are estimated to contribute 47 Ω , and the contact resistance is unexpectedly high at an estimated total of 73 Ω . Together, the three amount to 180 Ω , although 160 $\Omega \sim 220 \Omega$ has been measured in practice.

(In theory, the external thermocouple in Fig. 5.13 is unnecessary since the heater itself can function as a Resistance Temperature Detector that correlates resistance with temperature. Still, localized temperature sensing requires the main heater/sensor element to be substantially more resistive than the contact pads and the contact resistance, a condition not achieved in this work. Further, on-chip RTD has been observed to be highly sensitive to moisture and contaminants [63].)

Regarding heater lifetime, when the current density is capped at $1.5 \times 10^6 \text{ A/cm}^2$, the heater is known to withstand at least 10 simulated PCR tests without failure. Even though the Mean Time Between Failures is undetermined, for this single-use device it is sufficient to ensure that the heater can comfortably outlast the duration of a PCR reaction.

To sum up, an on-chip heater is selected over an off-the-shelf part because of the guaranteed thermal contact and the negligible thermal mass. Still, placing the heater near the DM electrodes and hence close to the aqueous droplets is found to unacceptably compromise the heater lifetime. Because of this concern, the heater is prevented from contacting any liquids by positioning it outside the PCR mixture preparation stage of the Gen II fluidic device. At this location, a heater operating at the relevant current density has never been observed to fail during the course of a PCR run.

In retrospect, the decision to use an on-chip heater is perhaps too heavily influenced by the desire to minimize the thermal mass and thus the PCR time. The

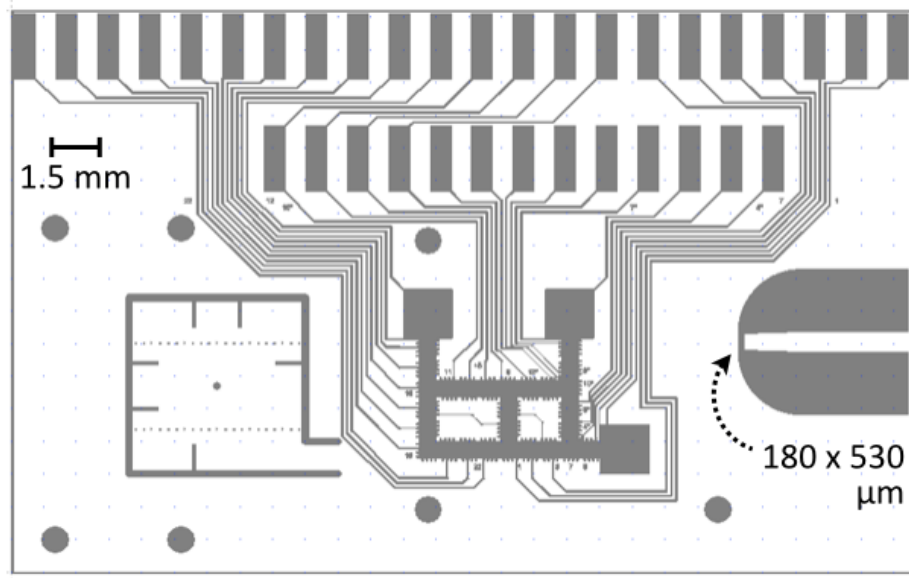


FIGURE 5.10: Photomask of Gen II fluidic device showing the Cr layer and the dimensions of the on-chip heater.

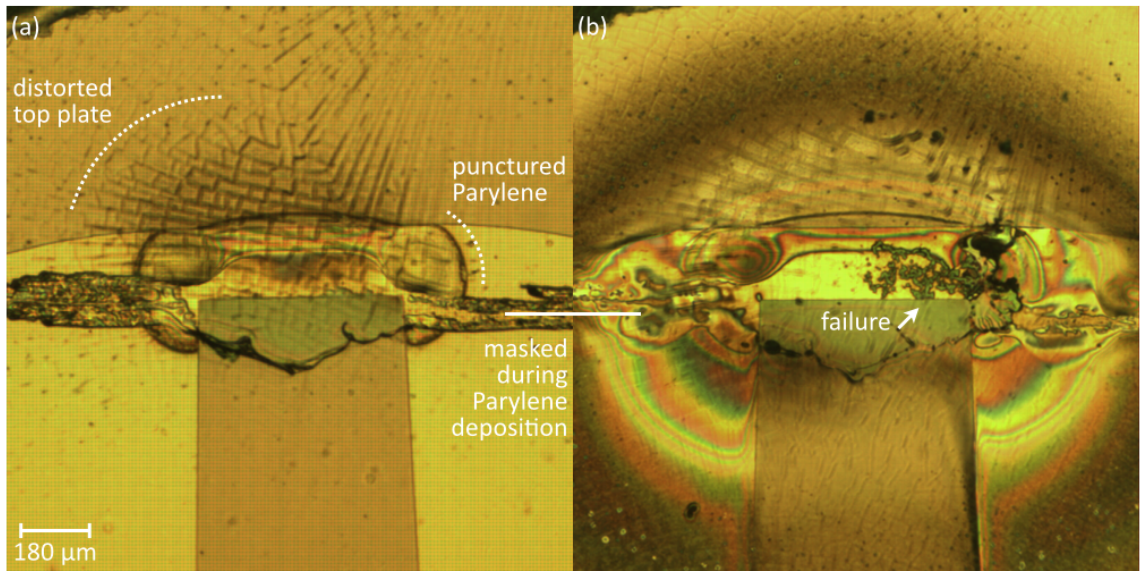


FIGURE 5.11: Used (a) and damaged (b) heater as observed through the top plate. The elevated temperature around the heater punctured the Parylene, resulting in the discoloration. To expose the contact pads, the area below the white line is masked during Parylene deposition.

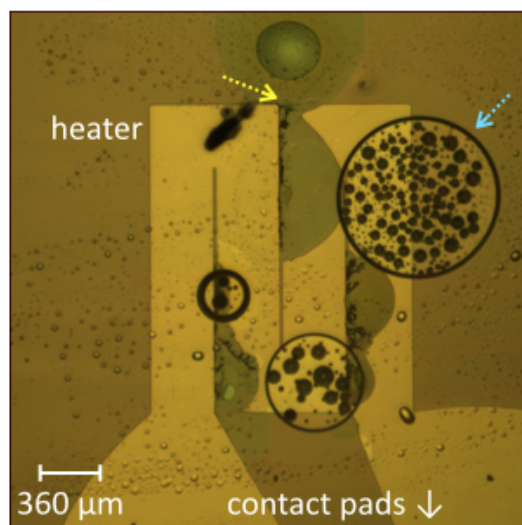


FIGURE 5.12: Placing the heater in close proximity to an aqueous reagent is found to drastically reduce its lifetime. Blue arrow: Bubble formation due to the electrolysis of water. This happened because at the onset of the failure, the Parylene stopped to insulate the heater from the water. Yellow arrow: Punctured Cr and Parylene.

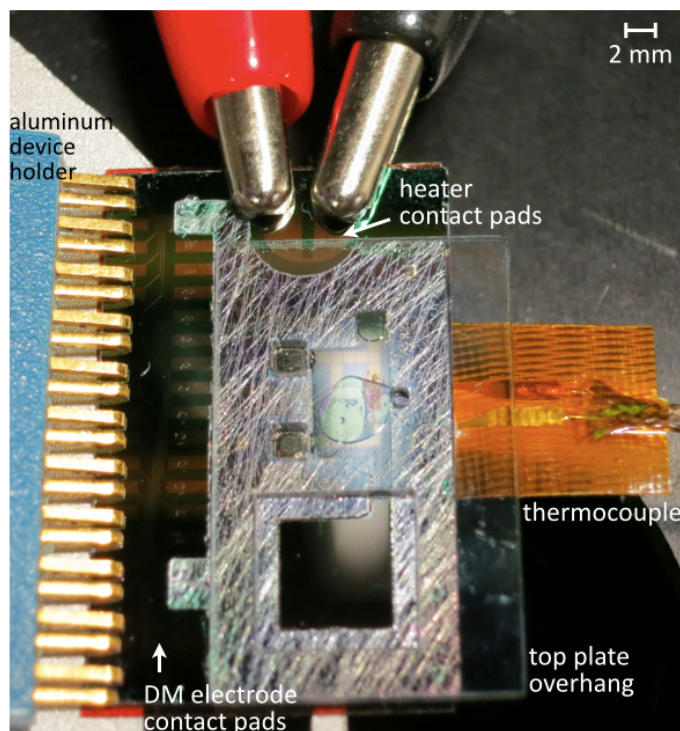


FIGURE 5.13: Electrical contacts to Gen II fluidic device. To make contact with the DM ground electrode, an alligator clip will be clamped to the top plate overhang.

shorter the PCR time, the better the polymeric components, namely the SecureSeal gasket and the ITO/PEDOT:PSS/acrylic top plate, can be preserved. However, it was later learned from the tests detailed in Sec. 5.3.1 that the entire thermal “package” must be extremely well-optimized to take advantage of the reduced thermal mass. For example, a suboptimal set of PID parameters can easily offset the benefits that may be brought by an on-chip heater.

5.3 Auxiliary Systems

After the reagents are selected and the fluidic device is designed, the remaining missing component is the auxiliary systems that are needed to support the operation of qPCR. As a whole, the auxiliary systems function as a qPCR instrument, which consisted of a thermocycler, a fluorescence sensor, and a device holder. The temperature control system that executes the thermocycling is designed to have a very fine-grained control over the temperature ramping behavior at the different phases of a thermocycle. This feature is implemented as a provision for optimizing the PCR time. Still, to take full advantage of this feature, it is found that the ramp rate dependent correlation between the thermocouple reading and the temperature experienced by the PCR mixture droplet must be well-characterized and repeatable from device to device. Another auxiliary system is the fluorescence sensor. While waiting for the integrated photodetector to be developed (Fig. 2.3), a fiber optic fluorescence sensor has been constructed as an alternative. Other than measuring the fluorescence generated by qPCR, the sensor is found to have a few other interesting uses, e.g., detecting a failing DM electrode and measuring the droplet volume. Lastly, the device holder is unexpectedly troublesome to develop. A 3D-printed ABS holder, softened by the elevated temperature, is found to be deformed by the pressure applied by the spring-loaded SOIC clip. On the other hand, for an aluminum holder

to be usable, its powerful heat sinking must be suppressed. These complications will be the subjects of the discussion in the next three sections.

5.3.1 Temperature Control

The temperature control system is responsible for modulating the on-chip heater to perform thermocycling. At the beginning of this section, an overview of the system will be provided. Then, a few notable details regarding the temperature measurement aspect of the system are briefly highlighted. Lastly, the thermocycling performance and the effects of different temperature ramp rates would be discussed.

System Overview

The temperature control system along with parts of the fluorescence sensing system are illustrated in Fig. 5.14. The temperature control system relies on the feedback from the temperature sensor to conduct two functions. First, the system regulates the on-chip heater to carry out thermocycling. Second, when cooled to a preset temperature, it will trigger the fluorescence sensing system to perform spectrum acquisition. (The fluorescence sensing system will be discussed in Sec. 5.3.3.)

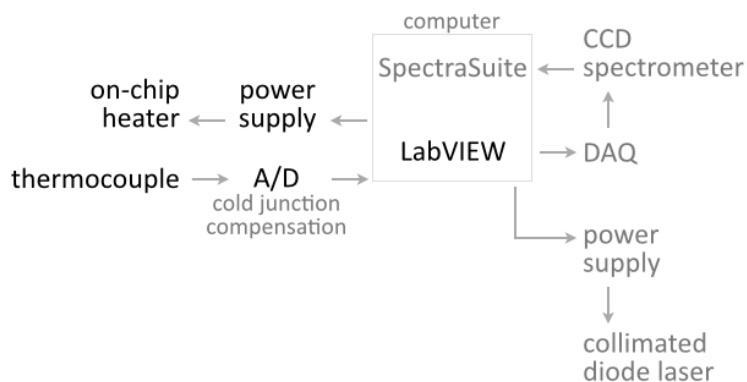


FIGURE 5.14: Temperature control system. The LabVIEW program is also responsible for controlling the laser and the spectrometer based on the feedback from the thermocouple. Also see Fig. 5.23.

The LabVIEW program in Fig. 5.14 is composed of two finite state machines: thermocycler FSM and fluorometer FSM. In particular, the thermocycler FSM controls the on-chip heater using the PID algorithm. Notably, different sets of PID parameters can be run in a thermocycle. For example, depending on the desired balance between ramp rate and overshoot, each of the following five phases in a thermocycle might employ its own set of PID parameters: $< 80^{\circ}\text{C} \rightarrow 80^{\circ}\text{C}$, $80^{\circ}\text{C} \rightarrow 90^{\circ}\text{C}$, $> 90^{\circ}\text{C}$, $> 70^{\circ}\text{C} \rightarrow 70^{\circ}\text{C}$, $< 70^{\circ}\text{C}$. This way, a very fine-grained control over the temperature ramping behavior can be obtained.

Temperature Measurement

Regarding the temperature sensor, a foil thermocouple is currently used. Among the surveyed parts, the employed Omega CO1-T is found to be especially suitable because of its $10 \sim 20$ ms short response time, 0.5°C low limits of error, and the low thermal mass. Initially, it was attempted to permanently mount the thermocouple on the device holder. This option is thought to provide more consistent alignment and thermal contact between the thermocouple and the fluidic device. However, due to the reasons that will be explained in Sec. 5.3.2, this approach was eventually abandoned. Instead, as pictured in Fig. 5.15, the thermocouple needs to be aligned and attached to the bottom of the fluidic device prior to each experiment.

In Fig. 5.15, also note that thermal paste is indispensable to the thermal contact between the thermocouple and the fluidic device. Without the paste, temperature crayons indicate that towards the ceiling of the interested temperature range the device temperature can be underestimated by as much as 55°C .

Lastly, as illustrated in Fig. 5.14, before the temperature data is read into the thermocycler FSM, the voltage signal produced by the thermocouple is first digitized at 4 Hz by an analog-to-digital converter. Importantly, cold junction compensation is handled by the NI USB-TC01 20-bit A/D with a thermistor near the receptacle

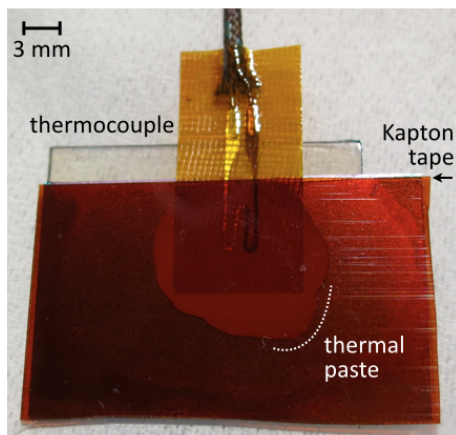


FIGURE 5.15: Thermocouple taped to the bottom of a Gen II fluidic device. The thermal paste is applied to enhance the contact between the device and the thermocouple.

of the thermocouple connector.

Thermocycling Performance

A comparison of the thermocycling performance is presented in Table 5.9. Also, the thermocycles performed using the Fast Ramp (FR) and Slow Ramp (SR) sets of PID parameters are shown in Fig. 5.16 and Fig. 5.17, respectively. In particular, Fig. 5.16 indicates that the on-chip heater generally outputs between 2 W to 12 W during a thermocycle.

Table 5.9: Temperature ramp rate and PCR time of ABI 7900HT and the in-house thermocycler at two ramp rates: Fast Ramp, Slow Ramp.

	7900HT	FR	SR
Per cycle heating/cooling rate ($^{\circ}\text{C}/\text{s}$)		4.0/2.5	2.3/1.7
Overall ramp rate ($^{\circ}\text{C}/\text{s}$)	1.4	3.4	1.8
Cycle time (sec)		41	57
PCR time (min)/cycle	55/45	30/40	42/40

Although FR is able to complete 40 thermocycles in 30 minutes (including UNG incubation 2 min and polymerase activation 20 s), the on-chip qPCR tests conducted

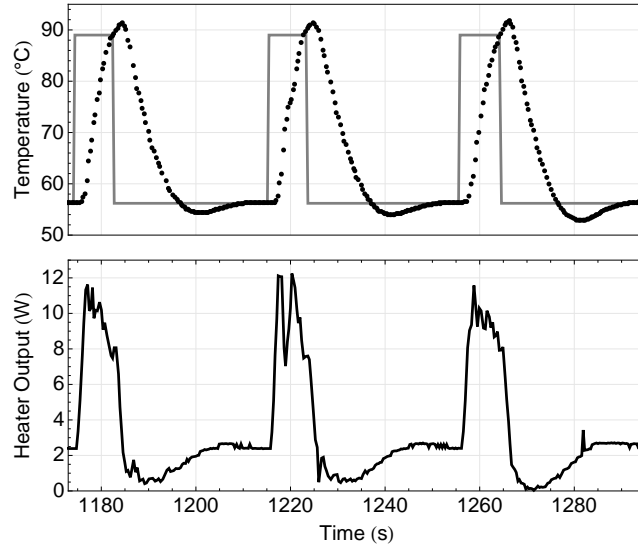


FIGURE 5.16: Three thermocycles performed with the “Fast Ramp” set of PID parameters. The gray trace represents the temperature setpoint. The transient temperature ramp rate can be visualized by observing the gap between two adjacent data points.

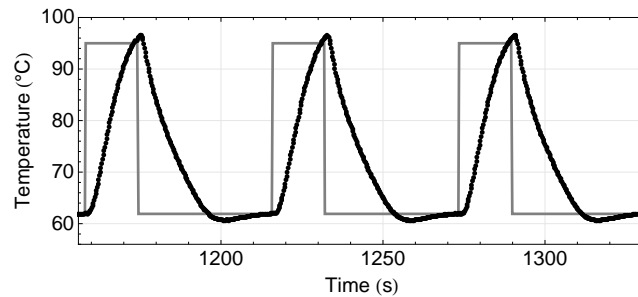


FIGURE 5.17: Three thermocycles performed with the “Slow Ramp” set of PID parameters. The gray trace represents the temperature setpoint.

using FR were unsuccessful.

A likely explanation might be inferred from the data shown in Fig. 5.19. Briefly, this experiment involved two thermocouples. The first thermocouple, T_{bottom} , is placed at the typical position shown in Fig. 5.15. The other thermocouple, T_{top} , is sandwiched between the two plates of the fluidic device and aligned to the first thermocouple. (A modified SecureSeal gasket is needed to accommodate T_{top} .) In other words, the two thermocouples are only separated by the 525 μm silicon bottom

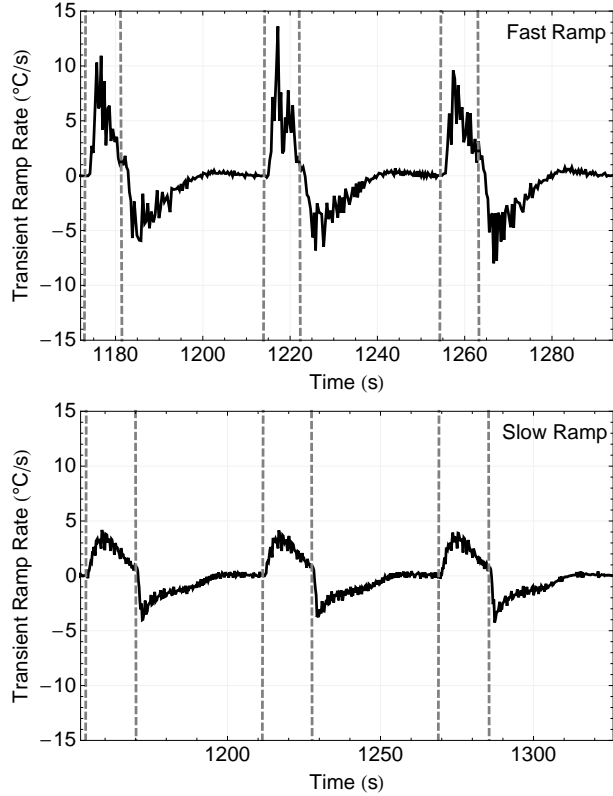


FIGURE 5.18: Transient temperature ramp rate derived from the data in Fig. 5.16, 5.17. Each dotted line indicates a change of the temperature setpoint.

plate and the thickness added by the thermal paste.

Using the described setup, thermocycles are run with higher and lower ramp rates, and a thermocycle from each condition is plotted in Fig. 5.19. First, it can be seen that the temperature difference between the two thermocouples, $T_{\text{top}} - T_{\text{bottom}}$, varies throughout the thermocycle. Second, the temperature difference is larger when the transient ramp rate is higher. The effect is particularly noticeable by comparing the behavior near and in the high temperature zone (1 s between the purple bars) in the two plots.

Because of the different thermal mass, the exact temperature difference values are not directly relevant to the typical on-chip qPCR. Still, the result suggests that: (1) at higher ramp rates, T_{bottom} becomes a lesser indicator of the temperature

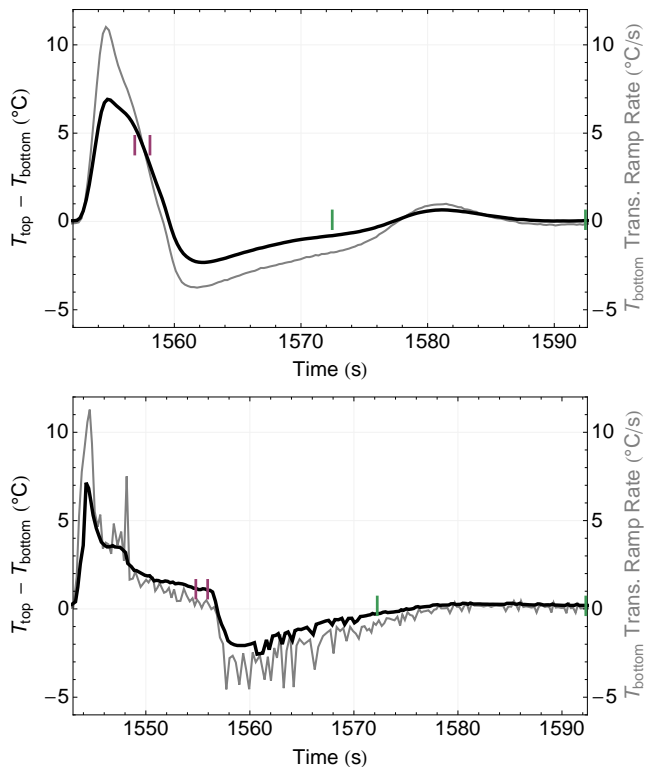


FIGURE 5.19: In the bottom plot, the ramp rate when approaching the temperature zones (colored bars) are lowered. Thus, ΔT during the temperature zones is reduced (colored bars closer to $\Delta T = 0$ °C.) Purple/green bars: 1/20 s in the high/low temperature zone.

experienced by the PCR mixture droplet, T_{droplet} , (2) the temperature setpoints can only be correctly set if the correlation between T_{droplet} and T_{bottom} is known and more importantly, repeatable from device to device. The latter is difficult to achieve, in part because the on-chip heaters are found to vary between 160 Ω to 220 Ω .

Consequently, due to the problems encountered in setting up the high ramp rate qPCR, the slightly slower SR set of PID parameters is eventually used in the on-chip qPCR experiments in Sec. 6.2. As demonstrated in Fig. 5.18, SR is specifically developed to have a lower but more repeatable ramp rate. Additionally, as SR does not throttle the on-chip heater as aggressively, it seems to be more tolerant of the aforementioned resistance variation.

In summary, a thermocycler is constructed in order to accommodate the electrical and observational requirements of DM devices. A notable feature is that different PID parameters can be run in different phases of a thermocycle. For instance, the initial ramp up from 60 °C to 95 °C may prioritize the heating rate, but from 80 °C onwards different parameters might be used to reduce the overshoot. The fine-grained control over the temperature ramping behavior will facilitate the improvement of PCR time.

However, the correlation between the thermocouple reading and the temperature experienced by the PCR mixture droplet is challenging to characterize under relevant conditions, i.e., thermocycling with an unmodified fluidic device and without extra thermocouples attached.

Since the issue of correlation is found to be more pronounced at high ramp rate, a more conservative set of PID parameters is currently used to leave room for the uncertainties in temperature setpoints and heater resistance variations. Ultimately, the obtained data suggests that with further optimizations the thermocycler would be able to complete a 40-cycle PCR in under 30 min.

5.3.2 Device Holder

The primary purpose of the device holder is to anchor the spring-loaded SOIC clip that makes contact with the DM electrode contact pads. In addition, as part of the chip-to-world interface, other application-dependent functions are frequently incorporated into a device holder, e.g., to expedite or to improve the repeatability of the pre-experiment procedures. In this section, the attempt to incorporate the fluidic device - thermocouple aligner into the 3D-printed ABS device holder will be first discussed. Then, the complications associated with aluminum device holders will be overviewed.

3D-Printed Holder with Fluidic Device-Thermocouple Aligner

In addition to anchoring the SOIC clip that makes contact with the DM electrode contact pads (Fig. 5.22), 3D-printing permits more sophisticated device holders to be designed. For instance, an aligning mechanism can be incorporated into the device holder to ensure the alignment of the thermocouple measurement junction to the desired position on the fluidic device, e.g., the on-chip heater (Fig. 5.20, 5.21) or a particular DM electrode (Fig. 5.22.)

In this way, the thermocouple can be permanently mounted on the holder, thus eliminating the step to tape it to a fluidic device prior to each experiment. The latter not only decreases the consistency of the alignment, it is also cumbersome to manually handle the fluidic device through IPF washes with the rigid glass braided wire of the thermocouple interfering. In addition, as it is unnecessary to align and tape the thermocouple to the device before an experiment, the possibility of contaminating the device is reduced.

However, these 3D-printed holders are found to become unusable after a few PCR experiments. This is because the downward pressure applied by the spring-loaded SOIC clip to the holder's device-contacting surfaces would deform the ABS that is already softened by the elevated temperature, as pictured in Fig. 5.20(d). As the deformation gradually detaches the thermocouple from the fluidic device, it becomes increasingly difficult for T_{TC} to match T_{SP} . In turn, the PID algorithm compensates by deploying the heater at higher power and with longer duration, thereby exacerbating the softening of ABS. This positive feedback cycle quickly renders a holder unusable. (T_{TC} : thermocouple reading, T_{SP} : temperature setpoint.)

Aluminum Device Holder

Since 3D-printed ABS holders are found to deform during thermocycling, aluminum device holders were used instead. Although aluminum holders do not suffer from the

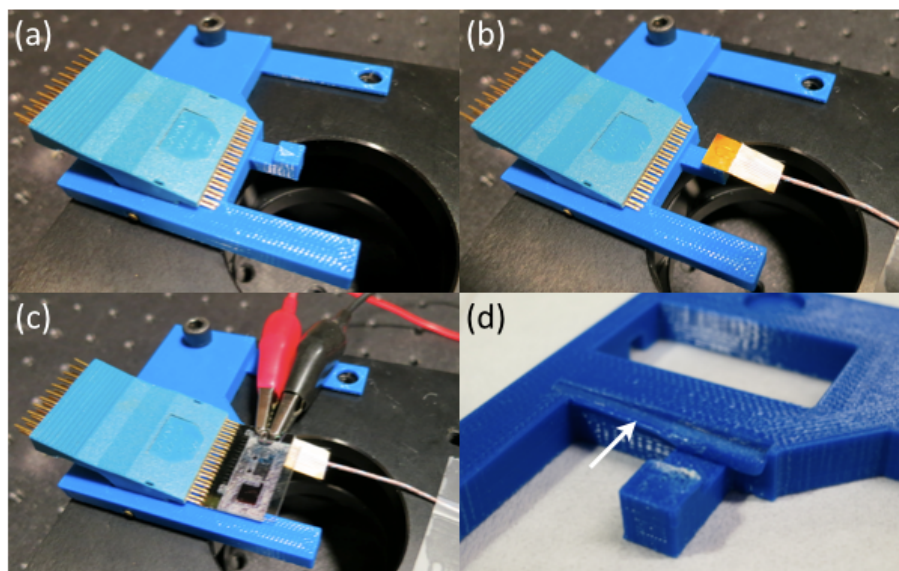


FIGURE 5.20: (a ~ c) As the fluidic device is mounted onto the holder, the on-chip heater is self-aligned to the metal junction of the thermocouple. (d) The deformed holder (arrow) ruined the thermal contact between the device and the thermocouple.

deformation issue, their adoption was not without complications.

First, because of the high thermal conductivity of aluminum, the fluidic device cannot be directly placed on an aluminum holder. Instead, as demonstrated in Fig. 5.22, two layers of Kapton tape needed to be applied to the device-contacting surfaces to mitigate the overly powerful heat sinking. (Thermal conductivity in W/m·K: 6061-T651 aluminum 167, ABS 0.19.)

The heat sinking effect of the aluminum holder is evident in Table 5.10. In this experiment, fragments of the temperature crayons were utilized to monitor the temperature at the PCR mixture preparation stage. For a Gen II bottom plate mounted on an ABS holder, 8.8 W heater output is able to keep the 93 °C crayon melted. On the other hand, without Kapton insulating the bottom plate from the aluminum holder, the on-chip heater outputting at nearly its maximum sustainable power is unable to attain more than approximately 70 °C.

In a subsequent evaluation, the effect of the Kapton tape was observed by placing

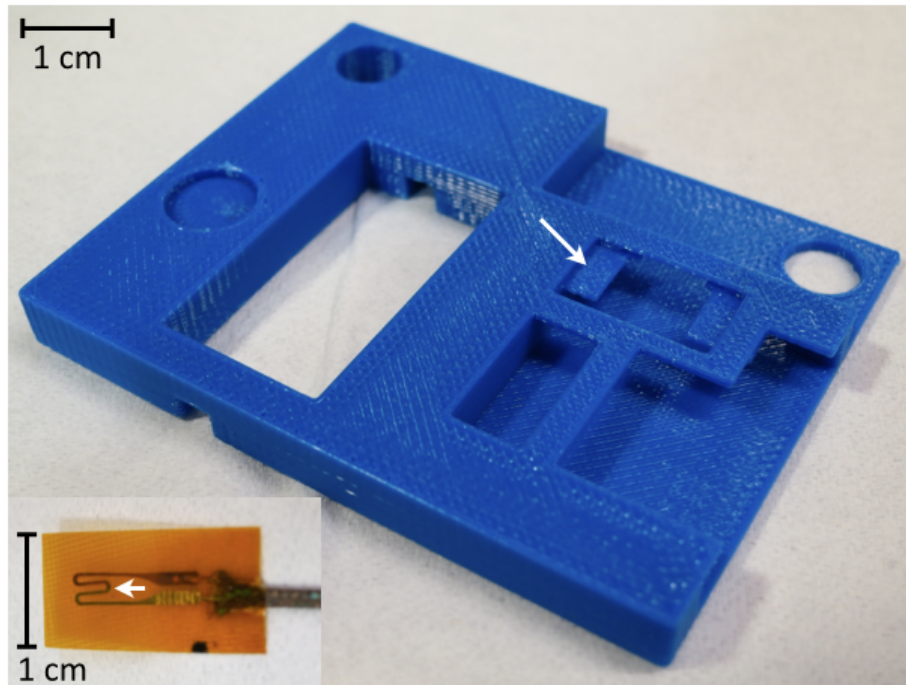


FIGURE 5.21: Aligner (arrow) built-in to the 3D-printed device holder aligns the on-chip heater to the metal junction of the thermocouple (inset, arrow.)

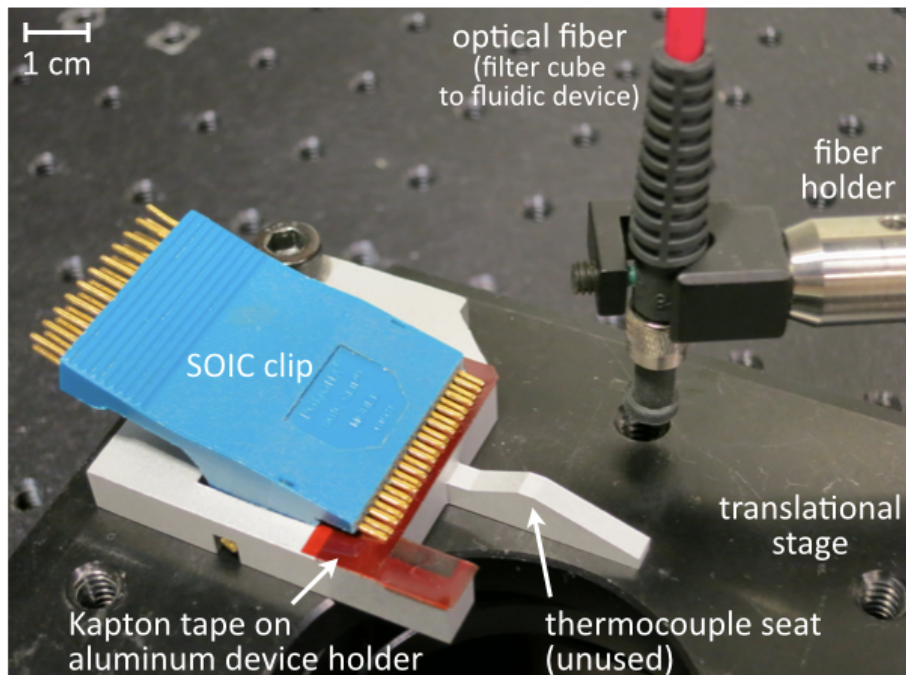


FIGURE 5.22: Two layers of Kapton tape are applied to the aluminum device holder to mitigate the heat sinking. The optical fiber is part of the fluorescence sensor.

Table 5.10: Heat sinking effect of the aluminum device holder.

Heater (W)	Holder	Tape (Layer)	Behavior
8.8	ABS	0	Sufficient to hold at 95 °C.
8.8	Al	0	Sufficient to hold at 60 °C.
13.5	Al	0	Only reaches ~ 70 °C.

a second thermocouple in the PCR mixture preparation stage of a modified Gen II fluidic device, i.e., sandwiched between the two plates. With two thermocouples, the temperature difference between the heater T_{heater} and the PCR stage T_{drop} can be monitored. In Table 5.11, it can be seen that to attain $T_{\text{drop}} = 95$ °C, without any tape it takes $T_{\text{heater}} = 101.5$ °C. In contrast, with two layers of Kapton tape insulating the fluidic device from the aluminum holder the required T_{heater} is reduced to a more reasonable 97.5 °C. A third layer of Kapton does not discernibly lower T_{heater} any further. (This test involves a device with a different thermal mass and necessitates a different set of PID parameters. Hence, the relationship between T_{heater} and T_{drop} described here is not directly applicable to a typical on-chip qPCR experiment.)

Table 5.11: T_{heater} (°C) needed to reach $T_{\text{drop}} = 95$ °C 1 s/60 °C 20 s vs. layers of Kapton tape between the fluidic device and the aluminum holder.

Tape (Layer)	$T_{\text{drop},60}$	$T_{\text{drop},95}$
0	63.1	101.5
1	62.7	99.8
2	61.9	97.5

Second, although aluminum holders do not deform and thus do not distort the alignment and the separation between the fluidic device and the thermocouple, the approach of permanently mounting the thermocouple on the device holder remains problematic. For example, the aluminum holder shown in Fig. 5.22 was originally designed to align the thermocouple to the DM electrode where the PCR mixture droplet was intended to be positioned. Yet, again because of the high thermal con-

ductivity of aluminum, this arrangement was found to rapidly sink the heat away via the device bottom surface - thermal paste - thermocouple - Kapton tape - aluminum holder path. Additionally, as a consequence of the heat sinking, the reading from a thermocouple mounted on Kapton tape/aluminum holder would be a gross underestimation of T_{drop} .

The results suggest that even though mounting the thermocouple on the device holder is beneficial, in practice it is difficult to implement without a holder made of a material with a high softening temperature and a suitable thermal conductivity. In the end, the aluminum holder pictured in Fig. 5.22 was employed in the on-chip qPCR tests, but its thermocouple seat was unused. Instead, as shown in Fig. 5.15, the thermocouple needed to be aligned and taped to the bottom surface of the fluidic device before each experiment.

In summary, 3D-printed ABS device holders cannot be used. This is because the pressure applied by the spring-loaded SOIC clip deforms the ABS that is already softened by the elevated temperature. Although aluminum device holders do not suffer from the deformation issue, the high thermal conductivity of aluminum leads to different complications. For example, a fluidic device cannot be directly placed on the holder. Rather, in order to mitigate the overly powerful heat sinking, layers of Kapton tape must be applied to the device-contacting surfaces of the holder. Also, since it is unsuitable to permanently mount the thermocouple on the aluminum device holder, now the thermocouple must be aligned and taped to the bottom surface of the fluidic device before each experiment.

5.3.3 Fluorescence Sensing

Since the aim of this work is to develop a single-chip solution that incorporates the purification and the detection of nucleic acids, a sensor is needed to analyze the fluorescence generated by on-chip qPCR. To this end, as a stepping stone to

the integrated thin-film photodetector, a fiber optic fluorescence sensor has been custom constructed. The first part of this section will discuss the construction, implementation issues, and the performance of the sensor. Then, three other potential applications of the sensor that are highly relevant to DM devices will be summarized in the second part of the section.

Purpose

In parallel with the development of the integrated thin-film photodetector by the Jokerst group (Fig. 2.3), an off-chip fiber optic fluorescence sensor has been constructed and characterized. An off-chip solution was needed because of roadmap-related reasons. Initially, before the development of the thin-film sensor is completed, a fluorescence sensor with consistent performance was necessary to debug on-chip qPCR. Later on, reproducible on-chip qPCR will in turn serve as a stable platform for evaluating the integrated photodetector. Also, the on-chip sensor can be benchmarked against the off-chip system.

Sensor Construction

Off-the-shelf fluorescence sensing solutions are found to be unsuitable or cost prohibitive for our application, in part due to the complex requirements imposed by the fluidic and thermocycling aspects of the application. Thus, a fiber optic fluorescence sensor has been constructed in-house. As illustrated in Fig. 5.23, the sensor consisted of five major components:

- A 4.5 mW 532 nm collimated diode laser that is directly attached to the filter cube. Its power supply is controlled by the LabVIEW program.
- A filter cube installed with three filters (532 \pm 5 nm excitation filter, 544 nm dichroic mirror, and 555 nm long-pass emission filter) and two fiber couplers.

- Two optical fibers: cube-to-device (0.22 NA, 550 μm core) and cube-to-spectrometer (0.22 NA, 910 μm core.)
- A CCD spectrometer that will capture the 360 \sim 1000 nm spectrum when triggered by the LabVIEW program.
- A LabVIEW program that, when activated by a separate LabVIEW program that handles the PID temperature control, will turn on the laser, trigger the spectrometer, and then turn off the laser. This process is repeated for each thermocycle.

As an epi-illumination system, in addition to delivering the excitation light to the PCR mixture droplet, the cube-to-device fiber is also responsible for collecting the resulting fluorescence (Fig. 5.24.) Since the fiber and the droplet are only separated by 0.79 mm, collection loss is reduced. (0.79 mm = 0.5 mm top plate + 0.29 mm gap as spaced by two No. 1 cover slips. The cover slips are removed after the fiber is positioned.)

Although adequate for the on-chip qPCR tests, the fluorescence sensor currently suffers from two notable issues:

- No shutter between laser and filter cube: Ideally, the laser should remain on during the course of an experiment. This way, the laser can reach the thermal equilibrium to stabilize its optical output. However, since the in-house sensor does not have a shutter between the laser and the filter cube, leaving the laser on will rapidly photobleach the dyes in the PCR mixture. To circumvent this issue, in each thermocycle the laser is only turned on when the thermocouple is cooled to a setpoint near 60 $^{\circ}\text{C}$. After warming up the laser for 300 ms, the spectrometer integrates for 300 ms. Then, the laser is turned off 1 ms after the integration is complete.

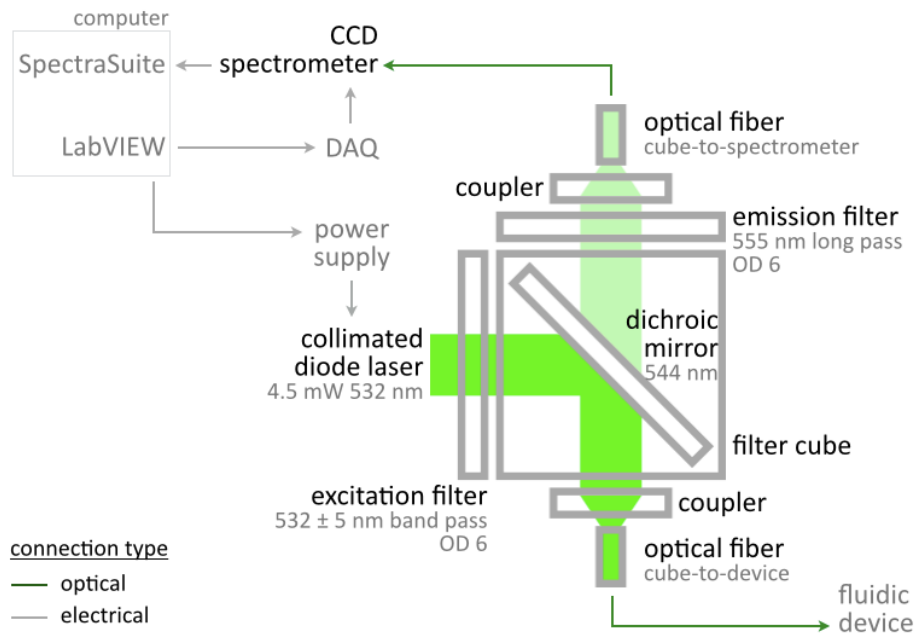


FIGURE 5.23: Schematic of the custom-built fluorescence sensor.

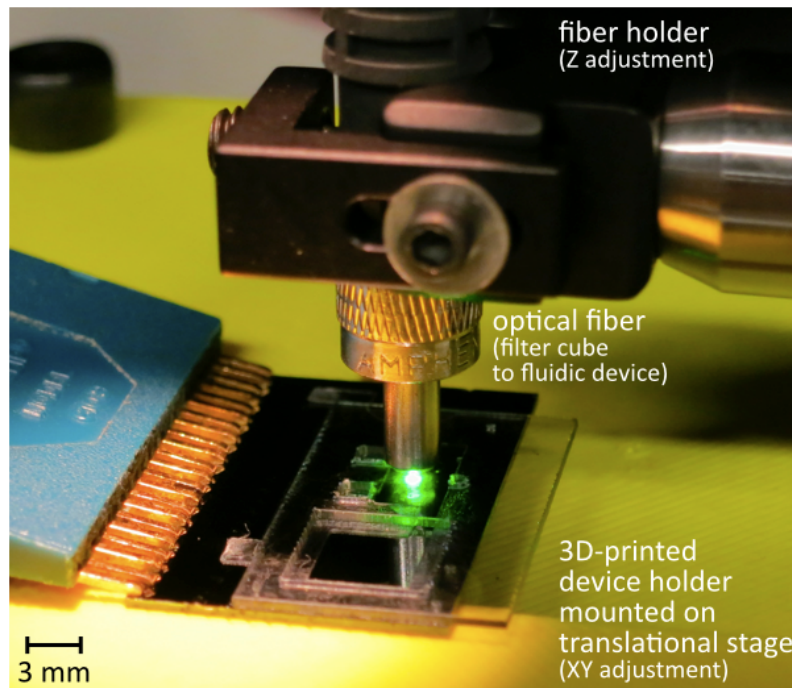


FIGURE 5.24: Custom-built fluorescence sensor positioned on Gen II fluidic device.

- Spectrum averaging incompatible with the needed triggering mode: A method to improve S/N is spectrum averaging. (Still, as it prolongs the exposure of the PCR mixture to the laser, the potential S/N improvement needs to be balanced against the increased photobleaching of the dyes.) In the case of the in-house sensor, because of a bug in the firmware of the CCD spectrometer, spectrum averaging cannot be used without changing to a triggering mode that has an unacceptable timing precision. Hence, spectrum averaging is unperformed in the on-chip qPCR experiments.

Sensor Performance

Selected attributes of the constructed fluorescence sensor are tabulated in Table. 5.12. Although some characterizations were performed in conditions different from the final on-chip qPCR tests, the table nonetheless provides an overview of the sensor’s general capability.

Table 5.12: Properties of the custom-built fluorescence sensor.

Property	Value	Note
Optical power	4.4 mW	at laser head
	4.1 mW	at fiber ¹ /top plate interface
Laser optical power stability	±3%	as configured in on-chip qPCR
Spectral resolution ²	28 nm FWHM	as configured in on-chip qPCR
Responsivity ³	204 count/nM	for ATTO 532 dye ⁴
Detection limit ³	0.24 nM	for ATTO 532 dye
Sensing area	~ ∅700 μm	fiber butt-coupled to top plate

¹ 0.39 NA, 1000 μm core.

² Boxcar smoothing: 4 pixels.

³ 40 ms integration × 20 averaging.

⁴ Similar spectral response to HEX, but more resistant to photobleaching.

In particular, during the evaluation of the sensing area (Fig. 5.25), in addition to measuring the fluorescence generated by qPCR the sensor was found to be useful for three other tasks. Given their potential significance to DM devices, these alternative applications will be discussed in the rest of the section.

Alternative Application 1: Droplet Detection

When the cube-to-device fiber is butt-coupled to the top plate of the fluidic device, the data presented in Fig. 5.25 indicates that the sensing area is approximately equal to the area of a DM electrode. Hence, the sensor can be used to detect the presence of a fluorescent droplet on the DM electrode that is directly underneath the fiber. Importantly, the detection will not be interfered by the fluorescent droplets at nearby electrodes.

As can be seen in Fig. 5.25, the sensor positioned above electrode #1 correctly detected the droplet during $t = 1 \sim 3$ s and $6 \sim 8$ s. Also, there is no false positive during $0 \sim 1$ s and $5 \sim 6$ s, when the droplet is at electrode #22 and #2, respectively.

Because the CCD spectrometer does not employ wavelength scanning, the demonstration suggests that droplet detection and composition measurement (i.e., fluorophore type and concentration) might be simultaneously completed in a short spectrum acquisition step, e.g., 0.8 s = 40 ms integration \times 20 averaging.

Alternative Application 2: Electrode Failure Detection

In addition, if the DM electrode that is underneath the fiber fails, the microbubbles generated by the electrolysis of an aqueous droplet (at this point the Parylene C in Fig. 5.6 is already broken) have been observed to cause the detected background fluorescence to erratically fluctuate. In other words, at least for this relatively common failure mode, the fluorescence sensor is capable of detecting a failing DM electrode. Consequently, it should be feasible to automatically terminate the voltage applied to the failing DM electrode as soon as the fluctuating background fluorescence is sensed. This way, the dielectric breakdown can be prevented from cascading to the neighboring DM electrodes. (An example of the background fluorescence can be seen in Fig. 5.25.)

Similarly, the presence of a water droplet in the sensing area has been measured

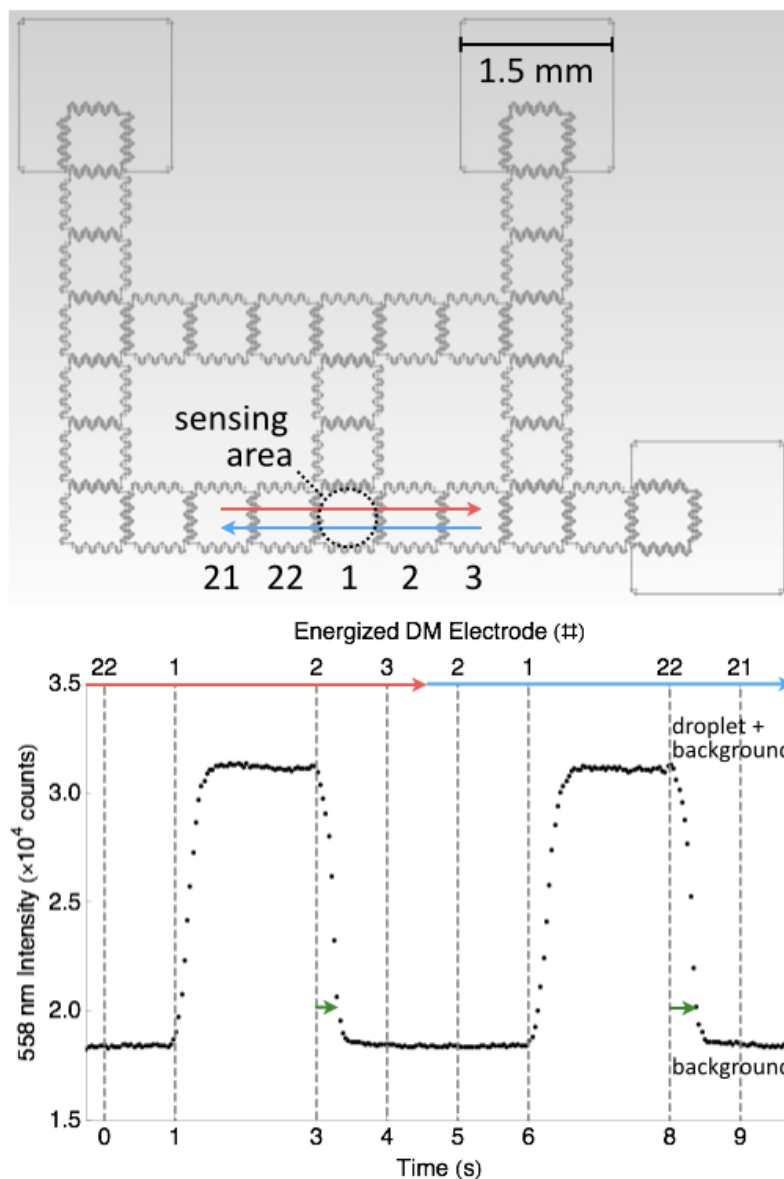


FIGURE 5.25: A fluorescent droplet is moved in and out of the fiber sensing area. Arrows superimposed on the photomask: The path of droplet transportation. In the bottom plot, each dotted line indicates the start of a droplet actuation step. E.g., at $t = 3$ s the droplet is transported from electrode #1 to #2. Spectrometer: 40 ms integration, no averaging.

to increase the detected background fluorescence by approximately 6%. Therefore, by monitoring the variation in background fluorescence the sensor can even detect the presence of a non-fluorescent droplet.

Alternative Application 3: Droplet Volume Detection

Another potential use of the fluorescence sensor that is being investigated is the measurement of droplet volume. Specifically, as long as the spectrum acquisition time is kept short relative to the droplet velocity (i.e., a relatively low DM actuation voltage is perhaps preferred in this application), the sensor can resolve the time it takes for the “tail” of a fluorescent droplet to leave the sensing area (Fig. 5.26.) This transit time is indicated by the green arrows in Fig. 5.25.

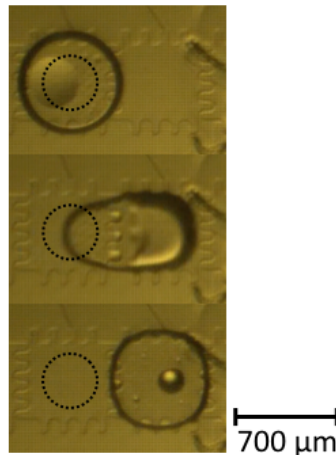


FIGURE 5.26: The time it takes for the tail of a droplet to leave the sensor field-of-view (simulated as the dotted circle) may be correlated with the droplet volume.

Accordingly, if the tail of a larger droplet (e.g., a 2x droplet obtained from merging two 1x droplets) can be shown to take a longer amount of time to leave the fiber field-of-view, it may be feasible to correlate the transit time with the droplet volume. The approach is highly advantageous because three types of information can be obtained at once from a single spectrum acquisition step: droplet volume, fluorophore types, and fluorophore concentrations.

Furthermore, by observing the variation in background fluorescence as discussed in Alternative Application 2, this method might be equally applicable to non-fluorescent droplets.

In summary, as a stepping stone to the integrated thin-film photodetector, a fiber optic fluorescence sensor has been constructed. Although hampered by the lack of a shutter between the laser and the filter cube and a firmware bug that prevents the use of spectrum averaging, the sensor in its current incarnation is adequate for on-chip qPCR experiments. In addition to measuring the fluorescence generated by qPCR, the in-house sensor is able to detect fluorescent droplets, non-fluorescent droplets, and the microbubbles that are indicative of a failing DM electrode. Also, droplet volume measurement appears to be feasible. In other words, with further optimizations applied to the sensor, a single short spectrum acquisition step could identify the dye types, dye concentrations, and droplet volume - a capability useful for a wide range of applications.

5.4 Chapter Summary

The progress described in this chapter represents the groundwork for the on-chip verifications in Ch. 6. These tasks are divided into three categories: assay, fluidic device, and auxiliary system. The three categories need to work in unison in order to demonstrate the feasibility of combining IPF nucleic acid purification and DM PCR mixture preparation on one fluidic device.

A qPCR assay found to be suitable for the on-chip tests is the Alu Yb8 assay. It detects a human-specific target that has a very high copy/genome ratio, which would facilitate the debugging of the on-chip protocols in the events of low nucleic acid yield from on-chip lysis or suboptimal retention throughout the on-chip purification. Later on, the evaluation of on-chip lysis may take advantage of the on-campus availability

of HeLa cells. Thus, for the sake of consistency HeLa gDNA is currently used as the source of Yb8. Still, since the copy number of Yb8 in HeLa is unknown, in the conversion from HeLa gDNA weight to Yb8 copy number HeLa gDNA is assumed to be equivalent to human somatic cell gDNA.

The Alu Yb8 assay will be combined with the Fast Advanced master mix to perform the majority of the qPCR reactions in Ch. 6. This master mix uses the UNG/dUTP mechanism to prevent the amplicons from contaminating later PCR reactions. The feature is desirable because the fluidic device is not fully sealed. Also, its short 95 °C 1 s/60 °C 20 s dwell times when combined with an optimized thermal system might substantially reduce a 40-cycle PCR time to approximately 30 min. In turn, the structural integrity of the fluidic device could be better preserved.

Regarding the fluidic device, purification and PCR each presents an issue that needs to be solved.

First, the design of the purification stage needs to be scalable in terms of the volume of the purification reagents that can be accommodated. This is overlooked in the Gen I device, which stores the purification reagents in upsized DM reservoirs (Fig. 5.2, 5.3.) The resulting large device footprint would necessitate an impractical amount of fabrication time to meet the consumption of these single-use devices. Afterwards, recognizing that the purification reagents need not be confined by the parallel plates, the purification stage of the Gen II device is not covered by the top plate (Fig. 5.4, 5.5.) No longer squeezed by the 120 μm gasket thickness, the reagents can regain a droplet form. Hence, for a given reagent volume the occupied area is considerably smaller. Conversely, this “coverless” implementation of the purification stage could be scaled up more efficiently. With the improvement, the Gen II layout trims the footprint of the purification stage by 84% and improves the fabrication throughput by 83%. Importantly, the thermal mass is correspondingly reduced. This is despite the addition of the third reservoir and the on-chip resistive heater.

The second issue is related to the ability to perform DM droplet actuation at elevated temperatures. Without DM actuation to hold the droplet in place during thermocycling, the slight deformation of the top plate and the gasket will cause the droplet to drift away from the sensing area of the optical fiber. Yet, because of the CTE mismatch between the ITO electrode and its polymeric substrate, when heated the ITO will crack and lose the necessary conductivity to function as the ground of the DM actuation voltage. This is temporarily addressed by changing the structure of the top plate from ITO/acrylic to ITO/PEDOT:PSS/acrylic. Although PEDOT:PSS does not prevent the ITO from cracking, the conductivity is maintained after a simulated 40-cycle PCR. Notably, oxygen plasma ashing of the acrylic immediately prior to the spin coating of PEDOT:PSS is found to be essential to the enhancement of temperature tolerance. In the long run, however, a more thermally stable construction, such as PEDOT:PSS/polysulfone and ITO/quartz, should be employed.

Other than the two application-oriented improvements that are summarized above, the usefulness of the techniques developed to reduce the fabrication time of DM devices should not be neglected. Conventionally, the gasket is fabricated using SU-8 photolithography, and the top plate is CNC milled. Both steps are highly time consuming and do not necessarily yield the optimal results. For example, thick SU-8 is prone to cracking during fabrication, and the stiff SU-8 gasket does not adequately seal the gap between the two plates. To address these concerns, the Gen II fluidic device uses a SecureSeal gasket and Clarex cast acrylic top plate. With the material change, laser patterning can now be used to rapidly fabricate the gasket and the top plate in large quantities. Also, mask-less manufacturing permits the designs to be modified on-demand. Perhaps more importantly, the SecureSeal gasket, which is essentially a double-sided adhesive film, was demonstrated to provide a far superior sealing than the SU-8 counterpart.

With the reagents selected and the fluidic device designed, the auxiliary systems still need to be built before on-chip evaluations can be conducted. This is unavoidable due to the lack of compatible off-the-shelf solutions. As a whole, the auxiliary systems function as a qPCR instrument, which consists of a thermocycler, a fluorescence sensor, and a device holder.

At the moment, the thermocycling performance is hindered by the difficulty of characterizing the ramp rate-dependent correlation between the thermocouple reading and the temperature experienced by the PCR mixture droplet under relevant conditions, i.e., thermocycling with an unmodified fluidic device and without extra thermocouples attached. Therefore, a more conservative set of PID parameters is being used to leave room for the uncertainties in temperature setpoints and heater resistance variations.

Interestingly, other than measuring the fluorescence generated by qPCR, it seems feasible to adapt the fiber optic fluorescence sensor for applications such as detecting a failing DM electrode and measuring the droplet volume. The latter would be a particularly useful capability for DM systems.

Lastly, it is worth noting that frequently more robust solutions to the encountered problems are known to exist yet are inaccessible in practice due to budgetary or turnaround constraints. Therefore, the challenge here is to develop a reasonable combination of wetware, hardware, and software with the obtainable resources. Although there is certainly room for improvement, as will be demonstrated by the results presented in Ch. 6, this goal is indeed attained.

Experimental Results

This chapter will present the results from the wet experiments. Based on the experimental method, the chapter is divided into three parts. First, in Sec. 6.1, the effectiveness of on-chip purification is assessed by off-chip absorbance measurements. In contrast, in Sec. 6.2, on-chip purification is followed by on-chip qPCR. This is used to verify the previous estimation of the purification power, and to measure the retention of nucleic acids throughout the workflow. Importantly, these two experiments demonstrated the feasibility of the proposed IPF - DM integration. Lastly, the performance of on-chip qPCR is discussed in Sec. 6.3.

Note that each section generally contains an overview of the employed experimental method. Separately, the experimental methods are detailed in Appendix A.

6.1 Estimation of Purification Power

As discussed in Appendix B, PDMS-on-glass devices were initially employed as a low-cost stand-in to obtain the initial experience with immiscible phase filtration. PDMS molding, however, is difficult to integrate into the fabrication process of digital

microfluidic devices. For this reason, the fluidic device detailed in Sec. 5.2 and other devices of similar construction were developed and used in all subsequent tests. The IPF- and DM-compatible, high fabrication throughput design provides a stable platform for more sophisticated experiments. As a first step, Sec. 6.1 will begin to evaluate the effectiveness of IPF-based on-chip purification.

First, the GuSCN concentration range in the PCR mixture that starts to inhibit qPCR is determined in Sec. 6.1.1. This is done by gradually increasing the amount of GuSCN added to the reaction mixture and then observing the resulting variation of the threshold cycle. In later experiments, a sufficient number of IPF washes has to be performed in order to lower the inhibitor concentration in the PCR mixture droplet to below the determined concentration range.

Second, in Sec. 6.1.2, on-chip purification is conducted with a varying number of IPF washes. Then, by correlating the UV absorption with GuSCN concentration, the extent of contamination in the simulated eluent can be determined. Here, the absorbance method is preferred because the data it provides is independent of the custom-developed on-chip qPCR. Further, by taking advantage of the NanoDrop instrument, the absorbance of the microliter-sized eluent generated by the purification stage of the fluidic device can be directly measured without any dilution.

Combining the results obtained in Sec. 6.1.1 and 6.1.2, the minimum number of IPF washes needed to attain uninhibited qPCR can be estimated. Afterwards, this estimation will be tested in Sec. 6.2 with on-chip qPCR.

6.1.1 Effect of GuSCN on PCR

Although convenient for initial evaluations such as Appendix B, food dyes are not the contaminants typically encountered in qPCR-based diagnosis. Therefore, in the following studies it was necessary to replace Red 40 with an applicable PCR inhibitor. To this end, after assessing candidates such as hemoglobin, human serum albumin,

and fluorescent protein [64, 65], the chaotropic agent guanidine thiocyanate (GuSCN) was eventually selected.

Primarily, GuSCN is chosen because it is directly relevant to the current workflow: it exists in Lysis Buffer and Wash Buffer 1 of the miniMAG purification kit (LB and WB1, respectively.) Between the two buffers, WB1 contains more concentrated GuSCN at 5 M. Also, WB1 is encountered relatively downstream in the purification process. Hence, subsequent calculations assume $C_{\text{inhibitor,in}} = 5 \text{ M}$.

On the other hand, because reference values are unavailable in the literature, the PCR inhibiting concentration of GuSCN needs to be determined. This concentration can be found by raising the GuSCN concentration in the reaction mix until benchtop qPCR shows a delayed threshold cycle C_t .

Following the experimental method detailed in Appendix A.1, the resulting amplification plot is shown in Fig. 6.1, and the C_t - GuSCN relationship is summarized in Table 6.1. The data indicates that GuSCN starts to impede PCR at $25 \sim 50 \text{ mM}$ in a reaction mix. In other words, under the relatively ideal benchtop PCR conditions, a purification power of at least $5 \text{ M} / 25 \text{ mM} = 200$ is needed. Furthermore, since the initial on-chip PCR will be less optimized than benchtop PCR (for instance, the polymerase activation step might be too cold or too short to activate all DNA polymerase), it is expected to be more sensitive to inhibitors. Thus, on-chip PCR may require a purification power that is somewhat higher than 200. (The $25 \sim 50 \text{ mM}$ range was later found to be in line with the $20 \sim 40 \text{ mM}$ range shown in [66].)

Table 6.1: PCR inhibition by GuSCN.

GuSCN(mM)	PCR behavior
≥ 158	No amplification
50	C_t delayed by 3 cycles
≤ 25	Normal

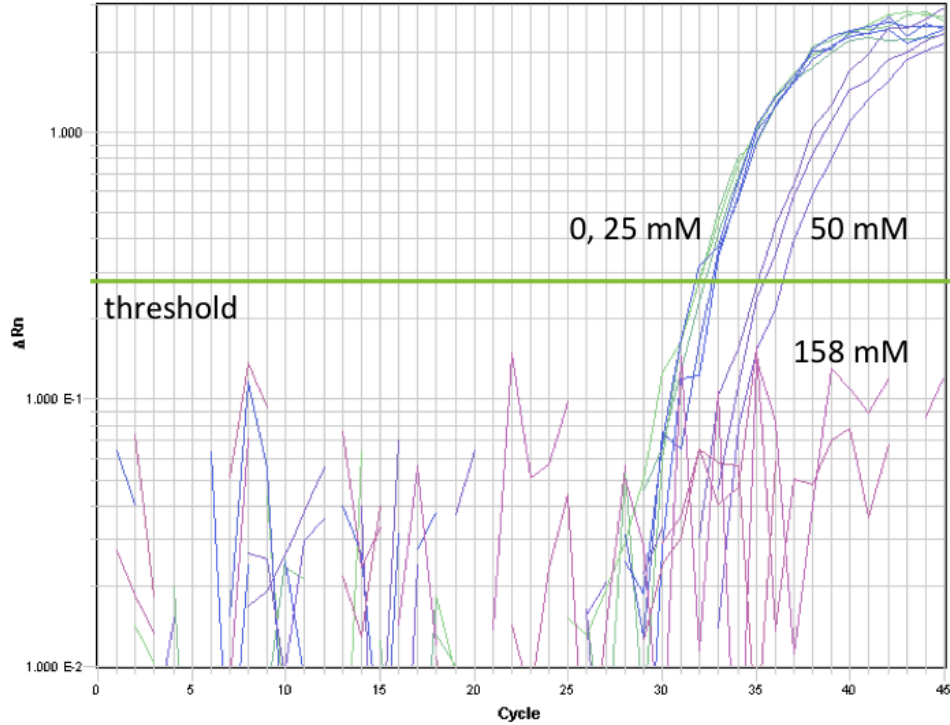


FIGURE 6.1: PCR inhibition by GuSCN. Blue: No GuSCN Control (NGC.)

6.1.2 GuSCN Concentration vs. Number of Washes

After selecting the model PCR inhibitor and determining the target purification power, the next step is estimating the number of on-chip washes needed to attain the target purification power. However, a method to measure the GuSCN concentration first needs to be established.

Correlate GuSCN Concentration with UV Absorbance

To evaluate the purification power achieved by on-chip washes, UV absorbance measurement is used to determine the GuSCN concentration. In particular, rather than a traditional spectrometer, a NanoDrop spectrometer is employed. The key difference between the two is sample volume. For the former, it is generally required to fill a 1 ml cuvette. In the latter case, a measurement is performed on a $1 \sim 2 \mu\text{l}$ droplet.

Since the purification stage of the fluidic device is designed to generate a few mi-

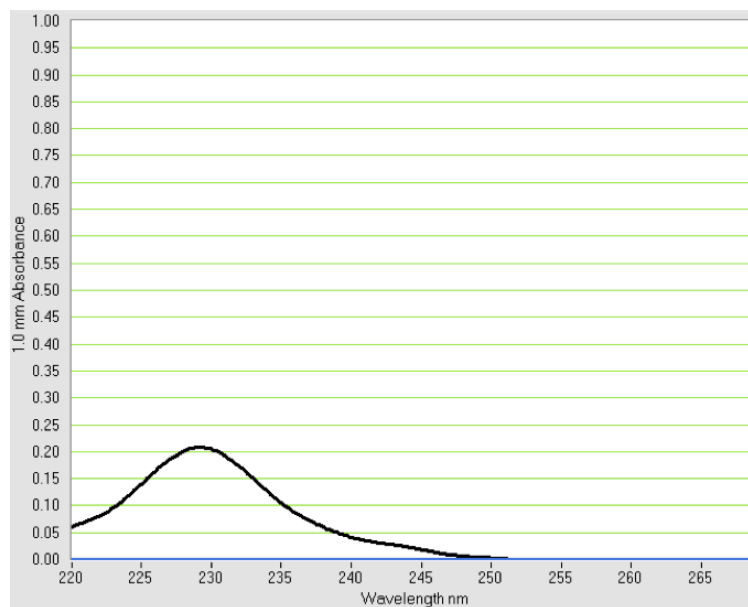


FIGURE 6.2: Absorbance spectrum of 1.5 mM GuSCN.

croliters of eluent, on a traditional spectrometer the eluent needs to be diluted by 500 \sim 1000 fold. With such dilution, GuSCN absorbance might become undetectable. In contrast, the absorbance of the eluent can be directly measured by NanoDrop without any dilution. Consequently, relative to cuvette-based spectrometers NanoDrop can obtain better GuSCN detection limit and dynamic range.

Shown in Fig. 6.2 is the absorbance spectrum of 1.5 mM GuSCN. Although the spectrum indicates that the absorbance peaks at approximately 230 nm, in Table 6.2 it can be seen that as GuSCN concentration increases the peak absorption wavelength is red-shifted. This behavior may be related to the shift of chemical equilibrium towards the left of Eq. 6.1, which in turn causes the apparent molar absorption coefficient at a given wavelength to become concentration dependent. This explanation is one of the reasons why the Beer-Lambert law is only valid at “low” concentrations.



Table 6.2: Peak absorption wavelength vs. GuSCN concentration.

GuSCN (mM)	Absorption peak (nm)
0.5	230
5	230
50	241
500	249
5000	262

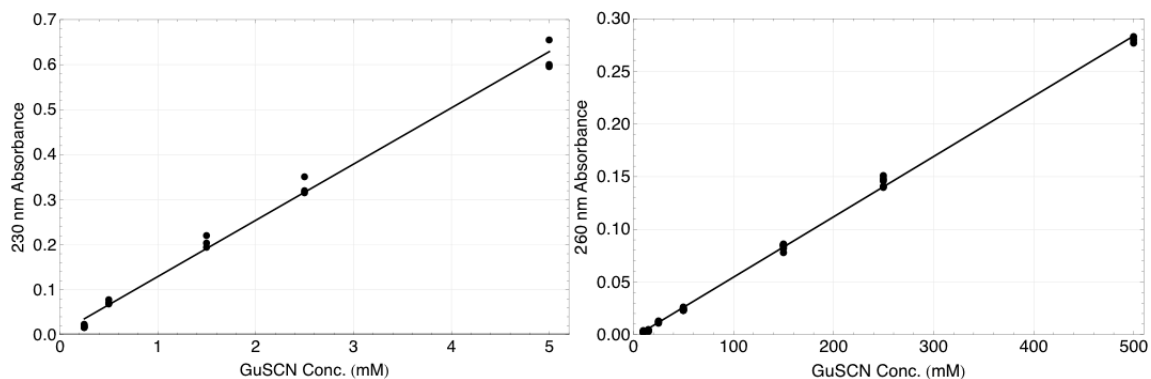


FIGURE 6.3: Absorbance - GuSCN standard curve for low and high concentration range (left and right, respectively.) Each concentration $n = 3$. Both plots $R^2 > 0.99$.

To overcome this issue, two standard curves are established: a low range curve that correlates 230 nm absorbance with GuSCN concentration 0.5 ~ 5 mM, and a high range curve that correlates 260 nm absorbance with GuSCN concentration 10 ~ 500 mM. The low and high range standard curve are shown in the left and right of Fig. 6.3, respectively.

GuSCN Concentration vs. Number of Washes

In the above paragraphs, GuSCN concentration is demonstrated to be correlated with the UV absorbance. Further, the GuSCN concentration in a microliter-sized droplet can be directly determined, without any dilution, by measuring its absorbance on a NanoDrop spectrometer.

This is a convenient technique that enables the quantitative comparison of the

model inhibitor concentration before and after an on-chip wash, i.e., purification power. Combined with the knowledge about how GuSCN affects qPCR (Table 6.1), at least in this simplified scenario it becomes possible to estimate the number of washes needed to obtain uninhibited on-chip qPCR.

Still, since absorbance is not chemical-specific, to use the method to monitor the GuSCN concentration after a wash it is necessary to ensure that GuSCN is the only UV absorber that changes its concentration between the washes. Because of this limitation, in the experiments discussed in Sec. 6.1.2 no nucleic acid is added to the input. Accordingly, the purification power result presented later in this section neglects any impact that may be incurred by the presence of nucleic acids, for instance by making the beads more difficult to disperse in a wash buffer. Thus, the purification power derived from this set of experiments should be considered as an overestimation.

Similarly, because the sodium azide in Wash Buffer 2 (WB2) of the miniMAG purification kit is a UV absorber, WB2 is unused. Instead, in addition to WB1 (the source of 5 M GuSCN) the on-chip purification process involves only Wash Buffer 3 and Elution Buffer. WB3, EB, and 5 cS silicone oil have been tested to show negligible UV absorbance.

With the purification protocol modified to be compatible with the measurement of GuSCN concentration, it is then proceeded to evaluate the effectiveness of on-chip IPF washes.

Briefly, as detailed in Appendix A.2, the experiment consists of three major steps. First, the magnetic beads suspended in WB1 are actuated by an external magnet either directly to EB (no wash) or to WB3 (1 ~ 2 washes.) Secondly, the beads along with the GuSCN carryover are brought into contact with EB. Third, with the magnet holding the beads in place, the eluent (i.e., EB contaminated with GuSCN) is aspirated from the device and subsequently analyzed on NanoDrop.

Following the outlined procedure, absorbance measurements indicate that after 0,

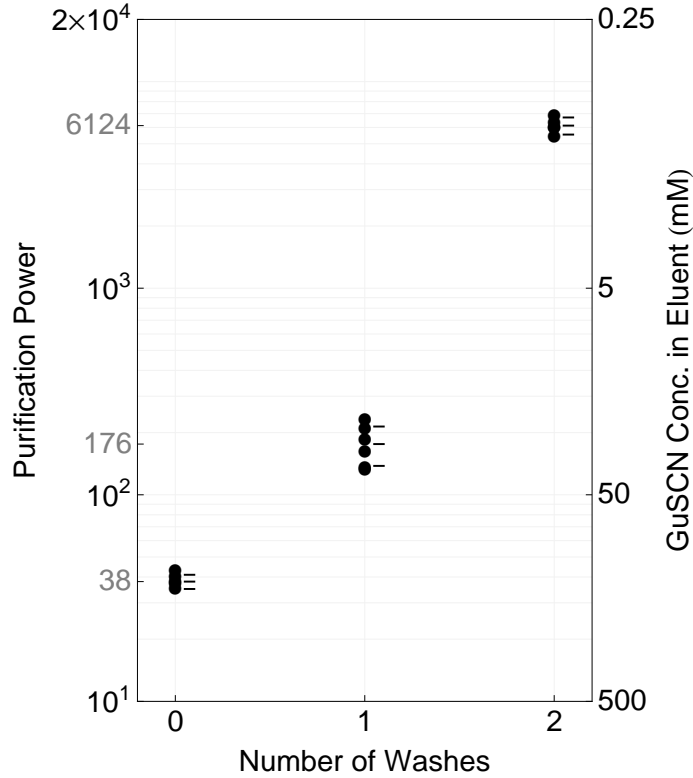


FIGURE 6.4: Purification power and GuSCN concentration in eluent vs. number of washes. Mean and 95% CI (t-distribution) calculated from $n = 5, 6, 5$ (0, 1, 2 washes, respectively) are labelled.

1, 2 washes the average GuSCN concentrations in the eluent are 131.6, 28.4, 0.8 mM, respectively. As plotted in Fig. 6.4, the concentrations correspond to purification power 38, 176, and 6124.

Among the results, there are three aspects that are particularly worth examining. First, the purification power of the no wash case will be discussed. Second, the effectiveness of each wash step is assessed. Third, with the addition of these data the number of washes needed to obtain uninhibited on-chip qPCR can now be estimated.

1. Purification power of the no wash case:

After on-chip washes, as part of the elution process GuSCN is further diluted by the elution buffer. Hence, even with no on-chip wash GuSCN is still lowered from

5 M to 131.6 mM.

Although it appears that dilution can be increased to eliminate the need for IPF washes, the approach is impractical for two reasons. First, with more dilution less extracted DNA can be packed into the droplets. In turn, the detection limit (in terms of *E. coli* per volume of sample, for instance) is impacted. Second, purification is not only dilution. For instance, when purifying nucleic acids from blood, the wash buffers are also responsible for digesting the proteins that might interfere with the downstream PCR.

2. Purification power gained by each wash step:

With one wash, the purification power obtained is 176, which results from 4.6×38 (1st wash \times dilution.)

With two washes, the purification power obtained is 6124, which results from $4.6 \times 35 \times 38$ (1st wash \times 2nd wash \times dilution.)

Interestingly, although both washes are performed with the same volume of WB3, the second wash is significantly more effective than the first ($PP_{2nd} = 35$, $PP_{1st} = 4.6$.) Still, it is unclear if a third wash would be able to provide a higher purification power than the second wash. This is because the absorbance method is limited to approximately 0.25 mM GuSCN. As a result, it is incapable of detecting the GuSCN in the eluent from a three-wash test.

In addition, it is important to note that even though the purification power gained from the second wash is similar to the purification power resulted from the dilution of inhibitors during elution ($PP_{2nd} = 35$, $PP_{elu} = 38$), as discussed in the previous bullet point the former does not penalize the nucleic acid concentration in eluent droplets, which in this approach is the factor that ultimately determines the overall detection limit.

3. Number of washes needed to obtain uninhibited on-chip qPCR:

In this section, two important results are presented. Initially, it is shown that GuSCN must be lowered from 5 M to less than 25 ~ 50 mM in order not to inhibit a downstream qPCR reaction. In other words, the purification power needed is at least 200.

Next, it is demonstrated that one- and two-wash purification respectively generate 176 and 6124 in purification power. On top of this purification power acquired from the purification process, on-chip PCR mixture preparation should further generate a purification power of 2. Consequently, the total purification powers are doubled to 352 and 12248.

(In Sec. 6.2.2, a 1x eluent droplet is merged with a 1x master mix/qPCR assay droplet to form a qPCR-ready 2x-volume droplet. Correspondingly, GuSCN is diluted by two fold. In an optimized implementation, however, the purification power gained from digital microfluidic PCR mixture preparation would be 3. This is because normally a PCR mixture should be assembled from three droplets: eluent, assay, and master mix.)

Combining the two data, the subsequent “purification then qPCR” full on-chip demonstration can be predicted to require only one wash. Still, it is essential to recall that the estimation might be somewhat optimistic. Because the experiment it is partially based on neglects the effects of nucleic acids on purification power. Therefore, it remains to be seen if the margin of purification power, 352 minus the needed 200, is sufficient to counter the inefficiency factors that have not been revealed by the investigations so far.

In contrast, two-wash purification seems likely to provide enough margin to safeguard against the above concern. Later on, these observations will be validated in Sec. 6.2.1 by varying the number of washes and then monitoring the changes

in the threshold cycle of on-chip qPCR.

6.2 Demonstration of IPF - DM Integration

In the previous section, it was estimated that one-wash purification would be sufficient for uninhibited PCR. This estimation will be tested in Sec. 6.2.1 by varying the number of washes and then observing the corresponding effect on the amplification curves generated by on-chip qPCR.

After confirming the needed number of IPF washes, the next step is to demonstrate the feasibility of the IPF - DM integration. This is achieved in Sec. 6.2.2 with an experiment that involves on-chip purification of the gDNA from the inhibitor solution, PCR mixture preparation via DM actuation, and the quantification of the retained Yb8 using on-chip qPCR. Further, by utilizing the copy number - threshold cycle relationship that will be detailed in Sec. 6.3, this experiment also reveals the percentage of the nucleic acid target that is retained throughout the workflow.

6.2.1 Threshold Cycle vs. Number of Washes

In Sec. 6.1, the PCR inhibiting concentration of GuSCN and the purification power gained by the IPF washes were determined. Also, by combining the two information, the number of washes needed to obtain uninhibited on-chip qPCR was estimated.

To recap, one wash was projected to be adequate. However, the estimation is partly based on the results from benchtop qPCR. Since on-chip qPCR is not yet optimized, compared with benchtop qPCR it may be less tolerant of GuSCN. Hence, in practice more purification power than the estimated value might be required.

The goal of this section, therefore, is to verify if one wash is indeed sufficient for on-chip qPCR. Later on, the number of washes confirmed to be necessary will be used in the “purification then qPCR” full on-chip demonstration in Sec. 6.2.2.

Summary of Experimental Method

To facilitate the discussion on the obtained results, the experimental method is summarized in the following paragraphs. A thorough description of the experimental method is provided in Appendix A.3.

To confirm if one wash is indeed sufficient, the number of washes is varied in order to observe its effect on the threshold cycle of on-chip qPCR. To this end, all other variables are fixed. For example, to ensure the purification power obtained here is in line with the previously measured values, in the purification stage the bead load, buffer volume, and wash procedure are identical to what were used in Sec. 6.1.2. Furthermore, the concentrations of reagents and the thermocycling profile are kept the same in all experiments.

Importantly, in addition to the above parameters, the amount of DNA in the PCR mixture also has to be consistent across the tests. This is because threshold cycle is a function of copy number and amplification efficiency. Accordingly, when monitoring the threshold cycle to detect the change in amplification efficiency (which is lowered by GuSCN), it is necessary to fix the copy number.

However, since each additional wash inevitably reduces the nucleic acid retention, if the experiment was started with DNA-bound beads the downstream qPCR would see the copy number and the amplification efficiency both varying. Then, the change in threshold cycle cannot be solely attributed to the GuSCN concentration in the PCR mixture. Therefore, instead of subjecting DNA-bound beads to a varying number of washes, the copy number here is fixed by adding the DNA directly to the master mix/qPCR assay solution. This method is viable because the DNA polymerase is inactive prior to the hot-start step of qPCR.

Other than the tests outlined above, there are two control experiments: no GuSCN control and no template control (NGC and NTC, respectively.) NGC pro-

vides a reference threshold cycle that is uninfluenced by GuSCN. In NGC, beads are not used. Instead, Elution Buffer is directly dispensed as the eluent droplet. On the other hand, the threshold cycle of NTC indicates the extent of background human DNA contamination. Therefore, in NTC no DNA is added to the master mix/qPCR assay solution. Also, similar to NGC, Elution Buffer is directly dispensed as the eluent droplet.

Ideally, at least three qPCR reactions (excluding replicates) should be concurrently performed on a fluidic device: NGC, NTC, and one for the wash test. This way, the robustness of each threshold cycle datum would be guaranteed by its accompanying on-chip positive and negative controls. However, despite the benefits, this experimental method was not adopted. This is because the current fluidic device and the fluorescence sensing strategy are somewhat ill-equipped to handle multiple concurrent qPCR reactions.

As a compromise, each control is run on a separate fluidic device. Also, NGC and NTC are always run when a new master mix/assay/DNA solution is prepared.

Lastly, it is worth noting that the presence of DNA on the beads may reduce the actual purification power to below the previously estimated value, for example by making the beads more difficult to disperse in a wash buffer. However, this influence is not straightforward to quantify, because the methodological limitation discussed on p. 112 prevents the purification power measurement and the on-chip qPCR from being performed simultaneously.

Result and Discussion

Following the experimental method outlined above, on-chip qPCR is performed with the eluent resulting from 0, 1, and 2 IPF washes. Along with the NGC and NTC, each of the five types of tests is replicated three times. The obtained amplification plot is shown in Fig. 6.5, and the threshold cycle data are tabulated in Table 6.3.

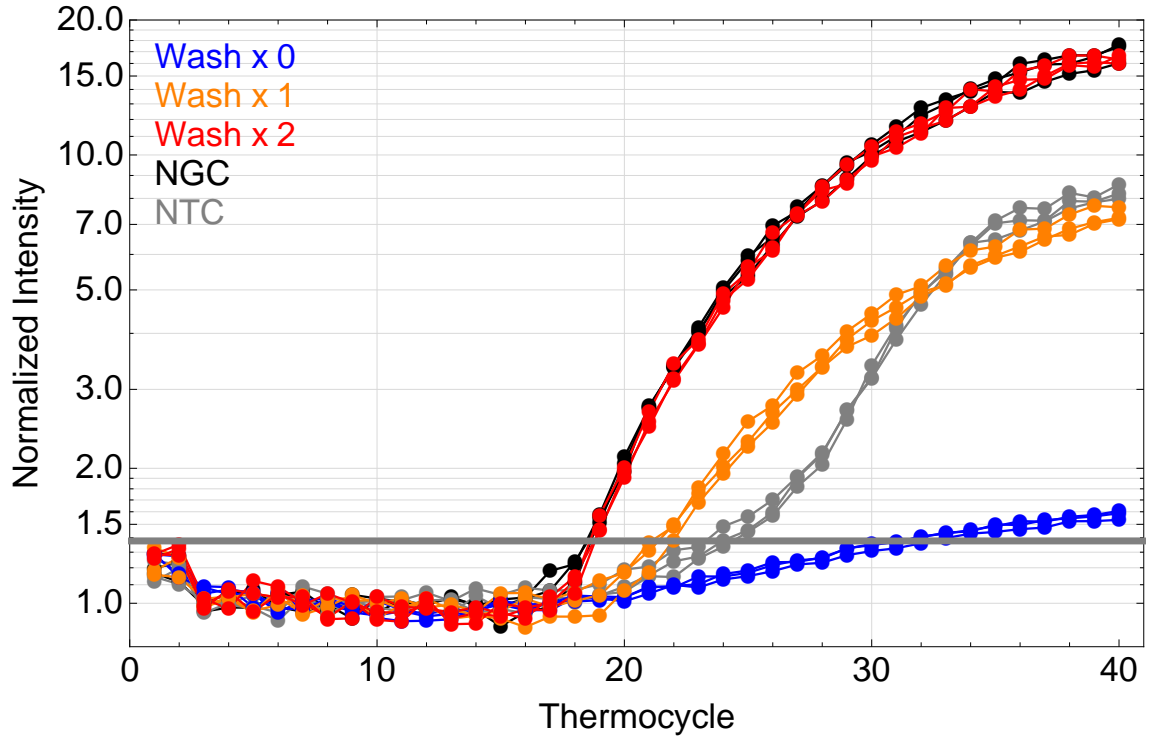


FIGURE 6.5: Threshold cycle vs. number of washes.

Table 6.3: Threshold cycle vs. number of washes.

Type	Average C_t	Note
Wash \times 0	-	No exponential phase.
Wash \times 1	22	C_t delayed by 3 cycles.
Wash \times 2	19	$C_t = \text{NGC}$.
No GuSCN Control	19	Reference C_t .
No Template Control	24	Background Yb8.

The following observations can be made from the amplification plot:

1. Two-wash purification

It produces effectively the same amplification curve as NGC. In other words, as estimated, two-wash purification is able to generate enough purification power to achieve uninhibited on-chip qPCR.

2. One-wash purification

Compared with NGC, its threshold cycle is delayed by 3 cycles.

Previously, one wash was predicted to provide sufficient purification power, albeit with a small margin over the needed value: 352 versus 200. However, the estimations done in Sec. 6.1.2 are based on the data gathered using benchtop qPCR, not on-chip qPCR. Therefore, the reason why one wash performed unsatisfactorily perhaps can be explained by the consequences of this difference.

First, on-chip qPCR might have a less-than-estimated tolerance for the inhibitors coming from the purification process. This follows since parts of the overall inhibitor tolerance could be consumed by the additional inhibitors introduced by the PCR stage of the fluidic device. Secondly, a lesser overall inhibitor tolerance itself is a likely consequence of the unoptimized on-chip qPCR. For instance, inaccurate temperature setpoints will exacerbate the degradation of DNA polymerases. In turn, even less DNA polymerases would be able to survive the denaturing effect of GuSCN.

Thus, as both effects push the demanded purification power to above 200, one wash quickly becomes inadequate. Meanwhile, two washes, with a purification power estimated at 12248, appear to have enough leeway to counter the two effects.

3. No purification

A very weak amplification was detected. Unlike the PCR behavior of other curves, this trace seems to skip the exponential phase and directly enter a plateau-like phase. Thus, although the generated fluorescence surpassed the threshold intensity, it did not occur when the reaction was in the exponential phase. As a result, this test did not yield any valid threshold cycle value.

4. No template control

Significant amplification is detected in NTC. The result was not unanticipated, because positive NTC was previously obtained on benchtop qPCR, as can be seen in Fig. 5.1.

Since the qPCR is intended to detect a 1852 copy/genome target in the human genome, positive NTC is somewhat unavoidable. Potential sources of the contamination include the reagents, assembling of the fluidic device, and the experiment setup process. In particular, the steps thought to contribute the most to the background are reagent loading and IPF purification, during which the reagents are exposed and in close proximity to the operator.

Currently, the floor of the dynamic range is not limited by the qPCR chemistry or the fluorescence sensor. Rather, it is determined by the high background human DNA contamination. Further discussions about the dynamic range can be found in Sec. 6.3.2.

In sum, to purify the DNA from 5 M GuSCN, one wash is found to result in a delayed threshold cycle, and two washes are in fact necessary for uninhibited qPCR.

Since each on-chip wash takes approximately twenty seconds, the extra wash does not significantly penalize the sample-to-answer time. Instead, the most affected aspects are the floor plan and footprint of the fluidic device, and perhaps more importantly, nucleic acid retention.

Also, one-wash purification's deviation from the estimation could be attributed to the on-chip qPCR having a less-than-estimated tolerance for the inhibitors inherited from the purification process. This may be due to the extra inhibitors introduced by the PCR stage taking up the inhibitor budget, and/or the overall inhibitor budget itself might become smaller because of the suboptimal on-chip qPCR. Either of the two mechanisms will compromise the amplification efficiency.

Hence, the amplification efficiency of on-chip qPCR will be measured in Sec. 6.3.1.

Its value would be useful for confirming the reasons why one-wash purification fails to lead to uninhibited qPCR.

6.2.2 Nucleic Acid Retention

The second IPF - DM experiment has two purposes. First, after confirming the needed number of IPF washes in Sec. 6.2.1, this experiment will fully demonstrate the feasibility of the proposed IPF - DM integration. To that end, all steps from the purification of gDNA from the inhibitor solution to the detection of the nucleic acid target by qPCR are performed on-chip.

Secondly, by combining the threshold cycle data from this experiment and the copy number - threshold cycle relationship that will be detailed in Sec. 6.3, the retention of the nucleic acid target throughout the workflow can be estimated. This parameter is important because a better retention corresponds to a higher probability of having more copies of the targets in an eluent droplet, thereby improving the detection limit.

Summary of Experimental Method

The experiment begins with the off-chip binding of the gDNA to the magnetic silica beads. In the case of 100% retention, the amount of the gDNA added to the Lysis/Binding Buffer would lead to 30x/8550 copies of Alu Yb8 in the final PCR mixture droplet. Next, as part of a suspension with Wash Buffer 1 (WB1), the beads are transferred via pipetting to the purification stage of the fluidic device. The amount of the beads loaded to the device is identical to what was used in the experiment in Sec. 6.2.1. Beyond this step, all procedures are on-chip.

At this point, the goal is to purify the gDNA from WB1, which is essentially a solution of 5 M GuSCN - a potent PCR inhibitor at high concentration. To attain the necessary degree of purification (that is, lower the GuSCN concentration in the

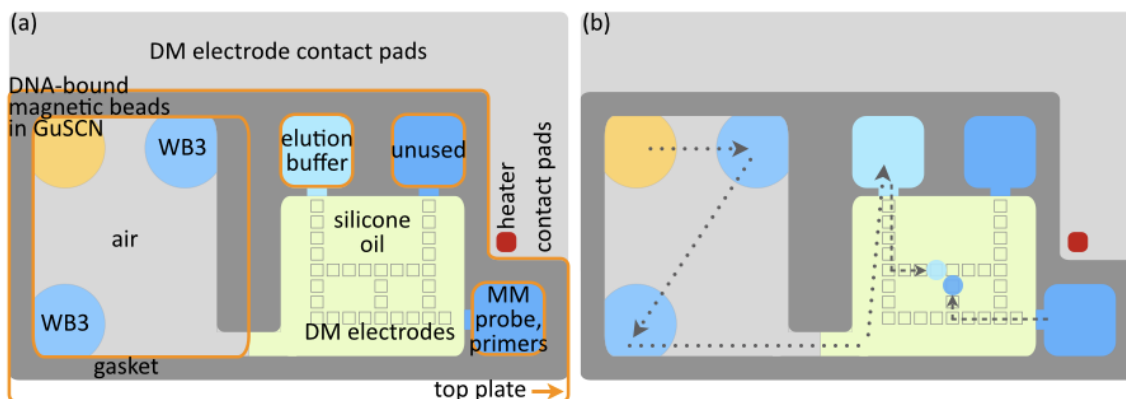


FIGURE 6.6: NA retention experiment: (a) floor plan and (b) workflow. Dotted line: During purification, DNA-bound beads are transported by an external magnet. Dashed line: Microdroplets are generated and then transported by DM actuation.

final PCR mixture to a level that can be tolerated by PCR), as suggested by the result in Sec. 6.2.1 two IPF washes in WB3 are performed. Afterwards, the beads are transported to the Elution Buffer reservoir (EB.) After a brief incubation, the gDNA is released from the beads. At the same time, the aqueous carryover that travels with the beads brings a certain amount of GuSCN to the EB. However, the inhibitor concentration becomes inconsequential after two IPF washes and two dilutions: with EB and later with the master mix/qPCR assay droplet.

Subsequently, an eluent droplet and a master mix/qPCR assay droplet are dispensed from their respective reservoir and then mixed together. The dispensing, transportation, and merging of the two microdroplets are achieved using digital microfluidic actuation. Finally, the auxiliary system is started to thermocycle the PCR mixture droplet and to monitor the resulting fluorescence.

Fig. 6.6 illustrates the movement of the magnetic beads during the purification process and the actuation of the two droplets during PCR mixture preparation. Additional details about the experimental method can be found in Appendix A.5.

Lastly, after summarizing the workflow, it is perhaps worth noting that the relatively high 30x copy number is used primarily because of the concern about the

ability to confidently discern the retained target from the background in the case of very low retention. Specifically, with a maximum starting concentration of 30x the present $0.06x \sim 30x$ dynamic range of the on-chip qPCR would correspond to $0.2\% \sim 100\%$ retention. Thus, even after provisioning for a ten-fold margin over the floor in order to confidently differentiate a low retention case from the Yb8 background, the range of nucleic acid retention that can be measured by the on-chip qPCR remains rather usable at $2\% \sim 100\%$. Furthermore, the other reason for using 30x is because Assumption 1 in Sec. 6.3.2 does not need to be invoked if the retention is within or close to $3.3\% \sim 100\%$.

Estimation of Nucleic Acid Retention

Following the outlined procedure, the obtained amplification plot is shown in Fig. 6.7. Compared with the amplification plot in Fig. 6.5, the spread among the three replicates in Fig. 6.7 appears to be relatively wide. The phenomenon perhaps can be explained by the different procedures that the gDNA needs to go through before qPCR. In the Fig. 6.5 case, the gDNA that contains the Yb8 target is premixed with the master mix and the qPCR assay, loaded to the reservoir, and then dispensed. As a result, the initial Yb8 copy number in the PCR mixture droplet should be relatively consistent. In contrast, the gDNA here needs to go through binding, washing, and elution in addition to droplet dispensing. Because these steps are not yet automated, they are likely to introduce variations to the initial Yb8 copy number, and thus affecting the amplification curves.

Via the copy number - threshold cycle relationship given in Eq. 6.4, the threshold cycles in Fig. 6.7 correspond to an average nucleic acid retention of 36%. As the experiment is structured, the obtained estimation on the retention encompasses all of the losses occurred throughout the workflow from off-chip binding to on-chip PCR mixture preparation. The major factors that are suspected to be responsible for

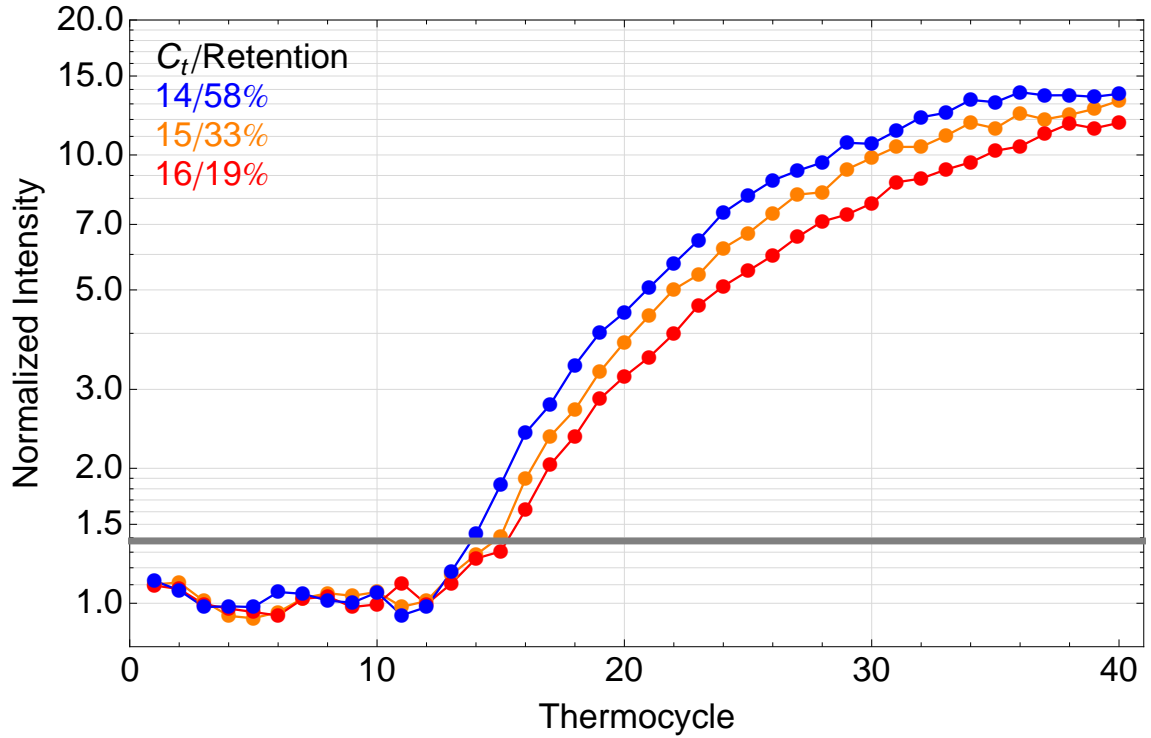


FIGURE 6.7: Threshold cycle vs. nucleic acid retention.

lowering the nucleic acid retention are itemized below:

- Binding
 - Not all added gDNA are captured by the magnetic silica beads.
- Purification
 - Some analytes are left in WB1 and WB3 and thus not transported to the Elution Buffer reservoir. For example, when the beads are snapped away from WB3 after an IPF wash, a somewhat small portion of the beads is observed to remain trapped in WB3.
 - DNA detach from the beads during an IPF wash.
 - During elution, the release of the DNA from the beads to EB is incomplete.
- PCR mixture preparation

- An eluent droplet may have a different nucleic acid concentration than the eluent in the reservoir.
- Nucleic acids might adhere to the surfaces of the fluidic device, for instance when transporting the eluent droplet to the location designated for the subsequent thermocycling.

Challenges in Achieving Effective Elution

In particular, optimal retention greatly depends on effective elution. Yet, because elution is the step that bridges IPF nucleic acid purification with DM PCR mixture preparation, the optimization of the elution protocol and the EB reservoir is challenging due to the sometimes conflicting requirements. For instance:

- EB volume
 - Less improves the detection limit, more improves elution/retention.
 - The proposed approach calls for eluting to a small volume of EB to improve the probability of having at least one copy of the target in the eluent droplets. On the downside, the preference of nucleic acids to unbind from the silica during elution to certain extent decreases with an increasing nucleic acid concentration in the eluent.
- Bead volume (pertaining to the current range of EB volume)
 - Less improves retention by facilitating mixing during elution, more improves retention in a different way by enhancing the capture of targets.
 - Elution is promoted by having an adequate degree of mixing between the beads and the EB. However, mixing is difficult in the current implementation because during elution the beads would take up a substantial volume of the EB reservoir. Although the issue could be addressed by employing

less beads, this solution limits the ability to use more beads to improve the probability of capturing the targets and to adjust the binding capacity.

In addition to what are outlined above, elution efficiency is also influenced by temperature. In the present protocol, elution is conducted at room temperature, rather than the 60 °C generally recommended for eluting to a small volume of EB. This circumvents the problem of excessive EB evaporation due to the exposed reservoir (i.e., not sealed by the top plate, refer to Fig. 5.5) but sacrifices the elution efficiency and hence, nucleic acid retention.

Lastly, independent of the experiment described in this section, a previous attempt at characterizing the retention of 160 bp DNA indicates that the loss due to elution is 3.4x relative to the loss due to IPF washes (Table 6.4.) Although the exact ratio might not be directly applicable to the experiment here, it nonetheless suggests that the optimization of elution should be a top priority in the effort to improve the retention.

Table 6.4: Loss of nucleic acid retention due to unoptimized on-chip processes. The steps labelled with “b” are performed off-chip according to vendor-supplied protocols.

Bind	Wash	Elute	qPCR	Relative NA retention
b	b	b	b	1
b	on-chip	b	b	0.88
b	on-chip	on-chip	b	0.47

Demonstration of Feasibility

The overall goal of this work is to demonstrate the feasibility of integrating IPF nucleic acid purification with DM PCR mixture preparation. Such integration is important in the context of speeding up the common “lyse, purify, quantify” workflow because both IPF and DM are inherently amenable to automation.

Previously, this integration is partially showcased in Sec. 6.2.1 with the “empty” beads went through a different number of IPF washes and the gDNA essentially directly added to the PCR mixture droplet. To assess the number of washes needed to attain uninhibited qPCR, the fixed initial Yb8 copy number ensured that the on-chip qPCR is only influenced by the GuSCN concentration.

In contrast, in the experiment discussed in this section, the gDNA is purified from the inhibitor using IPF washes, and then Yb8 in the gDNA is quantified by thermocycling the PCR mixture droplet prepared using DM actuation. While the protocols and the fluidic device are shown to have room for improvements, the successful amplifications nevertheless fully uphold the viability of the proposed integration.

Finally, it should be stressed that although the demonstration is basic, the potentials unlocked by the integration of IPF and DM should not be overlooked. For instance, lysis and binding implementations already known to be compatible with IPF purification could be incorporated [35]. Such a system would allow the operator to walk away after reagent loading. Another possibility is to replace (or augment) qPCR with other potentially faster multiplex sequence detection methods, such as the amplification-free, microarray-based approach commercialized by Nanosphere, Inc. [67].

6.3 Performance of On-Chip qPCR

In this section the focus is shifted to gaining a basic understanding about the present performance of on-chip qPCR, e.g., the amplification efficiency, the level of background contamination, and the dynamic range of Alu Yb8 quantification. In particular, the suboptimal amplification efficiency and the deviation from the predicted number of IPF washes in Sec. 6.2.1 might be attributed to the same causes. Additionally, the implicit assumptions when using the current data for quantification

purposes are clarified.

6.3.1 Amplification Efficiency

The focus of this section is to determine the amplification efficiency of on-chip qPCR. At this stage, knowing the amplification efficiency is useful for three reasons. First, it indicates how well a qPCR reaction is optimized. Second, it is helpful in understanding why one-wash purification does not comply with the purification power estimation (Sec. 6.2.1.) Third, it is part of the data that correlates the threshold cycle with the Alu Yb8 copy number (Sec. 6.3.2.)

As a brief overview, amplification efficiency is defined as:

$$C_n = C_i(1 + E)^n \quad (6.2)$$

(C_i , C_n : initial copy number and copy number at cycle n , E : amplification efficiency.)

According to the equation, low efficiency reduces the quantity of amplicons generated per thermocycle. In turn, more thermocycles would be needed to reach the threshold fluorescence intensity, resulting in a delayed threshold cycle.

However, in general amplification efficiency is not directly calculated from the above equation, since this would require an independent method to measure C_n . Rather, in practice it is determined from the slope of the threshold cycle - initial copy number standard curve.

To determine the amplification efficiency, on-chip qPCR is initiated after an Elution Buffer droplet is mixed with a master mix/assay/gDNA droplet. Three final DNA concentrations are tested: 0x, 1x, and 30x (refer to Appendix A.4 for details.) For each concentration there are three replicates. In reality, only the 30x experiment needs to be run. This is because the 0x and the 1x conditions are identical to the No Template Control and the No GuSCN Control in Sec. 6.2.1, respectively.

In particular, since the goal is to evaluate the on-chip qPCR, on-chip purification

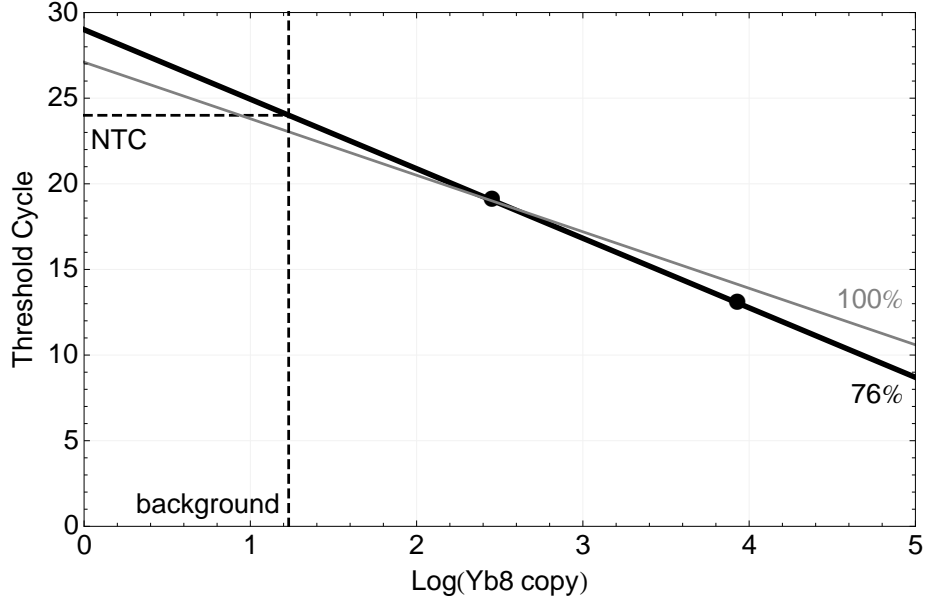


FIGURE 6.8: On-chip qPCR amplification efficiency and Yb8 background.

is not involved. Still, for comparison purposes the on-chip qPCR here is configured in the same way as Sec. 6.2.1. Because of this reason, the DNA is premixed with the master mix/assay solution, instead of dissolved in the Elution Buffer by itself.

Following the procedure described above, the obtained threshold cycle - initial copy number data is plotted in Fig. 6.8.

It can be seen that relative to a hypothetical case with 100% amplification efficiency (gray line), on-chip qPCR (black solid line) generates a lower threshold cycle when the starting copy number is high, and it generates a higher threshold cycle when the starting copy number is low. This behavior is a symptom of low amplification efficiency. The actual efficiency value can be calculated from the slope of the solid line:

$$10^{-1/slope} - 1 = 10^{-1/-4.06} - 1 = 76\% \quad (6.3)$$

That is, on average 1.76 amplicons are generated per template per thermocycle, rather than the theoretical value of 2. Although the difference seems to be small, relative to a 100% efficient amplification there will be 98% less amplicons after 30

thermocycles.

Since 90% \sim 110% is considered to be typical, the low efficiency suggests that on-chip qPCR remains to be further fine-tuned. (As a comparison, 81% is obtained on the benchtop qPCR, see Sec. 5.1.1.) Moreover, the two reasons previously hypothesized in Sec. 6.2.1 to explain why one-wash purification failed to lead to uninhibited on-chip qPCR can also explain the potential causes of the low amplification efficiency.

Firstly, the low efficiency could be due to the PCR stage introducing its own PCR inhibitors. These additional inhibitors are not considered in the purification power estimation, but along with the GuSCN inherited from the purification process the total amount of inhibitors in a PCR mixture droplet becomes enough to partially impede the amplification.

Second, the low efficiency seen here might be a result of a substandard thermocycling profile. As an example, if the denaturation step is slightly too long or too hot (since there is a difference between the setpoints and the temperature experienced by a PCR mixture droplet), the degradation of the DNA polymerase will be greatly accelerated. This not only directly affects the amplification efficiency, it also facilitates the inhibitors' effort to inactivate or denature the DNA polymerase. Accordingly, the inhibitor tolerance would appear to be weaker.

Notice that the first explanation relates only to the consequences of on-chip processes, whereas the root of the second mechanism originates from factors that are off-chip, e.g., the duration and the temperature setpoint of the denaturation step.

Independent of the two factors that are discussed above, amplification efficiency is also influenced by the composition of the reaction mixture. For instance, the master mix and the assay occupy 50% and 5% of the volume of the reaction mixture prepared according to the standard protocol. In contrast, due to the dilution incurred by the merging of two droplets, in the reaction mixture prepared on-chip the percentages and hence the concentrations of the associated reagents (e.g., DNA polymerase,

dNTPs, primers, probe) are halved. Therefore, the more diluted reagents could be one of the reasons for the low on-chip amplification efficiency. Fundamentally, this issue is perhaps best addressed by increasing the concentrations of the chemicals in the stock solutions. This is feasible for the assay since it is shipped from the vendor in a lyophilized form. However, it might require switching away from off-the-shelf master mixes.

Still, amplification efficiency alone cannot pinpoint the primary cause of a sub-optimal qPCR. Rather, low efficiency merely indicates the presence of issues in the qPCR chemistry, the thermocycling profile, or both. To improve the efficiency, however, there are many variables between the two that need to be systematically examined.

Lastly, it should be noted that in a rigorous investigation of amplification efficiency, the range of template concentration tested should span at least five logs, and each concentration should have at minimum three replicates. This is recommended because in Eq. 6.3 a small change in the slope will greatly affect the corresponding amplification efficiency. However, this level of stringency was not targeted herein, because the priorities of the fluidic device development are placed on demonstrating the feasibility of the proposed approach and qualitatively understanding the principal challenges of implementing the fluidic device and the auxiliary system. For the same reason, it was opted not to further venture into the investigation of the amplification efficiency when on-chip purification and on-chip qPCR are both involved, as this will (among other things) require the binding capacity of the magnetic silica beads to be first characterized. This obstacle will be further discussed on p. 136.

In sum, in this section the amplification efficiency of on-chip qPCR is estimated to be 76%. As a comparison, 81% is obtained on the benchtop qPCR, and 90% ~ 110% is considered to be the ideal range. Furthermore, the likely culprits of the low amplification efficiency can also explain the inability of one-wash purification to

lead to uninhibited on-chip qPCR. By implication, one wash may become sufficient if the on-chip amplification efficiency can be improved to the benchtop level. Finally, the low amplification efficiency could be due to issues with the qPCR chemistry, the thermocycling profile, or a combination of both. To better pinpoint its cause, in retrospect it is necessary to vary the number of on-chip washes and then check the resulting threshold cycle on benchtop qPCR. This way, the estimation of purification power can be verified independent of the on-chip qPCR.

6.3.2 Limitations of Nucleic Acid Quantification

In the previous section, the threshold cycle - initial copy number relationship was established. Other than using its slope to estimate the on-chip amplification efficiency, the standard curve can also be used to derive the copy number from an obtained threshold cycle. This method was employed in Sec. 6.2.2 to determine the retention of the nucleic acid target throughout the workflow. This section, however, will come back to clarify the assumptions and the limitations when the results gathered so far are being used for copy number quantification purposes.

Assumptions

To recap, the standard curve obtained in Sec. 6.3.1 is:

$$C_t = 29 - 4.06 \times \log(\text{Yb8 copy}) \quad (6.4)$$

In Sec. 6.2.2, the standard curve was used to quantify the nucleic acid targets that are retained throughout the workflow and then detected by the on-chip qPCR, i.e., nucleic acid retention (see Method C below.) However, because the characterization of amplification efficiency is preliminary, the use of Eq. 6.4 requires the following assumptions to be in place:

1. In Method B, the amplification efficiency is constant for copy numbers up to 30x in the PCR mixture droplet.

2. Method B and C have the same amplification efficiency.

For the ease of comparison, Experimental Method B, C are summarized below:

- Method B: Used in Sec. 6.3.1 to characterize the on-chip amplification efficiency.

Droplet 1: Master mix, assay, gDNA – 1x (B1), 30x (B2), 0x (B3).

Droplet 2: Elution Buffer.

- Method C: Used in Sec. 6.2.2 to characterize the nucleic acid retention.

Droplet 1: Master mix, assay.

Droplet 2: Beads with gDNA suspended in GuSCN → 2 IPF washes → elution → dispense eluent as Droplet 2 ($30x \times \text{retention}\%$).

- “1x” refers to 285 copies of Alu Yb8. 1x in the PCR mixture is equivalent to 3.1 copy/nl.

In both cases, Droplet 1 and Droplet 2 are merged to form the reaction mixture, and then the thermocycling is started. (Further details of the experimental methods are supplied in Appendix A.4 and A.5.)

Next, the two assumptions are explained and justified.

– Assumption 1

Recall that the amplification efficiency was derived from the threshold cycles of on-chip qPCR experiments with 1x and 30x starting template concentrations. While no subsequent tests employ concentrations higher than 30x, later discussions assume the same 76% amplification efficiency for initial template concentrations lower than 1x. The extrapolation to initial concentrations higher than what are involved in the standard curve is likely to become problematic approaching 10^3x , because PCR can be impeded by template overload, e.g., > 100 ng for a 20 μ l reaction using the ABI Fast Advanced Master Mix. In contrast, no similar issue will

affect the extrapolation to lower template concentrations. Thus, this assumption is perhaps not unreasonable.

– Assumption 2

Method C is used in Sec. 6.2.2 in the assessment of analyte retention. In Method C, the gDNA is purified from GuSCN via IPF washes, eluted from magnetic beads, packed into a microdrop, mixed with qPCR reagents via DM actuation, and then finally thermocycled.

Essentially, this assumption anticipates that after the two IPF washes in Method C, the resulting PCR mixture droplet would be sufficiently clear of GuSCN (as in Method B), and the subsequent on-chip qPCR would not be inhibited.

The assumption is considered to be sensible because of two previously gathered results. First, it is shown in Sec. 6.2.1 that after two IPF washes, the amount of GuSCN brought by the (DNA-less) magnetic beads to the Elution Buffer and in turn to the PCR mixture droplet is insufficient to impede the on-chip qPCR. Second, two-wash purification is shown in Sec. 6.1.2 to generate significantly more purification power than what is needed to attain uninhibited qPCR: 12248 versus 200. On the other hand, it is known that under Method C conditions the obtained purification power is decreased, while the required purification power is increased. Nevertheless, given the considerable excess purification power that could be afforded by two-wash purification, it seems plausible for it to remain adequate under Method C conditions.

In particular, Assumption 2 is related to the amplification efficiency when on-chip purification and on-chip qPCR are both involved. In a thorough 5-log evaluation,

the highest initial copy number that needs to be tested will approach

$$\begin{aligned} & \text{background} \times \text{margin over background} \times \text{max of } 10^{0\sim 4} \\ & = 17 \times 10 \times 10^4 = 1.7 \times 10^6 \text{ copies } (= 6 \times 10^3 \times) \end{aligned} \quad (6.5)$$

According to the Eq. 6.4 standard curve, this corresponds to an impractical threshold cycle of 4. Furthermore, this copy number might require significantly more magnetic beads than what can be accommodated on the current fluidic device. Because of these obstacles, this amplification efficiency is challenging to measure at the moment.

After the discussion about the two assumptions, it should be understood that they are put in place to temporarily plug the gaps in the existing data. In this function, they enable the calculations of a few performance indicators later in this section that will allow one to gain some basic knowledge about the approximate performance of the current system, and more importantly, to identify the issues that should be addressed with priority in subsequent efforts. Invoking these assumptions is not ideal. Still, since this work is structured to demonstrate the viability of a new approach rather than characterize a mature qPCR instrument, it is perhaps permissible providing that the derived results are analyzed with the two assumptions in mind.

Yb8 Background

With the assumptions in place and the reasonings behind them clarified, it is now appropriate to initiate a quantitative discussion about the performance of the current on-chip qPCR.

First, the background Alu Yb8 level can be determined by using the Eq. 6.4 calibration curve to estimate the Yb8 copy number that corresponds to the threshold cycle of the No Template Control in Sec. 6.2.1:

$$\begin{aligned} 23 &= 29 - 4.06 \log Yb8_{\text{chip}} \\ Yb8_{\text{chip}} &= 17 \text{ copies (per } 46 \times 2 \text{ nl PCR)} \rightarrow 184 \text{ copy}/\mu\text{l} \end{aligned} \quad (6.6)$$

As a comparison, on the benchtop qPCR the No Template Control shows:

$$33.9 = 40.5 - 3.88 \log Yb8_{\text{bench}}$$
$$Yb8_{\text{bench}} = 50 \text{ copies (per } 20 \mu\text{l PCR)} \rightarrow 2.5 \text{ copy}/\mu\text{l} \quad (6.7)$$

These values include only the contamination incurred by the experiment setup process, PCR mixture preparation, and thermocycling. In other words, they do not include the contamination introduced during nucleic acid purification.

In the case of benchtop qPCR, because the well plate is sealed by an optical adhesive film, during thermocycling the PCR mixture is protected from further contamination. Thus, the primary source of contamination is the manual PCR mixture preparation process.

In contrast, because the reservoirs on the fluidic device are exposed, human DNA that falls into a reservoir during the experiment setup procedure could be subsequently packed into the dispensed droplets during on-chip PCR mixture preparation. In particular, certain steps in the experiment setup procedure, such as thermocouple attachment, reagent loading, and optical fiber alignment to the PCR mixture droplet, require the operator to be in close proximity with the reagents and the fluidic device. Hence, these steps might considerably exacerbate the extent of the contamination.

Furthermore, as shown in Fig. 6.9, dust particles have been observed to enter the fluidic device through a reservoir and then contact a dispensed droplet during thermocycling. Accordingly, unlike the sealed wall plate in the case of benchtop qPCR, a PCR mixture droplet may be further polluted during thermocycling, even when the droplet is surrounded by the silicone oil medium and has been actuated away from the potential conduits of nucleic acid contaminants, i.e., the reservoir openings and the pipette ports. Due to the duration of qPCR, a significant amount of undesired Yb8 could enter the fluidic device during this period.

As can be expected from the difference in their susceptibility to contamination,

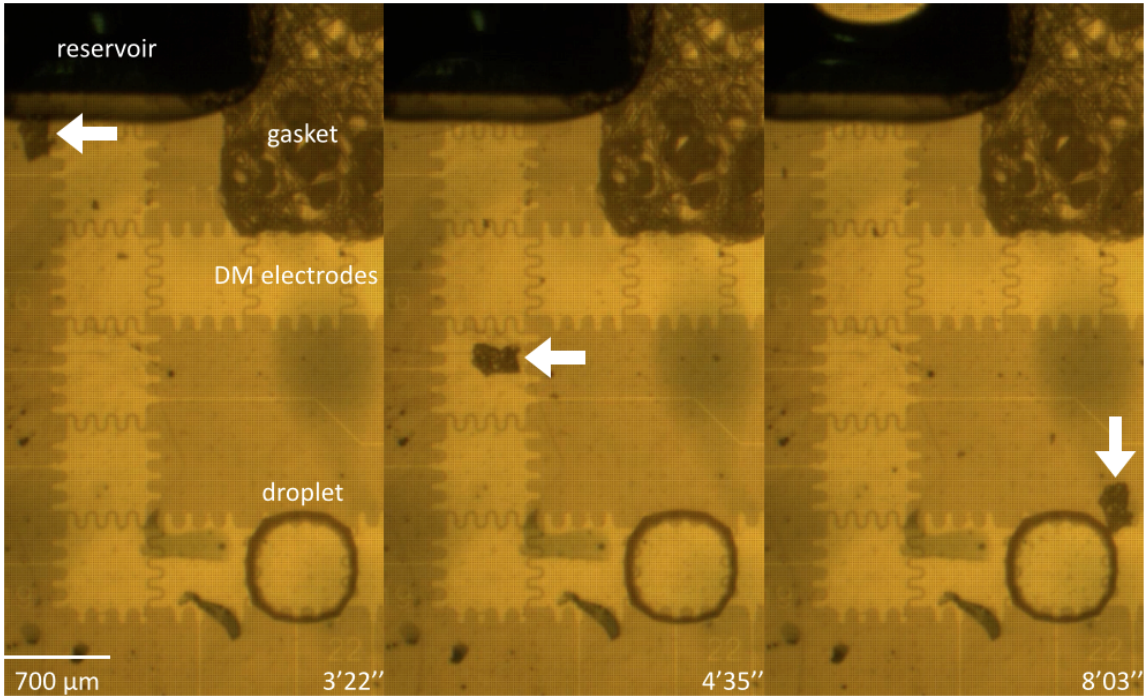


FIGURE 6.9: In this sequence of micrographs, a dust particle can be seen to enter the fluidic device from the reservoir and then contact the microdrop during thermo-cycling.

in terms of the Yb8 concentration in the final PCR mixture shown in Eq. 6.6 and 6.7, on-chip qPCR indeed has a 74x higher background than benchtop qPCR. On top of this background, additional Yb8 contamination can also be introduced during on-chip nucleic acid purification. For instance, since the purification stage of the fluidic device is also exposed to the operator, unintended sources of Yb8 can be captured by the magnetic silica beads during the IPF washes and then detected by the downstream on-chip qPCR. Still, because of the short duration, the amount of contaminating Yb8 that can be inflicted during the purification process is perhaps relatively limited.

Off-the-shelf qPCR instruments typically have a detection limit that approaches sub-ten copies. In comparison, the Yb8 background here is three to five times higher. The high background would be difficult to eradicate or mitigate, however. Recall that

the Alu Yb8 target was chosen because HeLa cells and HeLa gDNA are commercially available. Also, a target with a very high copy/genome ratio was intentionally selected in order to ensure that the demonstration of integrated on-chip purification and qPCR would not be stalled by substandard lysis or low nucleic acid retention. On the other hand, the tradeoff is that an elevated Yb8 background can be caused by, for example, a seemingly trivial number of human cells inadvertently fall into the Elution Buffer. In fact, at the concentration given by Eq. 6.6, the current background is equivalent to having only 0.2 somatic human cell in a 2 μ l reservoir. Due to this tradeoff, the detection limit is currently constrained by the high background and not by the qPCR chemistry.

Dynamic Range

The current dynamic range of on-chip qPCR, based on the available data and the associated assumptions, will be briefly discussed in the following paragraphs and then compared with that of a typical qPCR reaction. The purpose of this discussion is to gain a basic understanding about the current state of the on-chip qPCR and accordingly, identify what need to be improved in future implementations.

The floor of the dynamic range in this case is determined by the threshold cycle of the No Template Control, i.e., the background human DNA contamination. On the other hand, one of the factors that limits the ceiling of the dynamic range is the inhibition of PCR by overly concentrated nucleic acids. However, without making additional assumptions about the amplification efficiency at higher Yb8 concentrations, the ceiling in this case is constrained by the highest tested concentration.

Following the above discussion, the dynamic range is approximately 5×10^2 , which ranges from $17 \sim 8.6 \times 10^3$ initial copies in the 92 nl PCR mixture droplet. From another point of view, after factoring in the 36% retention of DNA (from off-chip binding to on-chip purification and qPCR, as determined in Sec. 6.2.2), prior to the

binding step this range would correspond to $2.1 \times 10^3 \sim 1.0 \times 10^6$ copies per ml of Lysis/Binding Buffer. In turn, 2.1×10^3 copies of Yb8 could be extracted from 0.6 somatic human cells, or in the case of a single copy per genome target amplifying at the same efficiency, 1.0×10^3 cells.

In contrast, most qPCR reactions feature a dynamic range of $10^{5\sim7}$, which ranges from $10 \sim 10^{6\sim8}$ copies in a $10 \sim 25 \mu\text{l}$ reaction volume. Hence, the dynamic range of on-chip qPCR at present lags by at least 200 folds. Fundamentally, this is a direct consequence of the low amplification efficiency.

Furthermore, a potential concern that is related to the dynamic range can be uncovered by switching the point of view from the initial copy number of the target to the initial total gDNA concentration.

Specifically, using the aforementioned values as an example, 8.6×10^3 copies of Yb8 is part of the 14 pg gDNA. In a 92 nl PCR mixture, this equates to 0.2 ng/ μl . Yet, for a 1 copy/genome target, the same number of copies has to come from 26 ng gDNA, which corresponds to 3 and 279 ng/ μl for 10 μl and 92 nl PCR reactions, respectively. The latter concentration is substantially higher than the maximum 10 ng/ μl recommended by the employed master mix. As a result, when the current system is used to detect a single copy target, the ceiling of the dynamic range may be further compressed by the total DNA loading in the PCR mixture.

6.4 Chapter Summary

Chapter 6 begins by determining the PCR inhibiting concentration of GuSCN. This is done by gradually increasing the amount of GuSCN added to the reaction mixture and then observing the resulting variation of the threshold cycle. It is found that GuSCN must be lowered from 5 M to less than 25 \sim 50 mM. In other words, the purification power needed is at least 200.

Then, the purification power gained by the IPF washes is measured. This is achieved by correlating GuSCN concentration with the UV absorbance of the eluent generated by the purification stage of the fluidic device. After factoring in the purification power resulting from the preparation of the PCR mixture droplet, it is estimated that one- and two-wash purifications generate 352 and 12248 in purification power, respectively.

Although based on the above purification power estimations it was predicted that one wash would suffice, on-chip qPCR reveals that in fact two IPF washes are needed. This may be due to the extra inhibitors introduced by the PCR stage taking up the inhibitor budget, and/or the overall inhibitor budget itself might become smaller because of the suboptimal thermocycling profile. Either of the two mechanisms will compromise the amplification efficiency.

Later, in the characterization of on-chip qPCR the amplification efficiency is found to be 76%. The value is indeed lower than the 81% obtained with the bench-top qPCR instrument and the 90% \sim 110% range that is typically considered to be optimal, thereby supporting the aforementioned explanations. Additionally, the dynamic range of on-chip qPCR is shown to be approximately $17 \sim 8.6 \times 10^3$ copies of Yb8 in a 92 nl PCR mixture droplet.

Finally, the average percentage of the nucleic acid target that is retained throughout the workflow is 36%. The experiment involves off-chip binding, on-chip purification of the gDNA from the inhibitor solution, PCR mixture preparation via DM actuation, and the quantification of the retained Yb8 using on-chip qPCR. Therefore, the experiment fully demonstrated the feasibility of the proposed IPF - DM integration.

Future Work and Conclusions

7.1 Future Work

After demonstrating the feasibility of IPF - DM integration, there are several implementation issues that remain to be addressed before more sophisticated experiments can be reliably conducted.

For instance, due to accessibility reasons, the polymeric materials currently used on the fluidic device have temperature tolerances comparable to or lower than 95 °C, i.e., Parylene C and the cast acrylic top plate. However, in subsequent revisions these materials must be replaced with materials that have the appropriate ratings, e.g., Parylene HT and a glass top plate. Further, all materials should be checked for the tendency to emit PCR inhibitors under thermocycling conditions.

Another area in need of a major revamping is the thermal aspect of the implementation. For example, the correlation between the temperature experienced by the PCR mixture droplet and the temperature sensed by the thermocouple during a thermocycle is not well characterized. Also, the position of the on-chip heater did not take into account the heat sinking of the aluminum device holder. These issues

in turn exacerbate the difficulty of finding a suitable set of PID parameters. Ultimately, to fully optimize the thermal behavior of the system, a predictive thermal model needs to be established, and thermal imaging would be an indispensable tool in the development of the model.

In addition, two topics that are unexplored in this work will be discussed below. First, enhancing the bead - buffer mixing is essential for improving the detection limit. Second, the possibility of combining IPF with other sequence detection methods would be considered.

Mixing Enhancement

Thorough mixing of NA-bound beads with the buffers is essential to effective washing and elution. Yet, all but one [35] of the surveyed publications on IPF conduct washes and elution when the beads are pelletized. This approach seems to be suboptimal, because the beads buried inside an agglomerate are only exposed to a limited flux of reactants [68]. From the integration point of view, ideally a magnetic field gradient created by on-chip coils [38] or serpentine [69] can be modulated to propel the beads off the substrate to promote mixing. Still, while such structures can be incorporated into the bottom plate of the fluidic device, the added fabrication complexity might be somewhat undesirable.

Instead, as a way to unpack the pellet and agitate the beads without additional moving parts, an ultrasonic transducer could be positioned at a location deemed to be effective by finite element modeling. However, low intensity is required to avoid NA shearing and polymerase denaturation, e.g., 1 W/cm² [70]. As an alternative, an extra linear actuator mounted with magnets can be placed on top of the fluidic device. To agitate the beads, the magnetic field can be manipulated by varying the relative position of the magnets [35]. Ultimately, improved bead - buffer mixing would lead to refined purification power and detection limit.

Alternative Sequence Detection Method

Although qPCR is one of the most mature sequence detection methods, the direct detection techniques (i.e., amplification-free) in principle could have the advantage in assay time and system complexity. This is because qPCR is typically time-consuming and requires sophisticated temperature control and fluorescence sensing systems. Another issue of qPCR is that the bacterial DNA contamination intrinsic to the manufacture of the polymerase inevitably interferes with the detection of pathogen DNA (Sec. 3.1.4.)

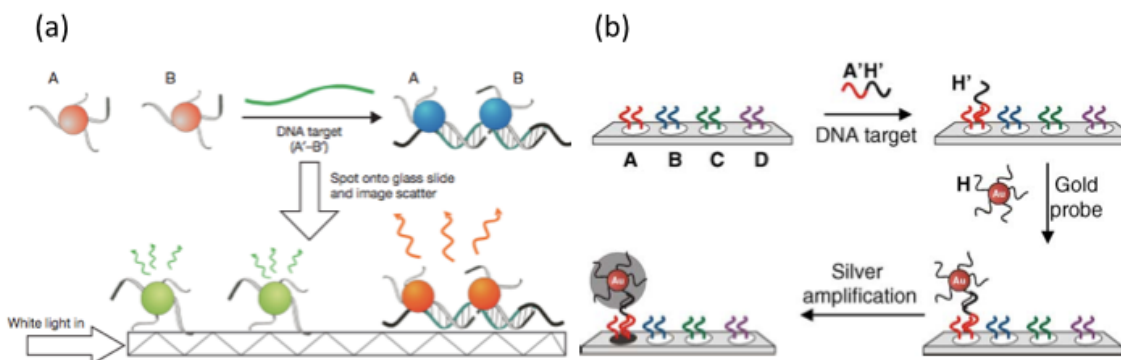


FIGURE 7.1: Variants of Nanosphere's nanoparticle-based sequence detection method [71, 72].

As an example, Fig. 7.1a illustrates a direct detection method that utilizes 13 nm gold nanoparticles (GNP) conjugated with ~ 200 sequence-specific oligonucleotides and consists of two main steps. Initially, two GNP - DNA probes (GNP - A and GNP - B) are hybridized to the DNA target (A' - target - B'), thus forming the GNP - A - A' - target - B' - B - GNP complex. (A' is part of the target that is complementary to A.) Later, the solution is spotted onto a glass slide and illuminated. A positive detection of the target, in the form of the complexed probes, can then be sensed by the red shift in the spectrum of the evanescent-induced scatter [71]. An updated version of this technique, sketched in Fig. 7.1b, eliminated the need for GNP - B by

pre-binding the slide with the B probe. After washing away the unbound compounds, the GNP is stained with silver. As the particle size grows from 13 nm to $0.5 \sim 1 \mu\text{m}$, the scatter intensity is improved by 10^3 x [73].

The technology outlined above has been commercialized as Nanosphere's Verigene line of bloodstream infection tests [67]. Even though Verigene is not strictly amplification-free (since it analyzes the lysate of 350 μl positive blood culture broth), the example nevertheless shows how direct detection might function.

In this work, the maturity of qPCR is leveraged to provide a relatively predictable path of development. In the long term, however, the potentials of having IPF working in conjunction with a (truly) amplification-free sequence detection method must not be overlooked.

7.2 Conclusions

In the last section of this document, the main objectives of this work and their corresponding results will be summarized.

Challenges of Sepsis Diagnosis

Septic shock is a severe form of bloodstream infection. Its diagnosis is challenging in part for two reasons. First, the infection can be caused by more than 50 species of pathogens. Second, the pathogens might exist in the bloodstream in very low concentrations, e.g., less than 1 colony-forming unit/ml blood. Consequently, depending on the method it might be necessary to analyze $3 \sim 20$ ml of blood. In turn, these difficulties of identifying the pathogens translate to inadequate and delayed treatments. The median time to receive an effective antimicrobial therapy is 6 hr after hypotension onset. By then, the survival rate has dropped at an average of 7.6%/hr to 42%.

Identification of Suitable Microfluidic Technologies

To address this issue, this work aims to take advantage of the advances in microfluidic technologies to expedite and automate the detection of sparse pathogens in a large-volume biofluid. In particular, the diagnostic method evaluated to be most amenable to the enhancements is magnetic bead-based nucleic acid purification followed by sequence detection via multiplex qPCR.

Subsequently, the solution is identified to be a fluidic device that integrates immiscible phase filtration (IPF) and digital microfluidic droplet actuation (DM, Fig. 4.3.) IPF utilizes the high interfacial tension at the aqueous/immiscible interface to minimize the carryover of PCR inhibitors when the nucleic acid-bound beads are transported away from the lysate (Fig. 4.4.) Relative to a typical benchtop solid phase extraction procedure, a well-tuned IPF reagent system could attain the necessary degree of purification in appreciably fewer wash steps, thereby considerably reducing the purification time. Also, IPF is far more compatible with low-cost automation.

In addition to purifying the nucleic acids, IPF also scales down the volume to what can be efficiently manipulated by DM. Thus, after elution DM could be used to automatically prepare the PCR reaction mixtures (Fig. 4.1), which further reduces the hands-on time and the chance of contamination. Afterwards, either whole-chip thermocycling or temperature zone PCR can be employed (Fig. 4.2.) The latter in particular might substantially trim the PCR time. Notably, unlike the methods that rely on the magnetic beads to transport the droplets, DM can be scaled up to concurrently execute multiple multiplex qPCR reactions.

IPF - DM Integration: Demonstration and Characterization

As the first step towards such a sample-to-answer sparse pathogen detection device, the key result of this work is showing the feasibility of the IPF - DM integration. As can be seen in Fig. 6.6, the demonstration involves all three steps that are at the

core of the proposed scheme: (1) Purify the DNA from an inhibitor solution with two IPF washes. (2) Prepare the PCR mixture droplet using DM actuation. (3) Perform qPCR to quantify the target.

Further, as summarized in Sec. 6.4, the performance of the current system has been characterized, including the purification power, amplification efficiency, nucleic acid retention, and the level of background contamination. The evaluation involved UV absorbance measurement (Fig. 6.4) and on-chip qPCR (Fig. 6.5, 6.7.) These results would facilitate the revising of the device design and the protocols. For instance, the data suggest that future iterations of the fluidic device should employ the materials with higher temperature ratings that do not emit PCR inhibitors under thermocycling conditions. Also, to improve the nucleic acid retention, bead - buffer mixing needs to be enhanced, especially during elution. A system updated with these improvements would be better suited to validate the qualitative design rules outlined on p. 41.

Improvements on Device Fabrication

The developed fluidic device features two notable improvements. Importantly, both are application-agnostic and applicable to the fabrication of other DM devices.

First, the ability to perform DM droplet actuation at elevated temperatures is obtained with the adoption the ITO/PEDOT:PSS/acrylic top plate (Fig. 5.6.) This is utilized to maintain the droplet - sensor alignment during thermocycling. Interestingly, oxygen plasma ashing of the acrylic immediately prior to the spin coating of PEDOT:PSS is found to be essential to the enhancement of temperature tolerance (Table 5.7.)

Second, the fabrication time is markedly reduced by laser patterning the Clarex cast acrylic top plate and the SecureSeal gasket (Fig. 5.5.) The mask-less manufacturing also permits the designs to be modified on-demand. In contrast, the conventional

thick SU-8 gasket is time-consuming to fabricate, crack-prone, and provides lesser sealing.

Construction of Auxiliary Systems

Temperature control and fluorescence sensing systems are needed to support the execution of qPCR. However, because off-the-shelf solutions are either incompatible or unaffordable, significant effort was spent on constructing the auxiliary systems that are uniquely suited for the operation of the custom fluidic device. Briefly, the temperature control system permits different PID parameters to be run in different phases of a thermocycle (Fig. 5.14.) This fine-grained control over the balance between fast ramping and reduced overshoot is a provision for refining the PCR time and amplification efficiency. Additionally, other than measuring the fluorescence generated by qPCR, it seems feasible to adapt the fiber optic fluorescence sensor to estimate the droplet volume (Fig. 5.23 ~ 5.26.) This method might replace lens - camera-based droplet observation in an application that demands a tight package.

Estimation of Sample-to-Answer Time

Finally, to reiterate the main advantage of the selected approach, an assessment of the sample-to-answer time is provided in Table 7.1. With a fully evolved IPF - DM fluidic device, current evidences indicate that the total run time might be reduced from the present 6 ~ 10 hr to 1.5 hr. More importantly, the hands-on time could be trimmed by 90% to approximately 20 min (mechanical lysis and reagent loading.) These differences may ultimately improve the survival rate of septic shock from 42% to 70%.

Table 7.1: Estimated total run time and hands-on time.

Step	Benchtop	IPF+DM
	Time (hr)	
Mechanical lysis	0.25	0.25
Chemical lysis, purification	1.75 ~ 2.75	0.42 ¹
qPCR preparation	1	0.05
qPCR	1.5	0.3 ~ 0.7 ²
Melting curve	0.5	0.5
Total / hands-on	6 / 3	1.52 / 0.33

¹ Reagent loading followed by on-chip chemical lysis, purification, and elution = 5 + 10 + 5 + 5 min.

² Temperature zone PCR ~ whole-chip thermocycling.

Appendix A

Experimental Methods

A.1 Effect of GuSCN on PCR

In Sec. 6.1.1 the following procedure is used to determine the PCR inhibiting concentration of GuSCN.

The experiment takes advantage of the synthetic internal control (IC) DNA and its corresponding assay that are included in the Qiagen QuantiFast PCR + IC kit. Following the vendor-recommended protocol, each 25 μ l PCR reaction mixture consists of 5 μ l master mix, 2.5 μ l IC assay, 2.5 μ l IC DNA (10^3 initial copies), 0.5 μ l reference dye ROX, 12 μ l nuclease-free water, and 2.5 μ l GuSCN solution. The GuSCN solutions are separately prepared by diluting Wash Buffer 1 in the miniMAG purification kit with nuclease-free water to the desired GuSCN concentration. The final GuSCN concentrations tested are 0.05, 5, 15.8, 25, 50, 158, 250, and 500 mM. In addition, there are two controls: the positive control that does not contain GuSCN, and the No Template Control that does not contain the IC DNA and GuSCN. Nuclease-free water is added to the controls to maintain the 25 μ l reaction volume. For each condition there were three replicates.

After the reaction mixtures are loaded to a 96-well plate, the plate is sealed with an optical adhesive film, centrifuged briefly at 1500 RPM, and inserted into the benchtop qPCR instrument ABI 7900HT. Throughout the preparation, the exposure of the reagents to light is minimized. Further, before pipetting the reagents are always vortexed to ensure homogeneity. Finally, qPCR is initiated with the thermocycling profile: polymerase activation 95 °C 5 min, and then 95 °C 15 s/60 °C 30 s for 45 cycles.

A.2 GuSCN Concentration vs. Number of Washes

In Sec. 6.1.2 the device and the procedure described below are used to generate the eluent for the subsequent absorbance measurement on the NanoDrop spectrophotometer.

Device: The device used in this test is an interim implementation of what is later developed into the purification stage of the fluidic device discussed in Sec. 5.2. As shown in Fig. A.1, it consists of a laser-patterned double-sided adhesive film (120 μm -thick SecureSeal) placed on a glass slide. This structure is then spin-coated with Cytop in order to render the liquid-facing surfaces hydrophobic.

Preparation of bead/WB1 suspension: The preparation of the bead/WB1 suspension involves three major steps. First, 50 μl Magnetic Extraction Reagent (that is, the magnetic beads) is added to 1 ml Lysis Buffer. Next, after incubating and centrifuging the bead/LB suspension, the LB supernatant is aspirated. Lastly, the beads are resuspended with 400 μl WB1 (i.e., 5 M GuSCN.) To ensure the same amount of beads is used in each test, the suspension is thoroughly vortexed before it is pipetted to the device.

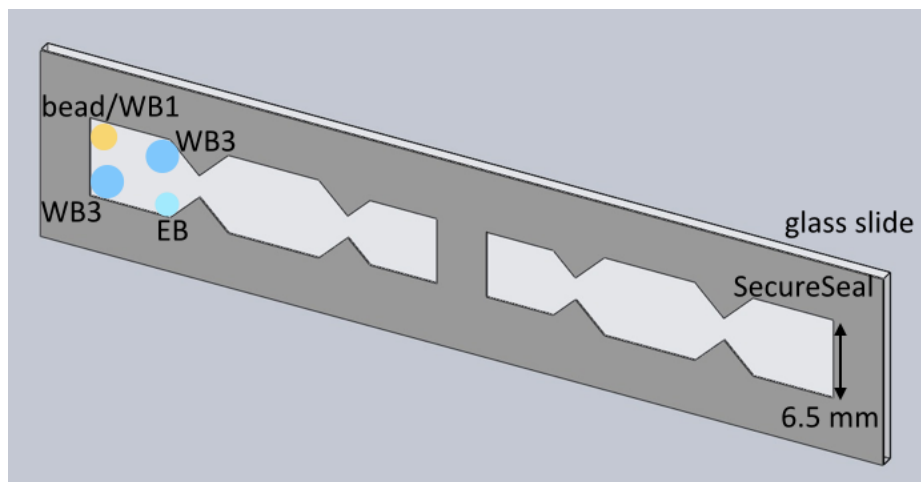


FIGURE A.1: The device employed to measure the purification power. In this variant up to six tests can be performed on a device.

Reagent loading: Prior to an experiment, a device is loaded with three types of reagents: 4 μl magnetic silica beads suspended in WB1, 8 μl WB3, and 2 μl EB. (WB, EB: Wash Buffer and Elution Buffer in the miniMAG purification kit, respectively.) Depending on the number of IPF washes that is being tested, 0 \sim 2 droplets of WB3 are loaded. 2 μl EB is used because it is the typical capacity of the reservoirs in digital microfluidic devices. In turn, since the volume of EB needs to be sufficiently large to accommodate the beads without having the dispensing of eluent droplets impeded, a suitable bead/WB1 volume is empirically determined to be 4 μl .

IPF washes and absorbance measurement: The procedure involves three major steps. First, the magnetic beads in WB1 are actuated by an external magnet either directly to EB (no wash) or to WB3 (1 \sim 2 washes.) During a wash step, the beads are repeatedly dispersed and pelletized in WB3 for five times. Second, the beads along with the GuSCN carryover are brought into contact with EB. Third, with the magnet holding the beads in place, 1.5 μl of the eluent (i.e., EB contaminated with GuSCN) is aspirated from the device and then analyzed on the NanoDrop 1000 spectrophotometer. EB is used to blank the spectrophotometer prior to the measurements.

A.3 Threshold Cycle vs. Number of Washes

The experiment in Sec. 6.2.1 involves two phases. The first phase is identical to the on-chip purification procedure performed in Sec. 6.1.2. The goal is to transport the beads from 5 M GuSCN to the EB without having the GuSCN concentration in the EB rising above 25 mM. To this end, a different number of IPF washes is tested in order to estimate the minimum number needed. Unlike Sec. 6.1.2, however, in the second phase absorbance measurement is replaced by on-chip qPCR as the method for assessing the amount of GuSCN in the eluent. Overall, the experiment can be summarized as:

- Method A: Used in Sec. 6.2.1 to verify the estimation of purification power.
Droplet 1: Master mix, assay, gDNA 1x.
Droplet 2: Beads suspended in GuSCN \rightarrow 0 \sim 2 IPF washes \rightarrow elution \rightarrow dispense eluent as Droplet 2.

Fluidic device: The fluidic device described in Sec. 5.2 is first used in this experiment. In particular, the thermocouple is attached to the bottom of the device before loading the reagents, i.e., the stack from top to down is device/thermal paste/TC/Kapton tape. Furthermore, with the help of the alignment guides, the TC is always placed at the same position relative to the edges of the fluidic device. This is necessary for improving the repeatability of temperature measurements.

Preparation of master mix/Yb8 assay/gDNA solution: The Fast Advanced master mix is used in all on-chip qPCR experiments. Following the vendor-provided protocol, a 20 μ l reaction mixture consists of 10 μ l master mix, 1 μ l Yb8 assay, 7 μ l nuclease-free water, and 2 μ l 0.1 ng/ μ l gDNA. In the No Template Control, gDNA is replaced by

water. A fresh 20 μl stock is prepared for each test case, and the same stock is used in all three replicates of a test case. The resulting PCR mixture droplet would have 5 pg/ μl gDNA, which is equivalent to 285 copies of Yb8 in the 92 nl mixture. In later discussions 285 copies is generally referred as “1x.”

On-chip purification: The purification procedure is identical to what is performed in the experiment in Sec. 6.1.2 (refer to p. 151 for the procedures of bead/WB1 preparation, reagent loading, and IPF washes) with the exception of two differences. First, instead of the purification stage, EB is loaded to its designated reservoir in the PCR preparation stage of the fluidic device. Second, in this case by the end of the purification procedure the contaminated EB is not aspirated off the device. Rather, it remains in the reservoir as the source of the eluent droplets.

After purification, the remaining WB1 and WB3 are removed from the purification stage, and the PCR preparation stage is filled with 5 cS silicone oil. Subsequently, the device is mounted onto a translational stage, and the electrical connection to the DM electrodes is established. An enclosure is employed to shield the reagents on the device and the device-side optical fiber from unwanted light.

On-chip PCR mixture preparation: The PCR mixture preparation process involves three major steps. First, using DM actuation an eluent droplet is dispensed from the EB reservoir. Second, the other reservoir is loaded with the master mix/assay/DNA solution, and a droplet is dispensed from this reservoir. Note that the master mix/assay/DNA solution is only pipetted to the device after the eluent droplet is generated. This is done in order to mitigate DNA contamination and the photo-bleaching of the qPCR probe. Third, the two droplets are merged together, resulting in a PCR mixture droplet that is ready to be thermocycled. This PCR mixture droplet is held in place by DM actuation during thermocycling to prevent it from

drifting away from the sensing area of the optical fiber.

In the above PCR mixture preparation process, droplet actuation is guided by visual observation via a long working distance zoom lens coupled to a CCD camera. Illumination is kept to minimum intensity to reduce photobleaching. Additionally, in the two dispensing steps, a droplet is only accepted if its diameter is comparable to the pitch of the DM electrodes.

On-chip qPCR: Upon completing the preparation of the reaction mixture droplet, the device-side optical fiber of the fluorescence sensor is brought into gentle contact with the top plate and aligned to the droplet. Then, thermocycling is started with the following setpoints: UNG incubation 53 °C 2 min, polymerase activation 98 °C 40 s, 98 °C 1 s/62 °C 20 s for the first 10 cycles, and 95 °C 1 s/62 °C 20 s for the remaining 30 cycles. Note that the temperature experienced by the droplet is different from the setpoints.

The measurement of 559 nm intensity is initiated every time the thermocouple is cooled to the anneal/extend temperature setpoint. At this moment, the laser is turned on and given 300 ms to stabilize its power. Then, the CCD spectrometer integrates for 300 ms, after which the laser is turned off. This process is repeated in each thermocycle.

A.4 Amplification Efficiency

Sec. 6.3.1 focuses on evaluating the on-chip amplification efficiency. The experiment involves two phases: PCR mixture preparation and thermocycling. The first phase is outlined below. It can be seen that two template concentrations are tested (1x, 30x) in order to estimate the amplification efficiency.

- Method B: Used in Sec. 6.3.1 to characterize the on-chip amplification efficiency.

Droplet 1: Master mix, assay, gDNA – 1x (B1), 30x (B2), 0x (B3).

Droplet 2: Elution Buffer.

Preparation of master mix/Yb8 assay/gDNA solution: A fresh 20 μl stock of the master mix/assay/DNA solution is prepared for each test case, and the same stock is used in all three replicates of a test case. All three stocks contain 10 μl Fast Advanced master mix and 1 μl Yb8 assay. In addition, B1 contains 7 μl nuclease-free water and 2 μl 0.1 ng/ μl gDNA; B2 contains 3 μl water and 6 μl 1 ng/ μl gDNA; B3 contains 9 μl water but no gDNA, which serves as the No Template Control. As an example, in B1 the PCR mixture droplet has 5 pg/ μl gDNA, which equates to 1x/285 copies of Yb8 in the 92 nl mixture.

On-chip PCR mixture preparation: The fluidic device described in Sec. 5.2 is used. Initially, the thermocouple is aligned and attached to the device. Next, the device is mounted onto a translational stage, and the electrical connection to the DM electrodes is established. An enclosure is employed to protect the reagents on the device and the device-side optical fiber from unwanted light.

After loading the two reagents and the silicone oil to the device, DM actuation is used to dispense the EB droplet and the master mix/assay/DNA droplet from their respective reservoirs. Subsequently, the two droplets are merged to form the PCR mixture droplet. In the PCR mixture preparation process, droplet actuation is guided by visual observation via a long working distance zoom lens coupled to a CCD camera. Illumination is kept to minimum intensity to reduce photobleaching. Additionally, in the two dispensing steps, a droplet is only accepted if its diameter is comparable to the pitch of the DM electrodes.

On-chip qPCR: Prior to thermocycling, the zoom lens is moved away from the translational stage to prevent it from blocking the access of the device-side optical fiber to the fluidic device. In turn, the fiber is brought into gentle contact with the top plate and aligned to the droplet. At this point, the reaction mixture droplet is held in place by DM actuation to prevent it from drifting away during thermocycling from the sensing area of the optical fiber. Finally, qPCR is performed in the same way as discussed on p. 155.

A.5 Nucleic Acid Retention

Sec. 6.2.2 attempts to estimate the retention of Yb8 throughout the workflow. As outlined below, the experiment involves off-chip binding and on-chip purification, PCR mixture preparation, qPCR.

- Method C: Used in Sec. 6.2.2 to characterize the nucleic acid retention.

Droplet 1: Master mix, assay.

Droplet 2: Beads with gDNA suspended in GuSCN → 2 IPF washes → elution → dispense eluent as Droplet 2 ($30x \times \text{retention}\%$).

Preparation of gDNA-bead/WB1 suspension: The preparation of the gDNA-bead/WB1 suspension involves three major steps. First, 60 μl 1 ng/ μl gDNA ($\sim 1.3 \times 10^5x$ copies of Yb8) and then 50 μl Magnetic Extraction Reagent (that is, the magnetic beads) are added to 1 ml Lysis Buffer. Next, after incubating and centrifuging, the LB supernatant is aspirated. Lastly, the DNA-bound beads are resuspended with 400 μl WB1 (i.e., 5 M GuSCN.) To ensure the amount of Yb8 is consistent across the replicates, the suspension is briefly vortexed before 4 μl ($\sim 1.3 \times 10^3x$ copies) is transferred to the device. Assuming all Yb8 is retained, a reaction mixture droplet would possess 30x copies.

Although the binding capacity of the beads in the miniMAG purification kit is unspecified by the vendor, the maximum values recommended by the surveyed silica particle-based kits all fall in $10^{2\sim 3}$ ng DNA per μl bead slurry (e.g., MO BIO UltraClean 15, Bioclone BcMag Quick DNA, and AMS MagSi-DNA.) Therefore, the employed 1.2 ng/ μl is assumed to be within the capacity.

Preparation of master mix/Yb8 assay solution: A 40 μl stock was prepared from 20 μl Fast Advanced master mix, 2 μl Yb8 assay, and 18 μl nuclease-free water. The water is added to keep the final master mix and assay concentrations identical to what are used in the previous experiments. The same stock is used in all three replicates.

On-chip purification: The fluidic device described in Sec. 5.2 is used. Prior to an experiment, 4 μl DNA-bead/WB1 and 8 μl WB3 (two locations) are loaded to the purification stage, and 2 μl EB is filled to its reservoir in the PCR preparation stage.

Since the gDNA has been previously bound to the magnetic beads, there are two steps remain in the purification process: IPF wash and elution. To perform the first IPF wash, the DNA-bound beads in WB1 are actuated by an external magnet to WB3. Then, the beads are repeatedly dispersed and pelletized in WB3 five times. The first wash is concluded by actuating the beads away from the WB3. Later, the beads are transported to the second WB3 to conduct the second IPF wash. After the two washes, the beads are transferred from the second WB3 in the purification stage to the EB reservoir in the PCR preparation stage. To release the DNA from the beads to EB, the beads are incubated with the EB at room temperature for 5 min.

Afterwards, to ready the device for the subsequent steps, the remaining WB1 and WB3 are removed from the purification stage. Also, the PCR preparation stage is filled with 5 cS silicone oil.

On-chip PCR mixture preparation, qPCR: The procedures for the mixture preparation and qPCR are the same as outlined on p. 154.

Appendix B

Dye-Based Initial Evaluation of Immiscible Phase Filtration

B.1 Experimental Methods

As illustrated in Fig. B.1a, the prototype IPF is assembled by mounting a molded PDMS block on a glass slide. It therefore represents a primitive approximation of the proposed Fig 5.5 structure. In particular, the 50 μl input is a solution of Red 40 dye (Kroger), DI water, and 5 μm silica-coated iron oxide superparamagnetic beads (FF-103, Bioclone.) Here, Red 40 serves as the simulated contaminant. To assess the impact of input viscosity on purification power, glycerol (G2025, Sigma-Aldrich) is added in some experiments to achieve up to 38 cP input viscosity. Moreover, to investigate the effect of bead load on purification power, bead load is varied from 0.4 to 1.6 mg. Otherwise, the typical bead load is 1.6 mg. The beads are manually actuated by a 0.64 T NdFeB magnet (B666-N52, K&J Magnetics.) Depending on the tests, one to three washes are conducted. To facilitate the removal of contaminants that might be entrapped in a bead pellet, during a wash step the beads are vigorously agitated. With three washes, IPF is generally completed in three minutes. After IPF,

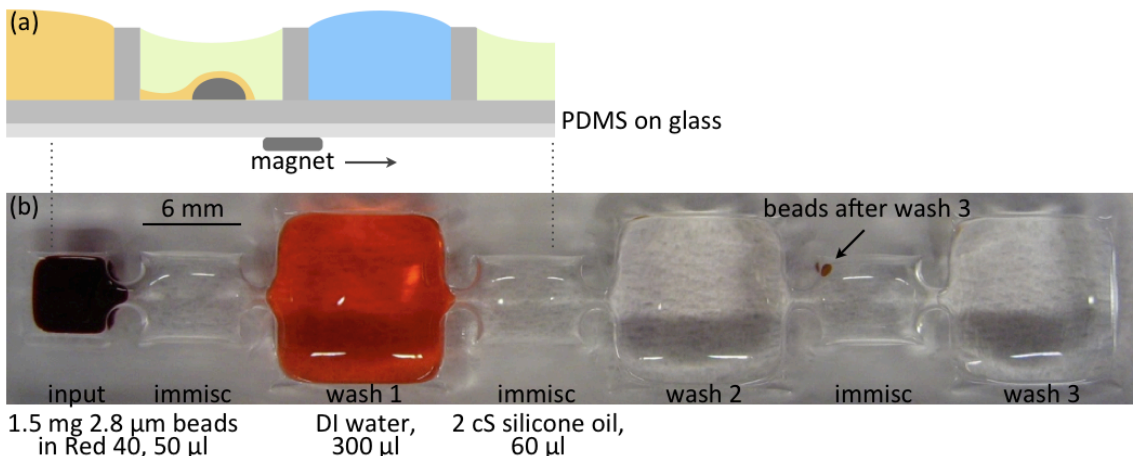


FIGURE B.1: An early PDMS-based IPF. (a) An illustration of the device structure and the bead snapping process. Side view. (b) As evident from the decreasing color intensity in successive wash chambers, the concentration of the simulated contaminant Red Dye 40 carried by the beads decreases as the beads are transported from input to wash 3. Top-down view.

input and wash solutions are monitored by a spectrophotometer (Genesis 20, Thermo Electron) for the absorbance at 502 nm. Lastly, purification power is calculated by normalizing the absorbance of wash solutions to the absorbance of the input. It is recognized that the complexities of nucleic acid purification and amplification are not fully modeled by the described setup. For instance, Red 40 and DNA fragments are different in electrostatic and hydrodynamic properties. Nevertheless, the proof-of-concept setup is perhaps sufficient for understanding the basics of IPF.

B.2 Selection of the Immiscible Phase

To simplify device operation, ideally the same chemical should be used as the immiscible phase in IPF and DM. For this reason, immiscible phases frequently employed in DM are evaluated as the immiscible phase in IPF, e.g. air [74] and low viscosity oils such as dodecane [75] and 2 cS silicone oil [31]. In the case of air, beads can only be snapped out of the input solution after surfactants such as Triton X-100 (TX1568, EMD Millipore) are added to the input. That is, the unmodified input/air interfacial

tension, 72 mN/m, is too high for bead snapping on a PDMS surface. On the other hand, in the case of 2 cS silicone oil (Gelest) the 40 mN/m input/oil interfacial tension seems to be adequate for bead snapping. Additionally, bead transportation in the immiscible phase appears to be smoother in silicone oil than in air. Based on the observation by Dulk *et al.* [39], this may be attributed to the reduced bead-PDMS friction in oil. However, over the course of tens of minutes the soak in silicone oil is observed to cause severe PDMS swelling. With the device geometry and surface properties altered, bead snapping on reused devices is found to generate excessive contamination carryover. In the case of dodecane (Alfa Aesar), the swelling is somewhat more pronounced. Therefore, all subsequent experiments in Appendix B were conducted on fresh devices with 2 cS silicone oil as the immiscible phase.

B.3 Effect of Input Viscosity and Interfacial Tension

In the project it is expected to encounter a wide range of input viscosities: from fragmented DNA or lysed cells suspended in a buffer, to the viscous suspension aspirated from lysed blood. Thus, the impact of input viscosity on purification power is investigated. Still, adding glycerol to increase the input viscosity has a side effect of lowering the input/oil interfacial tension. In turn, the bead pellet snapped out of the input is usually accompanied by an unsatisfactory carryover volume. In the worst case, this could result in the formation of a liquid bridge between the input and the wash solution. To overcome the issue, it is discovered that a device could be slightly tilted (counterclockwise in Fig. B.1a) to promote the pullback of the input solution during bead snapping. The finding implies that when the input/oil interfacial tension is slightly below the optimum range, an IPF device with a characteristic length comparable to the capillary length of the input

solution might utilize the tilt to improve the purification power without involving extra surfactants. Using the tilt technique, in $1 \sim 38$ cP the purification power appears to be unaffected by the increase in input viscosity. (As a comparison, the viscosity of whole blood at 37°C and 0.7 s^{-1} shear rate is 33 cP [76].) However, at higher input viscosity the actuation of beads during bead snapping needs to be slowed down, e.g. 1 mm/s. Afterwards, faster bead transportation could be resumed once most of the viscous contaminants are removed by the first wash.

B.4 Effect of Bead Load on Purification Power

The obtained purification power is typically on the order of 10^2 to 10^3 per wash, which is similar to [39]. In other words, after two washes the amount of Red 40 carried by the bead pellet can be reduced by six orders of magnitude. In addition, purification power is determined to be linearly impacted by an increasing bead load. As an example, increasing the bead load from 0.4 mg to 1.6 mg lowers the purification power from 167 to 24. Since the finding suggests a linear correlation between pellet volume and carryover volume (as reported in [35]), it is therefore important to minimize the bead load for instance by improving the capture of nucleic acids during the binding step.

Bibliography

- [1] P. Tissari, A. Zumla, E. Tarkka, S. Mero, L. Savolainen, M. Vaara, A. Aittakorpi, S. Laakso, M. Lindfors, H. Piiparinen, M. Maki, C. Carder, J. Huggett, and V. Gant, “Accurate and rapid identification of bacterial species from positive blood cultures with a DNA-based microarray platform: an observational study,” *The Lancet*, vol. 375, no. 9710, pp. 224–230, 2010.
- [2] M. L. Towns, W. R. Jarvis, and P.-R. Hsueh, “Guidelines on blood cultures,” *Journal of Microbiology, Immunology and Infection*, vol. 43, no. 4, pp. 347–349, 2010.
- [3] L. E. Lehmann, K.-P. Hunfeld, T. Emrich, G. Haberhausen, H. Wissing, A. Hoefl, and F. Stuber, “A multiplex real-time PCR assay for rapid detection and differentiation of 25 bacterial and fungal pathogens from whole blood samples,” *Medical Microbiology and Immunology*, vol. 197, no. 3, pp. 313–324, 2008.
- [4] A. Kumar, D. Roberts, K. E. Wood, B. Light, J. E. Parrillo, S. Sharma, R. Suppes, D. Feinstein, S. Zanotti, L. Taiberg, D. Gurka, A. Kumar, and M. Cheang, “Duration of hypotension before initiation of effective antimicrobial therapy is the critical determinant of survival in human septic shock,” *Critical Care Medicine*, vol. 34, no. 6, pp. 1589–96, 2006.
- [5] L. Dubska, M. Vyskocilova, D. Minarikova, P. Jelinek, R. Tejkalova, and D. Valik, “LightCycler SeptiFast technology in patients with solid malignancies: clinical utility for rapid etiologic diagnosis of sepsis,” *Critical Care*, vol. 16, no. 1, p. 404, 2012.
- [6] N. Mancini, D. Clerici, R. Diotti, M. Perotti, N. Ghidoli, D. De Marco, B. Pizzorno, T. Emrich, R. Burioni, F. Ciceri, and M. Clementi, “Molecular diagnosis of sepsis in neutropenic patients with haematological malignancies,” *Journal of Medical Microbiology*, vol. 57, no. 5, pp. 601–604, 2008.
- [7] D. C. Angus and T. van der Poll, “Severe sepsis and septic shock,” *New England Journal of Medicine*, vol. 369, no. 9, pp. 840–851, 2013.

- [8] F. R. Coelho and J. O. Martins, “Diagnostic methods in sepsis: the need of speed,” *Rev Assoc Med Bras*, vol. 58, no. 4, pp. 498–504, 2012.
- [9] K.-E. Kim and J.-Y. Han, “Evaluation of the clinical performance of an automated procalcitonin assay for the quantitative detection of bloodstream infection,” *Korean Journal of Laboratory Medicine*, vol. 30, no. 2, pp. 153–159, 2010.
- [10] S. Laakso, J. Kirveskari, P. Tissari, and M. Mäki, “Evaluation of high-throughput PCR and microarray-based assay in conjunction with automated DNA extraction instruments for diagnosis of sepsis,” *PLoS ONE*, vol. 6, no. 11, p. e26655, 2011.
- [11] J. Gong and C.-J. C. J. Kim, “All-electronic droplet generation on-chip with real-time feedback control for ewod digital microfluidics,” *Lab Chip*, vol. 8, no. 6, pp. 898–906, 2008.
- [12] B. Hadwen, G. R. Broder, D. Morganti, A. Jacobs, C. Brown, J. R. Hector, Y. Kubota, and H. Morgan, “Programmable large area digital microfluidic array with integrated droplet sensing for bioassays,” *Lab Chip*, vol. 12, no. 18, pp. 3305–13, 2012.
- [13] K. Hu, B.-N. Hsu, A. Madison, K. Chakrabarty, and R. B. Fair, “Fault detection, real-time error recovery, and experimental demonstration for digital microfluidic biochips,” in *Design, Automation Test in Europe Conference Exhibition (DATE), 2013*, 2013, pp. 559–564.
- [14] F. C. Lawyer, S. Stoffel, R. K. Saiki, S. Y. Chang, P. A. Landre, R. D. Abramson, and D. H. Gelfand, “High-level expression, purification, and enzymatic characterization of full-length *Thermus aquaticus* DNA polymerase and a truncated form deficient in 5’ to 3’ exonuclease activity.” *Genome Research*, vol. 2, no. 4, pp. 275–287, 1993.
- [15] M. J. McPherson and S. G. Moller, *PCR: The Basics*, 2nd ed. Taylor & Francis, 2006.
- [16] E. A. Pestana, *Early, rapid and sensitive veterinary molecular diagnostics - real time PCR applications*. Springer, 2010.
- [17] *Critical Factors for Successful Real-Time PCR*, Qiagen, 2010.
- [18] M. A. Innis, K. B. Myambo, D. H. Gelfand, and M. A. Brow, “DNA sequencing with *Thermus aquaticus* DNA polymerase and direct sequencing of polymerase

- chain reaction-amplified DNA,” *Proceedings of the National Academy of Sciences*, vol. 85, no. 24, pp. 9436–9440, 1988.
- [19] *TaqMan Fast Advanced Master Mix Protocol (Rev. C)*, Applied Biosystems, 2011.
- [20] I. R. Perch-Nielsen, D. D. Bang, C. R. Poulsen, J. El-Ali, and A. Wolff, “Removal of PCR inhibitors using dielectrophoresis as a selective filter in a microsystem,” *Lab Chip*, vol. 3, pp. 212–216, 2003.
- [21] E. Pelt-Verkuil, A. Belkum, and J. P. Hays, *Principles and technical aspects of PCR amplification*. Springer, 2008.
- [22] *AmpliTaq Gold DNA Polymerase, LD (Rev. D)*, Applied Biosystems, 2010.
- [23] E. Chern, S. Sieftring, J. Paar, M. Doolittle, and R. Haugland, “Comparison of quantitative PCR assays for *Escherichia coli* targeting ribosomal RNA and single copy genes,” *Letters in Applied Microbiology*, vol. 52, no. 3, pp. 298–306, 2011.
- [24] S. Philipp, H. P. Huemer, E. U. Irschick, and C. Gassner, “Obstacles of multiplex real-time PCR for bacterial 16S rDNA: Primer specificity and DNA decontamination of Taq polymerase,” *Transfusion Medicine and Hemotherapy*, vol. 37, no. 1, pp. 21–28, 2010.
- [25] K. Choi, A. H. Ng, R. Fobel, and A. R. Wheeler, “Digital microfluidics,” *Annual Review of Analytical Chemistry*, vol. 5, no. 1, pp. 413–440, 2012.
- [26] W. C. Nelson and C.-J. Kim, “Droplet actuation by electrowetting-on-dielectric (EWOD): a review,” *Journal of Adhesion Science and Technology*, vol. 26, no. 12-17, pp. 1747–1771, 2012.
- [27] F. Mugele, “Fundamental challenges in electrowetting: from equilibrium shapes to contact angle saturation and drop dynamics,” *Soft Matter*, vol. 5, no. 18, pp. 3377–3384, 2009.
- [28] F. Mugele and J. Buehrle, “Equilibrium drop surface profiles in electric fields,” *Journal of Physics: Condensed Matter*, vol. 19, no. 37, p. 375112, 2007.
- [29] M. J. Jebrail, H. Yang, J. M. Mudrik, N. M. Lafreniere, C. McRoberts, O. Y. Al-Dirbashi, L. Fisher, P. Chakraborty, and A. R. Wheeler, “A digital microfluidic method for dried blood spot analysis,” *Lab Chip*, vol. 11, pp. 3218–3224, 2011.

- [30] G. J. Shah, H. Ding, S. Sadeghi, S. Chen, C.-J. C. J. Kim, and R. M. van Dam, "On-demand droplet loading for automated organic chemistry on digital microfluidics," *Lab Chip*, vol. 13, no. 14, pp. 2785–95, 2013.
- [31] R. Fair, "Digital microfluidics: is a true lab-on-a-chip possible?" *Microfluidics and Nanofluidics*, vol. 3, no. 3, pp. 245–281, 2007.
- [32] R. S. Sista, A. E. Eckhardt, V. Srinivasan, M. G. Pollack, S. Palanki, and V. K. Pamula, "Heterogeneous immunoassays using magnetic beads on a digital microfluidic platform," *Lab Chip*, vol. 8, pp. 2188–2196, 2008.
- [33] S. Srigunapalan, I. A. Eydelnant, C. A. Simmons, and A. R. Wheeler, "A digital microfluidic platform for primary cell culture and analysis," *Lab Chip*, vol. 12, pp. 369–375, 2012.
- [34] H. Ren, R. B. Fair, M. G. Pollack, and E. J. Shaughnessy, "Dynamics of electro-wetting droplet transport," *Sensors and Actuators B: Chemical*, vol. 87, no. 1, pp. 201–206, 2002.
- [35] K. Sur, S. M. McFall, E. T. Yeh, S. R. Jangam, M. A. Hayden, S. D. Stroupe, and D. M. Kelso, "Immiscible phase nucleic acid purification eliminates PCR inhibitors with a single pass of paramagnetic particles through a hydrophobic liquid," *Journal of Molecular Diagnostics*, vol. 12, no. 5, pp. 620–628, 2010.
- [36] S. M. Berry, E. T. Alarid, and D. J. Beebe, "One-step purification of nucleic acid for gene expression analysis via immiscible filtration assisted by surface tension (IFAST)," *Lab on a Chip*, vol. 11, no. 10, pp. 1747–1753, 2011.
- [37] J. Pipper, Y. Zhang, P. Neuzil, and T.-M. Hsieh, "Clockwork PCR including sample preparation," *Angewandte Chemie-International Edition*, vol. 47, no. 21, pp. 3900–3904, 2008.
- [38] U. Lehmann, C. Vandevyver, V. Parashar, and M. Gijs, "Droplet-based DNA purification in a magnetic lab-on-a-chip," *Angewandte Chemie-International Edition*, vol. 45, no. 19, pp. 3062–3067, 2006.
- [39] R. C. den Dulk, K. A. Schmidt, R. Gill, J. C. Jongen, and M. W. Prins, "Magneto-capillary valve for lab-on-a-chip sample preparation," in *14th International Conference on Miniaturized Systems for Chemistry and Life Sciences*, 2010, pp. 449–451.
- [40] T. Ohashi, H. Kuyama, K. Suzuki, and S. Nakamura, "Control of aqueous droplets using magnetic and electrostatic forces," *Analytica Chimica Acta*, vol. 612, no. 2, pp. 218–225, 2008.

- [41] Z. Long, A. M. Shetty, M. J. Solomon, and R. G. Larson, “Fundamentals of magnet-actuated droplet manipulation on an open hydrophobic surface,” *Lab Chip*, vol. 9, no. 11, pp. 1567–75, 2009.
- [42] A. Bange, “Development and characterization of miniaturized electrochemical immunosensors,” Ph.D. dissertation, University of Cincinnati, 2006.
- [43] S. D. Carrigan, G. Scott, and M. Tabrizian, “Toward resolving the challenges of sepsis diagnosis,” *Clinical Chemistry*, vol. 50, no. 8, pp. 1301–1314, 2004.
- [44] Z. Hua, J. L. Rouse, A. E. Eckhardt, V. Srinivasan, V. K. Pamula, W. A. Schell, J. L. Benton, T. G. Mitchell, and M. G. Pollack, “Multiplexed real-time polymerase chain reaction on a digital microfluidic platform,” *Analytical Chemistry*, vol. 82, no. 6, pp. 2310–2316, 2010.
- [45] S. H. Holm, J. P. Beech, M. P. Barrett, and J. O. Tegenfeldt, “Separation of parasites from human blood using deterministic lateral displacement,” *Lab on a Chip*, vol. 11, no. 7, pp. 1326–1332, 2011.
- [46] Y. Zhang, S. Park, K. Liu, J. Tsuan, S. Yang, and T.-H. Wang, “A surface topography assisted droplet manipulation platform for biomarker detection and pathogen identification,” *Lab Chip*, vol. 11, no. 3, pp. 398–406, 2011.
- [47] R. C. den Dulk, K. A. Schmidt, G. Sabatté, S. Liébana, and M. W. J. Prins, “Magneto-capillary valve for integrated purification and enrichment of nucleic acids and proteins,” *Lab Chip*, vol. 13, no. 1, pp. 106–18, 2013.
- [48] J. Pawliszyn and H. Lord, *Handbook of Sample Preparation*. John Wiley & Sons, 2010.
- [49] M. Zordan, R. Fatig, L. Reece, V. J. Davisson, and J. Leary, “An efficient method to produce clonal colonies of cancer cells using laser enabled analysis and processing (leap),” in *Proc. SPIE*, D. L. Farkas, D. V. Nicolau, and R. C. Leif, Eds., vol. 6859, no. 1. SPIE, 2008, p. 685910.
- [50] C. Chiang, *Statistical Methods of Analysis*. World Scientific, 2003.
- [51] S. Champlot, C. Berthelot, M. Pruvost, E. A. Bennett, T. Grange, and E.-M. Geigl, “An efficient multistrategy DNA decontamination procedure of PCR reagents for hypersensitive PCR applications,” *PLoS ONE*, vol. 5, no. 9, p. e13042, 2010.

- [52] J. A. Walker, G. E. Kilroy, J. Xing, J. Shewale, S. K. Sinha, and M. A. Batzer, "Human DNA quantitation using Alu element-based polymerase chain reaction," *Analytical Biochemistry*, vol. 315, no. 1, pp. 122–128, 2003.
- [53] E. H. van der Horst, J. H. Leupold, R. Schubbert, A. Ullrich, and H. Allgayer, "TaqMan-based quantification of invasive cells in the chick embryo metastasis assay," *Biotechniques*, vol. 37, no. 6, pp. 940–946, 2004.
- [54] F. J. Miller, F. L. Rosenfeldt, C. Zhang, A. W. Linnane, and P. Nagley, "Precise determination of mitochondrial DNA copy number in human skeletal and cardiac muscle by a PCR-based assay: lack of change of copy number with age," *Nucleic Acids Research*, vol. 31, no. 11, p. e61, 2003.
- [55] S. Lynch, S. Weinstein, J. Virtamo, Q. Lan, C.-S. Lui, W.-l. Cheng, N. Rothman, D. Albanes, and R. Stolzenberg-Solomon, "Mitochondrial DNA copy number and pancreatic cancer in the alpha-tocopherol beta-carotene cancer prevention (ATBC) study," *Cancer Prevention Research*, 2011.
- [56] E. Callaway, "Deal done over HeLa cell line," *Nature*, vol. 500, pp. 132–133, 2013.
- [57] *QuantiFast Pathogen PCR + IC Handbook*, Qiagen, 2010.
- [58] D. R. McClernon, E. Ramsey, and M. StClair, "Magnetic silica extraction for low-viremia human immunodeficiency virus type 1 genotyping," *Journal of Clinical Microbiology*, vol. 45, no. 2, pp. 572–574, 2007.
- [59] P. Deschaght, T. De Baere, L. Van Simaey, S. Van daele, F. De Baets, D. De Vos, J.-P. Pirnay, and M. Vaneechoutte, "Comparison of the sensitivity of culture, pcr and quantitative real-time pcr for the detection of pseudomonas aeruginosa in sputum of cystic fibrosis patients," *BMC Microbiology*, vol. 9, no. 1, p. 244, 2009.
- [60] H. Wiesinger-Mayr, E. Jordana-Lluch, E. Martro, S. Schoenthaler, and C. Noehammer, "Establishment of a semi-automated pathogen DNA isolation from whole blood and comparison with commercially available kits," *Journal of Microbiological Methods*, vol. 85, no. 3, pp. 206–213, 2011.
- [61] E. R. F. Welch, Y.-Y. Lin, A. Madison, and R. B. Fair, "Picoliter DNA sequencing chemistry on an electrowetting-based digital microfluidic platform," *Biotechnology Journal*, vol. 6, no. 2, pp. 165–176, 2011.

- [62] E. Vitoratos, S. Sakkopoulos, N. Paliatsas, K. Emmanouil, and S. A. Choulis, “Conductivity degradation study of PEDOT: PSS films under heat treatment in helium and atmospheric air,” *Open Journal of Organic Polymer Materials*, vol. 2, no. 1, pp. 7–11, 2012.
- [63] P. Y. Paik, “Adaptive cooling of integrated circuits using digital microfluidics,” Ph.D. dissertation, Duke University, 2006.
- [64] J. Bessetti, *An Introduction to PCR Inhibitors*, 2007.
- [65] P. C. Thomas, L. N. Strotman, A. B. Theberge, E. Berthier, R. O’Connell, J. M. Loeb, S. M. Berry, and D. J. Beebe, “Nucleic acid sample preparation using spontaneous biphasic plug flow,” *Analytical Chemistry*, vol. 85, no. 18, pp. 8641–8646, 2013.
- [66] *NucleoSpin Gel and PCR Clean-up (Rev. 2)*, Macherey-Nagel, 2012.
- [67] B. W. Buchan, C. C. Ginocchio, R. Manii, R. Cavagnolo, P. Pancholi, L. Swyers, R. B. Thomson, Jr, C. Anderson, K. Kaul, and N. A. Ledebor, “Multiplex identification of Gram-positive bacteria and resistance determinants directly from positive blood culture broths: Evaluation of an automated microarray-based nucleic acid test,” *PLoS Medicine*, vol. 10, no. 7, p. e1001478, 2013.
- [68] C. Nunes Kirchner, M. Träuble, and G. Wittstock, “Diffusion and reaction in microbead agglomerates,” *Analytical Chemistry*, vol. 82, no. 7, pp. 2626–2635, 2010.
- [69] H. Rostaing, H. Chetouani, M. Gheorghe, and P. Galvin, “A micromagnetic actuator for biomolecule manipulation,” *Sensors and Actuators A-Physical*, vol. 135, no. 2, pp. 776–781, 2007.
- [70] T. Mann and U. Krull, “The application of ultrasound as a rapid method to provide DNA fragments suitable for detection by DNA biosensors,” *Biosensors & Bioelectronics*, vol. 20, no. 5, pp. 945–955, 2004.
- [71] J. J. Storhoff, A. D. Lucas, V. Garimella, Y. P. Bao, and U. R. Muller, “Homogeneous detection of unamplified genomic DNA sequences based on colorimetric scatter of gold nanoparticle probes,” *Nature Biotechnology*, vol. 22, no. 7, pp. 883–887, 2004.
- [72] J. J. Storhoff, S. S. Marla, P. Bao, S. Hagenow, H. Mehta, A. Lucas, V. Garimella, T. Patno, W. Buckingham, W. Cork, and U. R. Müller, “Gold nanoparticle-based detection of genomic DNA targets on microarrays using a

- novel optical detection system,” *Biosensors and Bioelectronics*, vol. 19, no. 8, pp. 875 – 883, 2004.
- [73] W. H. Buckingham, M. Domanus, S. Hetzel, G. Kunkel, J. Storhoff, and W. Cork, “Direct detection of bacterial genomic DNA using gold nanoparticle probes,” in *Engineering in Medicine and Biology Society, 2004. IEMBS '04. 26th Annual International Conference of the IEEE*, vol. 1, 2004, pp. 1953–1955.
- [74] G. J. Shah, J. L. Veale, Y. Korin, E. F. Reed, H. A. Gritsch, and C.-J. C. Kim, “Specific binding and magnetic concentration of CD8+ T-lymphocytes on electrowetting-on-dielectric platform,” *Biomicrofluidics*, vol. 4, no. 4, p. 044106, 2010.
- [75] K. Zhou, J. Heikenfeld, K. A. Dean, E. M. Howard, and M. R. Johnson, “A full description of a simple and scalable fabrication process for electrowetting displays,” *Journal of Micromechanics and Microengineering*, vol. 19, no. 6, p. 065029, 2009.
- [76] U. Windberger, A. Bartholovitsch, R. Plasenzotti, K. Korak, and G. Heinze, “Whole blood viscosity, plasma viscosity and erythrocyte aggregation in nine mammalian species: reference values and comparison of data,” *Experimental Physiology*, vol. 88, no. 3, pp. 431–440, 2003.

Biography

Full name: Bang-Ning Hsu

Place of birth: Tainan, Taiwan

Date of birth: July 25, 1982

Schools attended:

- National Chiao Tung University, Hsinchu, Taiwan, BS, June 2004
- Duke University, Durham, North Carolina, MS, May 2010
- Duke University, Durham, North Carolina, PhD, May 2014

Publications:

- K. Hu, B.-N. Hsu, A. C. Madison, K. Chakrabarty and R. B. Fair “Fault Detection, Real-Time Error Recovery, and Experimental Demonstration for Digital Microfluidic Biochips,” *Proceedings of the Design, Automation & Test in Europe Conference & Exhibition (DATE '13), Grenoble, France, March 18-22, 2013*, pp. 559–564.
- B.-N. Hsu, A. C. Madison and R. B. Fair “Accelerate Sepsis Diagnosis by Seamless Integration of DNA Purification and qPCR,” *Proceedings of the 16th International Conference on Miniaturized Systems for Chemistry and Life Sciences (microTAS '12), Okinawa, Japan, October 28-November 1, 2012*, pp. 830–832.
- A. Khlystov, B.-N. Hsu, and R. B. Fair “Development of Digital Microfluidic Impactor,” *Proceedings of the 30th Annual American Association for Aerosol Research Conference, Orlando, FL, October 3-7, 2011*.
- J. H. Song, R. Evans, Y.-Y. Lin, B.-N. Hsu, R. B. Fair “A Scaling Model for Electrowetting-on-Dielectric Microfluidic Actuators,” *Microfluidics and Nanofluidics*, vol. 7, pp. 75–89, 2009.